Applications of maximally localized Wannier functions: spin-flip excitations, plasmon dispersion and tight binding models for optical lattices

A thesis submitted to the University of the Basque
Country to obtain the degree of Doctor in Physics by

Julen Ibañez Azpiroz

Supervised by Dr. Aitor Bergara Jauregi
and Dr. Asier Eiguren Goienetxea

July 7, 2013

'ikimilikiliklik'
Mikel Laboa

Contents

Introduction

The electronic structure of a solid can be generally approached from two different viewpoints. In one of them, the atomic approach, electrons are viewed as tightly bound to their parent atoms, interacting very weakly with the rest of the solid. In such an approach, a natural basis for describing the electron states is represented by the atomic orbitals, which are highly localized around a given atom, with little extension to neighboring lattice sites. In a diametrically opposite point of view, electrons can be considered as largely delocalized throughout the solid, with no significant bounds to their parents atoms. An extreme example describing this picture is represented by a plane wave, $e^{i\mathbf{kr}}$. This function, which is a solution of the Schrödinger equation for a free particle, describes a completely delocalized electron state, being the associated probability amplitude independent of the position.

The difference between these two approaches becomes even more clear by considering a characteristic property of crystals, namely the periodicity. Ideal solids are built by the periodic repetition of its unit cell in real space. It follows from this periodicity alone that electron states acquire a factor $e^{i\mathbf{kR}}$ when translated by a direct lattice vector $\mathbf{R}$. Clearly, the above mentioned atomic orbitals do not fulfill such property due to their localization. Therefore, these states are not eigenstates of the system and, consequently, do not possess a definite energy. A plane wave, on the other hand, does satisfy the above periodic property, and it is therefore a valid option for being an eigenstate of the system. Thus, although this type of state is completely delocalized in real space, it can possess a definite energy. Then, the choice between atomic and delocalized viewpoints can be alternatively stated as the choice between localization in real space or localization in energy.

In this thesis, we pay special attention to the first choice, namely the localization in real space. For this, we make use of the concept of localized Wannier functions introduced by Gregory Wannier in 1937 [1]. The essence of this approach is to build functions that are highly localized in real space starting from the eigenstates of a periodic system, generally known as Bloch orbitals. The connection between these two set of functions, Wannier and Bloch, is realized by unitary transformations that carry a large inherent arbitrariness, i.e. Wannier functions are strongly non-unique. This problem was considerably overcome in 1997, when Marzari and Vanderbilt [2] developed a well defined method for determining the set of Wannier functions with minimum spread in real space. The outcome of this approach are the so-called maximally localized Wannier functions (MLWFs), which are the central tool of this thesis.

MLWFs find applications in many areas of condensed matter physics. For instance, these functions represent a natural basis set for tight binding models of periodic systems, where the localization in real space is needed in order to justify the tight binding approach. These models allow to efficiently interpolate several quantities in reciprocal space through the so-called "Wannier interpolation" scheme. This method is widely used in the solid-state community as it allows to consider a very fine sampling of the Brillouin zone at inexpensive computational cost. In metallic systems, for instance, this feature is extremely helpful as integrals bounded by the Fermi surface usually need of a considerable number of **k**-points in order to be converged. In different contexts, MLWFs also demonstrate a great potential. As an example, MLWFs play an important role in many modern theories, such as the current description of the electric polarization [3–5] and the orbital magnetization [6–10] of solids. Electron-phonon interactions [11–13] or molecular dynamics [14, 15] are further examples in which MLWFs are also currently applied.

In this thesis, we make use of MLWFs as a tool for calculating several properties of diverse systems. In Chapter 2, we study the electronic properties of surfaces with strong spin-orbit interaction. In particular, we analyze the low-energy excitations induced by a time-dependent electric field. The associated transition matrix elements involve the position operator, which is a troublesome quantity when dealing with periodic systems. Indeed, due to the delocalization of the Bloch states, this operator is ill-defined in the Bloch representation. To overcome this problem, we express the matrix elements in the Wannier representation, allowing not only to compute the quantity of interest, but also to efficiently interpolate the matrix elements into a fine **k** mesh. The excitation rate calculated considering this method shows that the spin-orbit interaction can have profound effects on the absorption properties of surfaces.

In Chapter 3, we focus on analyzing the collective charge excitations, plasmons, in an *a priori* simple metal, sodium, and their evolution with the applied pressure. For this, we calculate the linear response of the system using the time-dependent generalization of the density functional theory. This is a powerful approach that is able to accurately describe the rearrangement of the electron gas under the influence of an external perturbation. However, the accuracy of this method is accompanied by a heavy computational load, as the formalism involves the contribution of several bands above the Fermi level. Additionally, the Fermi surface of sodium requires a fine sampling of the reciprocal space in order to accurately reproduce the excited properties of the system. Therefore, 'brute-force' calculations become very time demanding, and some scheme for reducing the computational cost is almost mandatory. In this context, we adopt the MLWFs formalism for expressing the electron response function, which is the central quantity in linear response theory. Due to the properties of the MLWFs, the basis acquires a trivial dependence on the momentum of the external perturbation, $\mathbf{q}$, and the evolution of the response function can be efficiently computed. Following Chapter 2, the use of MLWFs allows to interpolate several $\mathbf{k}$-dependent quantities, such as the eigenvalues and eigenfunctions that build up the response function, into a fine $\mathbf{k}$ mesh at inexpensive computational cost. The fine sampling of the reciprocal space allows us to find an anisotropic interband plasmon in an *a priori* simple fcc phase, reflecting an unexpected departure of sodium from the free-electron-like behavior. Additionally, we also find low-energy interband plasmons in the high pressure phases oP8 and tI19 of Na which induce a drastic drop in the reflectivity, in accordance with recent high pressure neutron scattering experiments [16].

Finally, in Chapter 4, we apply the MLWFs for describing the properties of cold atoms trapped in two dimensional optical lattices. This is a field in which MLWFs still have not fully exploited their potential, as they were originally developed in the context of electronic structure of materials. In this final chapter, we study tight binding models of several two dimensional optical lattices in terms of the MLWFs. Again, due to their localized character and the ability of incorporating the contribution of several bands, MLWFs provide an ideal basis set for the tight binding models. In our analysis, we find that the properties of the optical lattice are very well reproduced in terms of a few tight binding coefficients calculated via MLWFs. In particular, our model is able to accurately reproduce the band structure details such as the so-called Dirac points. Therefore, this method is very well suited to theoretically calculate the relevant experimental parameters used in actual measurements, establishing a direct link between theory and experiment.

Chapter 1

The theoretical model

In this first chapter, we introduce the basic theoretical background that will be used throughout the work. It is divided in two main parts. In Sec. (1.1), we analyze basic properties of the electronic structure in solids. We introduce basic concepts such as the notion of the crystal momentum or Bloch orbitals. We also review current methods based on the density functional theory for solving the Schrödinger equation associated to the electrons in solids. In Sec. (1.2), we introduce the concept of Wannier functions as an alternative approach for describing the electronic structure of solids. We pay special attention to a particular class of Wannier functions, the so-called maximally localized Wannier functions introduced by Marzari and Vanderbilt [2]. We introduce the basic definition and properties of these functions, and point out their main advantages and applications in current fields of interest.

1.1 Basic electronic properties of solids

Solids are composed of ions and electrons. The ionic mass M_I is typically of the order of 10^3 times the mass of the electron, m_e, and, as a consequence, the ionic motion is much slower than the electronic one. The classical theory of the harmonic crystal, for instance, predicts ionic velocities of the order of 10^5cm/s, while typical electronic velocities are of the order of 10^8cm/s [17]. This difference between the ionic and the electronic velocities suggests that, as a first approximation, ionic positions can be considered as fixed. Within such approximation, the solid is formed by a static array of ions stacked to their lattice sites while the electrons move throughout the system. The

Hamiltonian corresponding to this situation is given by[1]

$$H = -\frac{1}{2}\sum_{i}^{N}\mathbf{p}_i^2 - \sum_{i}^{N} V_{\text{ext}}(\mathbf{r}_i) + \frac{1}{2}\sum_{i\neq j}^{N}\frac{1}{|\mathbf{r}_i - \mathbf{r}_j|} + E_{II}, \tag{1.1}$$

with $\mathbf{r}_i$ the position variable of the ith electron. The first term in Eq. (1.1) is the electron kinetic energy with $\mathbf{p}_i = -i\boldsymbol{\nabla}_i$ the electron momentum operator. The second term in Eq. (1.1) contains the interaction of the electrons with external sources. The electron-ion Coulomb interaction, for instance, is considered an external source,

$$V_{\text{ext}}^{C}(\mathbf{r}_i) = \sum_{I}^{N_I}\frac{Z_I}{|\mathbf{r}_i - \mathbf{R}_I|}, \tag{1.2}$$

with $\mathbf{R}_I$ the parameters corresponding to the N_I ionic lattice sites. Other possible terms that would belong to $V_{\text{ext}}(\mathbf{r}_i)$ are the Zeeman coupling of the electron spin to an external magnetic field or the relativistic spin-orbit coupling. All these terms involve just one-body operators of the electron position variable. In contrast, the third term in Eq. (1.1) is a two-body electron operator that takes into account the electron-electron Coulomb interaction. Finally, E_{II} is a constant energy term coming from the ion-ion Coulomb interaction of the fixed ionic lattice.

The usual way to proceed in quantum mechanics is to solve the Schrödinger equation associated to the Hamiltonian (1.1). Due to the two-body electron-electron interaction term, however, there is no general solution for such an equation, and one has to assume some approximation in order to proceed. In this work, we consider the density functional theory (DFT) for such a task. Within this approach, the interacting many-body problem represented by Eq. (1.1) is substituted by a non-interacting one which can be more easily solved.

1.1.1 Density Functional Theory

In 1964 Hohenberg and Kohn proved two basic theorems [18] regarding the electron many-body problem of Eq. (1.1). They showed that the total energy of the system is a functional of the electron density, n, and that the minimum of this energy functional, E[n], corresponds to the exact ground state density, n_0. Furthermore, they proved that n_0 uniquely determines any external potential acting on the electrons. These theorems do not provide a way to extract the electronic properties of the system, but they show that the knowledge of the ground state density is sufficient for this. At this point, the Kohn-Sham ansatz proves to be useful: *an auxiliary system*

---

[1] Unless otherwise stated, atomic units will be used throughout the work, so that $e = \hbar = m_e = 4\pi\epsilon_0 = 1$.

made of non-interacting electrons can be defined whose ground state density is equal to the ground state density of the interacting many-body system. In other words, this ansatz states that one can define a fictitious system made of non-interacting particles having the same ground state density as the real interacting system, no matter how complicated the interaction is. The great advantage of this approach is that it opens the way to substitute the difficult many-body problem represented by Eq. (1.1) by an auxiliary system that can be more easily solved.

The Schrödinger equation associated to this auxiliary system is named the Kohn-Sham (KS) equation and contains only one-body operators, [2]

$$\left(-\frac{1}{2}\nabla^2 + V_{\text{eff}}(\mathbf{r})\right)\phi_\alpha(\mathbf{r}) = \epsilon_\alpha \phi_\alpha(\mathbf{r}). \tag{1.3}$$

The solution of this equation are the KS eigenvalues ϵ_α and eigenfunctions $\phi_\alpha(\mathbf{r})$, respectively, with α a set of quantum numbers that we will determine in short. The potential $V_{\text{eff}}(\mathbf{r})$ in Eq. (1.3) is a one-body effective potential that acts on each electron of the auxiliary system,

$$V_{\text{eff}}(\mathbf{r}) = V_{\text{ext}}(\mathbf{r}) + V_{\text{H}}(\mathbf{r}) + V_{\text{xc}}(\mathbf{r}). \tag{1.4}$$

Above, $V_{\text{H}}(\mathbf{r})$ is the so-called Hartree potential,

$$V_{\text{H}}(\mathbf{r}) = \int \mathrm{d}\mathbf{r}' \frac{\mathrm{n}(\mathbf{r}')}{|\mathbf{r}-\mathbf{r}'|}, \tag{1.5}$$

which represents the classical Coulomb interaction among the electrons and takes into account great part of the long ranged electronic interactions. The third term in Eq. (1.4) is the so-called exchange-correlation potential. The success of DFT lies on the ability of incorporating the main many-body effects into this last term. By far, the two most common and widely used methods for approximating the exchange and correlation effects are the Local Density Approximation (LDA) [19] and the Generalized Gradient Approximation (GGA) [20]. The LDA is based on the electron density of the homogeneous electron gas (HEG) [21] and assumes that the exchange-correlation effects are local in character, while the GGA incorporates the gradients of the density evaluated at each point in real space, hence it is a semi-local approximation. The reader is referred to [22] and references therein for a full review of the different types of approximations for the exchange and correlation effects.

1.1.2 Periodicity of the potential

An ideal solid is built by the periodic repetition of its unit cell, which is defined by three real-space vectors, $\{\mathbf{a}_1, \mathbf{a}_2, \mathbf{a}_3\}$, the so-called direct lattice.

---

[2] From now on we use $\mathbf{r}$ as the position variable of any electron.

As electrons are physically placed into this periodic structure, the potential felt by the electrons is also periodic. This is reflected in the effective potential entering the KS equation as

$$V_{\text{eff}}(\mathbf{r}) = V_{\text{eff}}(\mathbf{r}+\mathbf{R}), \tag{1.6}$$

where $\mathbf{R}$ is a lattice vector obtained through linear combinations of the direct lattice vectors,

$$\mathbf{R} = \sum_{i}^{3} l_i \mathbf{a}_i, \quad l_i \in \mathbb{Z}. \tag{1.7}$$

The periodic property of Eq. (1.6) alone is sufficient to infer valious information about the electronic properties of solids. For instance, one can prove that due to Eq. (1.6), the eigenfunctions of the KS equation (1.3) must fulfill the so-called *Bloch theorem*,

$$\phi_{n\mathbf{k}}(\mathbf{r}+\mathbf{R}) = e^{i\mathbf{k}\cdot\mathbf{R}}\phi_{n\mathbf{k}}(\mathbf{r}), \tag{1.8}$$

where we have written the set of quantum numbers as $\alpha \equiv n\mathbf{k}$. We will find useful to express the Bloch theorem in an alternative but equivalent form,

$$\phi_{n\mathbf{k}}(\mathbf{r}) = u_{n\mathbf{k}}(\mathbf{r})e^{i\mathbf{k}\cdot\mathbf{r}}, \tag{1.9}$$

with $u_{n\mathbf{k}}(\mathbf{r}) = u_{n\mathbf{k}}(\mathbf{r}+\mathbf{R})$. Different proofs for the theorem can be found in [17, 22].

The set of functions $\phi_{n\mathbf{k}}(\mathbf{r})$ satisfying the properties above are known as *Bloch orbitals*. These are characterized by quantum numbers $\mathbf{k}$ and n. The first one is a vector that lays in the first Brillouin zone (1BZ), and it is commonly known as the crystal momentum. In the case of an ideal crystal, $\mathbf{k}$ is usually discretized by applying the periodic Born-von Karman conditions which restrict its values to

$$\mathbf{k} = \sum_{i}^{3} \frac{m_i}{N_i}\mathbf{b}_i. \tag{1.10}$$

In Eq. (1.10), $\mathbf{b}_i$ are the three primitive reciprocal vectors fulfilling $\mathbf{a}_i \cdot \mathbf{b}_j = 2\pi\delta_{ij}$, $m_i \in \mathbb{Z}$ and N_i the number of lattice sites in the direction i.

The second quantum number appearing in Eq. (1.8), n, is the band index. Following the new notation, eigenvalues of the KS equation are now depicted as $\epsilon_n(\mathbf{k})$.

1.1.3 Plane wave basis

Eq. (1.8) shows that the values of the KS orbitals at points $\mathbf{r}$ and $\mathbf{r}+\mathbf{R}$ differ just by a phase factor $e^{i\mathbf{k}\cdot\mathbf{R}}$. We note that this phase factor is a plane wave, which in the Dirac's notation is denoted as $|\mathbf{k}\rangle$, with

$$\langle \mathbf{r} \,|\, \mathbf{k} \rangle = \frac{1}{V}e^{i\mathbf{k}\mathbf{r}}. \tag{1.11}$$

Thus, plane waves seem a natural basis for expanding the KS orbitals. Working again in the Dirac's notation, we can write this expansion as

$$|\phi_{n\mathbf{k}}\rangle = \frac{1}{\sqrt{V}} \sum_{\mathbf{K}} c_{n\mathbf{k}-\mathbf{K}} \, |\mathbf{k}-\mathbf{K}\rangle \, , \tag{1.12}$$

with $\langle \mathbf{r} \,|\, \phi_{n\mathbf{k}} \rangle = \phi_{n\mathbf{k}}(\mathbf{r})$ and V the total volume of the solid. In the above, $c_{n\mathbf{k}-\mathbf{K}}$ are the expansion coefficients of the plane waves, being $\mathbf{K}$ a reciprocal lattice vector that fulfills

$$e^{i\mathbf{K}\cdot\mathbf{R}} = 1. \tag{1.13}$$

The fact that the expansion in Eq. (1.12) only involves reciprocal vectors is a consequence of the periodic property of the potential (Eq. (1.6)) [17].

The plane waves of Eq. (1.11) are the solutions of the Schrödinger equation for a free particle, and describe totally delocalized states. Thus, when electrons are not tightly bound to the ions, we expect the plane wave expansion of Eq. (1.12) to yield a good description of KS states including only a few expansion coefficients. This is usually the case for metals, where conduction electrons practically lose their atomic character and become delocalized throughout the solid. In many other systems, however, the electrons are substantially more localized around the ions than in metals. Even in this case, the expansion in Eq. (1.12) can still be adequate since plane waves form a complete set, therefore one can always add more coefficients in order to improve the description of KS states. In practice, the number of plane waves included in the expansion is determined considering the kinetic energy of the plane waves,

$$\frac{1}{2}|\mathbf{k}-\mathbf{K}|^2 \leq E_{\text{cutoff}}. \tag{1.14}$$

The above quantity, E_{cutoff}, is called the cutoff energy.

1.1.4 Solving the Kohn-Sham equations

The KS equation can be numerically solved through an iterative method. In Fig. 1.1 we schematically illustrate the steps involved in the process. At first, an initial guess is made for the electron density from which the effective potential is calculated. Then, the KS equation is solved in a discrete set of **k**-points by diagonalizing in the plane wave basis

$$\left\langle \mathbf{k}-\mathbf{K}' \left| -\frac{1}{2}\nabla^2 + V_{\text{eff}}(\mathbf{r}) \right| \mathbf{k}-\mathbf{K} \right\rangle = \frac{1}{2}|\mathbf{k}-\mathbf{K}|^2 \delta_{\mathbf{K}'\mathbf{K}} + V_{\text{eff}}(\mathbf{K}'-\mathbf{K}), \tag{1.15}$$

with

$$V_{\text{eff}}(\mathbf{K}'-\mathbf{K}) = \frac{1}{V} \int \mathrm{d}\mathbf{r} e^{-i(\mathbf{K}'-\mathbf{K})\cdot\mathbf{r}} V_{\text{eff}}(\mathbf{r}) \tag{1.16}$$

the Fourier transform of the effective one-body potential. If $N(\mathbf{k})$ is the number of $\mathbf{K}$ vectors used at point $\mathbf{k}$, Eq. (1.15) represents a $N(\mathbf{k}) \times N(\mathbf{k})$

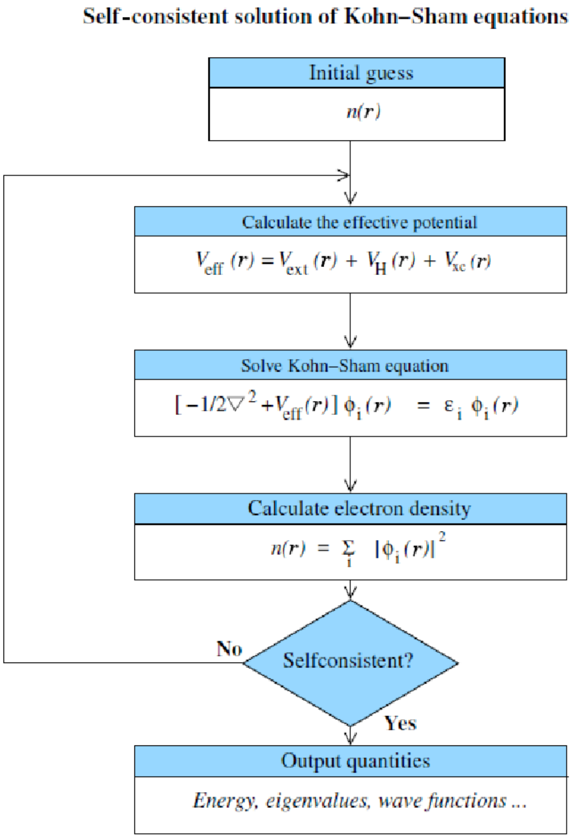

Figure 1.1: Schematic representation of the self-consistent loop for the solution of the KS equations.

matrix. In practice, this matrix can easily contain $\sim 10^5$ elements, and, therefore, it must be diagonalized by efficient computational algorithms. In this work we use the QUANTUM-ESPRESSO [23] *ab-initio* package that implements the LAPACK mathematical code [24] for this purpose.

The diagonalization of Eq. (1.15) yields the KS eigenvalues $\epsilon_n(\mathbf{k})$ and eigenfunctions $|\phi_{n\mathbf{k}}\rangle$. The latter are used to compute a new density from

$$n(\mathbf{r}) = \sum_n \sum_{\mathbf{k}}^{1BZ} f_{n\mathbf{k}} |\phi_{n\mathbf{k}}(\mathbf{r})|^2, \tag{1.17}$$

with $f_{n\mathbf{k}}$ the Fermi occupation factors. The above process is repeated until the density converges. Once convergence is reached, several physical properties, such as the total energy, forces or KS wave functions are accessible.

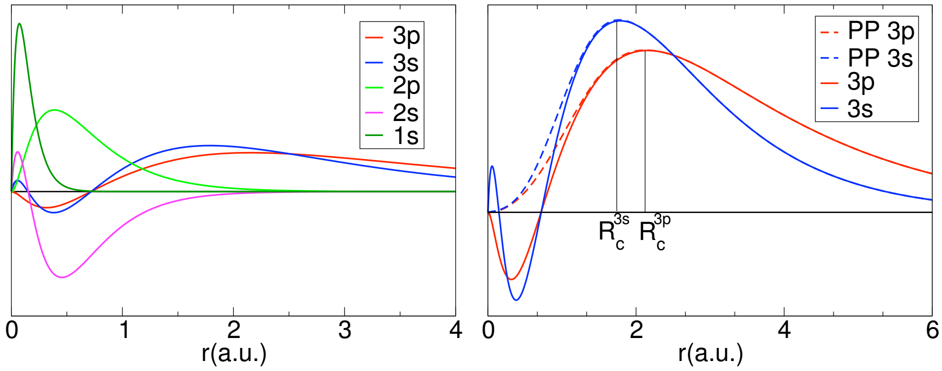

(a) (b)

Figure 1.2: (a) Exact wave functions of Si, $\phi_{1s}(r)$, $\phi_{2s}(r)$, $\phi_{2p}(r)$, $\phi_{3s}(r)$ and $\phi_{3p}(r)$. r denotes the distance from the nucleus. (b) Exact and pseudo wave functions $\phi_{3s}(r)$, $\phi_{3p}(r)$, $\phi^{ps}_{3s}(r)$ and $\phi^{ps}_{3p}(r)$. The cutoff radius for $3s$ and $3p$ is denoted by R_c^{3s} and R_c^{3p}, respectively.

1.1.5 The pseudopotential approximation

Before concluding this section, we will comment on a technique that is widely used within the DFT formalism, the so-called pseudopotential (PP) approximation [25–27]. This method takes advantage of the different roles that core and valence electrons have inside a solid. While core electrons are highly localized in the vicinity of the nucleus and contribute little to the chemical properties of the system, valence electrons are usually much more delocalized and free to interact with the environment, providing the main electronic properties to the solid. Considering the above, the PP approximation assumes that the only electrons entering the KS equation (1.3) are the valence ones. This obviously decreases the cost of solving the KS equation since the states to be considered are significantly reduced.

A PP for a given element is built by considering an isolated atom of that element. Then, the atomic Schrödinger equation is solved for all the electrons (core and valence), obtaining the corresponding eigenfunctions and eigenvalues, which are considered as exact. [3] As an illustrative example, in Fig 1.2a we show the calculated wave functions for silicon. Clearly, the $3s$ and $3p$ electronic states show a much larger contribution far from the nucleus ($r = 0$) than the rest. Therefore, it is sensible to consider these states as the valence ones.

The next step is to calculate the so-called pseudo wave function, $\phi^{\mathrm{ps}}(\mathbf{r})$, for each valence electron. An example of $\phi^{\mathrm{ps}}(\mathbf{r})$ for the $3s$ and $3p$ states of

---

[3] We notice that even the atomic Schrödinger equation for an isolated atom is a many-body problem and, therefore, some approximation is needed for the exchange-correlation energy of the atomic electrons.

silicon is shown in Fig. 1.2b. As appreciated in the figure, a pseudo wave function is required to be equal to the exact wave function beyond some cutoff radius R_c, while for $r < R_c$ it should smoothly vanish as r approaches 0. Once we make sure that the pseudo wave function fulfills these and other sensible requisites [22], a PP, $V^{\mathrm{ps}}(\mathbf{r})$, for each valence state is constructed considering the Schrödinger equation of the pseudo wave functions,

$$\left(-\frac{1}{2}\nabla^2 + V^{\mathrm{ps}}(\mathbf{r})\right)\phi^{\mathrm{ps}}(\mathbf{r}) = \epsilon\phi^{\mathrm{ps}}(\mathbf{r}). \tag{1.18}$$

From the above equation, $V^{ps}(\mathbf{r})$ is numerically calculated at every point in real space,

$$V^{ps}(\mathbf{r}) = \frac{\nabla^2\phi^{\mathrm{ps}}(\mathbf{r})}{2\phi^{\mathrm{ps}}(\mathbf{r})} + \epsilon. \tag{1.19}$$

Therefore, $\phi^{\mathrm{ps}}(\mathbf{r})$ should be nodeless (see Fig. 1.2b) in order to avoid numerical problems in the denominator.

1.2 Maximally localized Wannier functions

The main outcome of the approach presented in Sec. 1.1 are the KS states $|\phi_{n\mathbf{k}}\rangle$, which are an specific type of Bloch orbitals. In this section, we will analyze how to construct a different set of functions through linear combinations of the $|\phi_{n\mathbf{k}}\rangle$. This method was originally introduced by Gregory Wannier in 1937 [1] and has been extensively developed since then. The basis of this so-called *Wannier representation* are a set of Wannier functions (WFs) defined as

$$|\mathbf{R}n\rangle = \frac{1}{N}\sum_{\mathbf{k}} e^{-i\mathbf{k}\cdot\mathbf{R}}\,|\phi_{n\mathbf{k}}\rangle\,, \tag{1.20}$$

with $\langle\mathbf{r}\,|\,\mathbf{R}n\rangle = w_{n\mathbf{R}}(\mathbf{r})$. The above definition is basically a discrete Fourier transform of Bloch orbitals from $\mathbf{k}$-space to its reciprocal space, i.e. the real space, hence the label $\mathbf{R}$. The inverse relation is [4]

$$|\phi_{n\mathbf{k}}\rangle = \sum_{\mathbf{R}} e^{i\mathbf{k}\cdot\mathbf{R}}\,|\mathbf{R}n\rangle\,. \tag{1.21}$$

Eqs. (1.20) and (1.21) establish a linear transformation between the Bloch functions and the WFs. Both sets constitute in principle an equally acceptable basis for the description of the electronic properties, even though the WFs are not eigenstates of the Hamiltonian and, therefore, do not have a definite energy. The latter may seem a disadvantage, but it is largely compensated by a desirable property of the WFs not shared in general by Bloch orbitals: the localization in real space.

---

[4] We follow the convention $\langle\phi_{n\mathbf{k}}\,|\,\phi_{m\mathbf{k}'}\rangle = N\delta_{nm}\delta_{\mathbf{k}\mathbf{k}'}$, $\langle\mathbf{R}n\,|\,\mathbf{R}'m\rangle = \delta_{nm}\delta_{\mathbf{R}\mathbf{R}'}$.

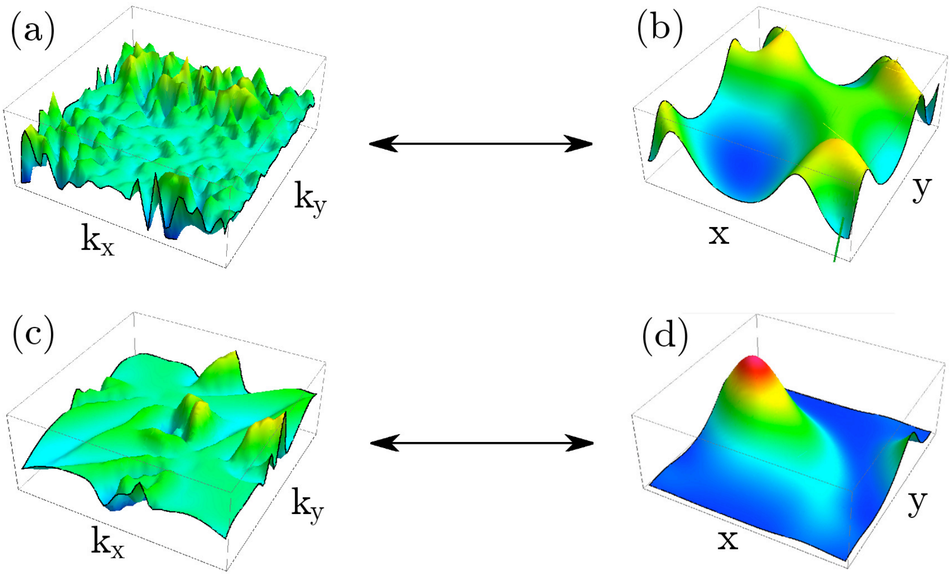

Figure 1.3: Illustrative example of the gauge freedom characteristic of Bloch orbitals. (a) and (b) show a Bloch orbital $|\phi_{n\mathbf{k}}\rangle$ obtained through an standard DFT calculation and its associated WF, respectively. (c) and (d) show respectively the transformed function $|\tilde{\phi}_{n\mathbf{k}}\rangle$, which is smooth in reciprocal space, and the associated WF, which is highly localized in real space.

1.2.1 Gauge freedom

Bloch orbitals possess an inherent phase indeterminacy in **k**-space. To illustrate this point, we note that if $|\phi_{n\mathbf{k}}\rangle$ is a valid Bloch orbital for describing the system, then

$$|\tilde{\phi}_{n\mathbf{k}}\rangle = e^{i\varphi(\mathbf{k})}\,|\phi_{n\mathbf{k}}\rangle \tag{1.22}$$

is an equally valid orbital provided that $\varphi(\mathbf{k})$ is real and periodic in reciprocal space. This is a 'gauge freedom' characteristic of Bloch orbitals, and it can be exploited in order to get WFs that are localized in real space. We recall from the basic properties of Fourier transforms that the smoother a reciprocal-space object, the more localized the associated real-space object, and vice-versa. Thus, if we choose $\varphi(\mathbf{k})$ in such a way that $|\tilde{\phi}_{n\mathbf{k}}\rangle$ is smooth in **k**-space, its Fourier transform, $|\mathbf{R}n\rangle$, will be well-localized in real space.

In order to visualize the phase indeterminacy more clearly, in Fig. 1.3a we illustrate the shape of a Bloch orbital $|\phi_{n\mathbf{k}}\rangle$ obtained through an standard DFT calculation. As it is clear from the figure, the function is characterized by random spikes all over the reciprocal space. This shows that Bloch orbitals are not smooth *per se*, but one can impose the smoothness by exploiting the gauge freedom. This is schematically illustrated in Fig. 1.3c, where the phase $\varphi(\mathbf{k})$ has been fixed in order to obtain a smooth transformed function $|\tilde{\phi}_{n\mathbf{k}}\rangle$. The WFs associated to $|\phi_{n\mathbf{k}}\rangle$ and $|\tilde{\phi}_{n\mathbf{k}}\rangle$ are respectively shown in

Figs. 1.3c-d, the latter clearly showing a much higher degree of localization in real space.

Eq. (1.22) nicely exemplifies the gauge freedom of the Bloch orbitals, but it does not describe the most general case. Consider now a manifold of M bands that remain separated by a gap from any other band all over the 1BZ. Then, one can generalize the gauge freedom of the Bloch orbitals to

$$|\tilde{\phi}_{n\mathbf{k}}\rangle = \sum_{m=1}^{M} U_{mn}(\mathbf{k})\, |\phi_{m\mathbf{k}}\rangle \,, \tag{1.23}$$

with $U_{mn}(\mathbf{k})$ a $M \times M$ unitary matrix. We notice that Eq. (1.22) corresponds to the special case of a diagonal $U_{mn}(\mathbf{k})$. In general, however, the off-diagonal elements of $U_{mn}(\mathbf{k})$ mix the contribution of several Bloch orbitals, resulting in a transformed function $|\tilde{\phi}_{n\mathbf{k}}\rangle$ that is not an eigenstate of the Hamiltonian. Thus, the quantum number n in Eq. (1.23) cannot be identified as a real band index, but corresponds to a mixture of bands.

As in the single-band case of Eq. (1.22), the goal is to construct smooth transformed functions $|\tilde{\phi}_{n\mathbf{k}}\rangle$ in order to get well-localized WFs from

$$|\mathbf{R}n\rangle = \frac{1}{N}\sum_{\mathbf{k}} e^{-i\mathbf{k}\cdot\mathbf{R}}\, |\tilde{\phi}_{n\mathbf{k}}\rangle = \frac{1}{N}\sum_{\mathbf{k}} e^{-i\mathbf{k}\cdot\mathbf{R}} \sum_{m=1}^{M} U_{mn}(\mathbf{k})\, |\phi_{m\mathbf{k}}\rangle \,. \tag{1.24}$$

For this purpose, the matrix $U_{mn}(\mathbf{k})$ should rotate the Bloch orbitals in order to cancel out their inherent discontinuities. This, however, is more subtle in the present multiband case. First, we note that degeneracies among the M bands may occur for some $\mathbf{k}$. At those points, the Bloch orbitals corresponding to the degenerate bands are not analytic, so that taking the Fourier transform may present problems. Second and most important, it is not at all obvious how should one choose the matrix $U_{mn}(\mathbf{k})$ so that every transformed function $|\tilde{\phi}_{n\mathbf{k}}\rangle$ is smooth in $\mathbf{k}$-space. We remind that $U_{mn}(\mathbf{k})$ mixes the contribution of several bands. Therefore, trying to improve the smoothness of a given band may worsen the smoothness of another one. Thus, we see the need of defining a criterion for measuring the 'global smoothness' of all the Bloch orbitals, or, analogously, a criterion for measuring the 'global localization' of the associated WFs.

1.2.2 Marzari-Vanderbilt localization functional

In 1997, Marzari and Vanderbilt [2] developed a method for determining the optimally localized set of WFs associated with a set of Bloch orbitals, later generalized to the case of entangled bands by Souza, Marzari and Vanderbilt [28]. This approach is based on the definition of a well-defined localization criterion for the WFs,

$$\Omega = \sum_{n}[\langle \mathbf{0}n \,|\, r^2 \,|\, \mathbf{0}n\rangle - \langle \mathbf{0}n \,|\, \mathbf{r} \,|\, \mathbf{0}n\rangle^2] = \sum_{n}[\langle r^2\rangle_n - \bar{\mathbf{r}}_n^2]. \tag{1.25}$$

The above quantity measures the sum of the quadratic spreads of the WFs in the home unit cell $\mathbf{R} = \mathbf{0}$, therefore Ω is commonly known as the spread of the WFs.

The way to proceed within this approach is to minimize this spread with respect to the unitary transformations $U_{mn}(\mathbf{k})$. For such a task, one needs to compute the matrix elements of the position operator [2, 29],

$$\langle \mathbf{0}n \,|\, \mathbf{r} \,|\, \mathbf{0}n \rangle = i\frac{V}{(2\pi)^3}\int d\mathbf{k} e^{i\mathbf{k}\cdot\mathbf{R}} \langle u_{n\mathbf{k}} \,|\, \boldsymbol{\nabla}_{\mathbf{k}} \,|\, u_{m\mathbf{k}} \rangle \,. \tag{1.26}$$

This is achieved by using a finite difference formula for the $\mathbf{k}$-space gradient,

$$\boldsymbol{\nabla}_{\mathbf{k}} \,|u_{m\mathbf{k}}\rangle = \sum_{\mathbf{b}} c_{\mathbf{b}} \mathbf{b} \left(|u_{m\mathbf{k}+\mathbf{b}}\rangle - |u_{m\mathbf{k}}\rangle \right) + \mathcal{O}(b^2). \tag{1.27}$$

where $\mathbf{b}$ are reciprocal vectors connecting nearest neighbor $\mathbf{k}$-points and $c_{\mathbf{b}}$ the associated weights. With the aid of the above expression, the needed quantities to calculate the matrix elements of Eq. (1.26) can be expressed in a compact matrix form,

$$M_{mn}(\mathbf{k}, \mathbf{b}) = \langle u_{m\mathbf{k}} | u_{n\mathbf{k}+\mathbf{b}} \rangle, \tag{1.28}$$

In practice, the above overlap matrix is calculated via an iterative process whereby the rotation matrix $U_{mn}(\mathbf{k})$ is updated in each iteration in order to minimize the global spread of Eq. (1.25). In this work, we make use of the WANNIER90 postprocessing algorithm [30] for such a task.

The WFs obtained through this method are named maximally localized WFs (MLWFs) and possess several desirable properties. First, they represent the set of WFs with highest degree of localization among all possible sets. The MLWFs are exponentially localized, as it has been recently shown by Panati and Pisante [31], and in most cases they are real; the exception occurs when spin-orbit coupling is taken into account, in which case the MLWFs are generally complex [32]. But, above all, this approach represents a well defined and versatile proccedure to fix the arbitrary phase of the Bloch orbitals in a large variety of systems, which explains the success of the MLWFs over other types of WFs.

1.2.3 Applications of MLWFs

The MLWFs are widely used in the solid state community due to their diverse applications. The simplest application is the interpolation of $\mathbf{k}$-dependent quantities into fine $\mathbf{k}$ meshes. To illustrate this method, consider a set of Bloch orbitals, $|\phi_{n\mathbf{q}}\rangle$, calculated *ab-initio* in a 'coarse' reciprocal-space mesh, denoted by $\mathbf{q}$, and the associated MLWFs, $|\mathbf{R}n\rangle$. By virtue of Eq. (1.21), one can transform back from the Wannier to the Bloch representation. Note however that in Eq. (1.21) there is no reference to the original reciprocal-space mesh. Thus, provided that the MLWFs are properly localized, one can accurately interpolate the Bloch orbitals into an arbitrary **k**-point even if this was not included in the original coarse mesh,

$$|\tilde{\phi}\rangle_{n\mathbf{k}} = \sum_{\mathbf{R}} e^{i\mathbf{k}\mathbf{R}} \, |\mathbf{R}n\rangle \, . \tag{1.29}$$

Performing the inverse Fourier transform of Eq. (1.29) has a negligible computational cost compared to the *ab-initio* calculation of the Bloch orbitals. Therefore, this so-called 'Wannier interpolation' procedure provides an efficient way of considering very fine **k** meshes that would be inaccesible otherwise.

The interpolated $|\tilde{\phi}_{n\mathbf{k}}\rangle$ can be used to calculate other physical quantities of interest such as band energies. Consider the representation of the Hamiltonian in the Wannier gauge,

$$H^{W}_{\mathbf{k},nm} \equiv \langle \tilde{\phi}_{n\mathbf{k}} | H | \tilde{\phi}_{m\mathbf{k}} \rangle = \sum_{\mathbf{R}} e^{i\mathbf{k}\mathbf{R}} \, \langle \mathbf{0}n \,|\, H \,|\, \mathbf{R}n \rangle \, . \tag{1.30}$$

The use of the MLWFs means that $\langle \mathbf{0}n \,|\, H \,|\, \mathbf{R}n \rangle$ is highly localized around the home unit cell, hence the above expansion yields good results including only a few **R** vectors. Then, the band energies can be interpolated into an arbitrary **k**-point simply by diagonalizing the matrix $H^{W}_{\mathbf{k},nm}$.

Apart from the interpolation scheme, MLWFs have applications in many other areas. The modern description of the electric polarization in solids [3–5], for instance, is given in terms of MLWFs. Indeed, MLWFs provide a natural way to express the electric dipole matrix elements involving the position operator, whereas in the Bloch representation this quantity is ill-defined due to the delocalization of the Bloch orbitals. Analogously, the recent description of the orbital magnetization of solids is also based on the MLWFs [6–10], providing an alternative viewpoint to the Berry phase formalism. In the context of the Hall effect, MLWFs have been successfully applied to accurately calculate the anomalous Hall conductivity in diverse magnetic systems [33]. Additionally, MLWFs demonstrate to be ideal basis functions of large-scale systems due to their maximal localization [34, 35]. Finally, MLWFs also find applications in molecular dynamics [14, 15] or electron-phonon calculations [11–13]. The reader is referred to [36] for a full review about the role of MLWFs in these and more topics.

Chapter 2

Electronic properties of surfaces with strong spin-orbit interaction

Surfaces have become an ideal testing ground for investigating the nature and effects of the relativistic spin-orbit interaction (SOI) in low dimensional systems [37–39]. As pointed in the pioneering work by LaShell and co-workers [40], the lack of inversion symmetry associated to surfaces allows for a finite spin-splitting of the so-called surface states via the SOI. Noteworthy, the typical order of magnitude for this spin-splitting is ∼100 meV, i.e. around two orders of magnitude bigger than in usual semiconductors [37]. This opens up a wide range of possible applications in the fast-growing field of spintronics, where the spin of the electron governs the charge transport and other dynamical properties [41–44].

Since the work by LaShell and co-workers, several studies performed on diverse type of surfaces have revealed exceptional effects associated to the SOI. The family of bismuth alloy surfaces, for instance, exhibits giant spin-splittings of nearly 400 meV [45, 46]. Other interesting examples include the semiconducting surfaces Tl/Si(111) [47, 48], Tl/Ge(111) [49] and Pb/Ge(111)$-\beta\sqrt{3}\times\sqrt{3}R30^\circ$ [50], among others. In these systems, bulk bands present a gap near the Fermi level, and thus electron transport properties appear strongly influenced by spin-polarized metallic surface states. Even surfaces with light element overlayers such as H/W(110) have revealed extremely complex spin-polarization structures inherited from the anisotropy of the SOI [51, 52].

In this chapter, we will provide an *ab-initio* analysis of several ground-state and excited-state electronic properties of various surfaces. In Sec. 2.1, we will introduce the basic aspects of the electron structure in surfaces together with the theoretical framework adapted to include the spin degree of freedom into the DFT formalism. As an illustrative example, we will analyze the Tl/Si(111) surface via *ab-initio* calculations of the relativistic band structure and the spin-polarization structure. Partial conclusions will be included at the end of the section.

In Sec. 2.2, we will analyze the effect of a time-dependent electromagnetic field in the low-energy electron-hole excitations at surfaces. For this purpose, we will apply a formalism based on MLWFs for calculating the transition matrix elements involving **k**-space derivatives of the Bloch functions. This approach will allow to consider very fine **k** meshes needed to accurately reproduce the details near the narrow Fermi surface associated to the surface states. We will apply the method to the Au(111) and Pb/Ge(111)$-\beta\sqrt{3}\times\sqrt{3}R30^\circ$ surfaces in Secs. 2.2.3 and 2.2.4, respectively. Main conclusions will be drawn in Sec. 2.3.

Additional material has been distributed among several Appendices. In Appendix A we include the technical details regarding how to construct (and optimize) a slab structure for modeling a surface using computational algorithms. In Appendix B we summarize the main features of the standard Rashba model [53] for a two-dimensional (2D) free-electron gas. The predictions of this simple and elegant model will be frequently referenced for comparing with our *ab-initio* results. In Appendix C we include the novel approach of Wang and co-workers [54] for expressing quantities that involve **k**-space derivatives of Bloch functions in terms of MLWFs. Finally, in Appendix D we include the derivation of the interaction Hamiltonian of Eq. (2.13) as the main perturbation term of the general relativistic Hamiltonian.

2.1 Basic electronic properties of surfaces

We begin this section by analyzing a property of surfaces that is central for this work, namely the absence of inversion symmetry with respect to the surface plane. This symmetry breakdown makes the electronic structure of surfaces rather different from that found in the bulk. Indeed, the potential near the surface reflects this inversion asymmetry and is therefore different from the bulk potential. This gives rise to certain electron states that only appear near the surface, the so-called *surface states.* These states, originally introduced by Tamm [55] and Shockley [56] in the 1930s, are solutions of the Schrödinger equation with complex momentum along the surface-perpendicular direction, z. As a consequence, surface states decay exponentially as $e^{-\operatorname{Im}[k_z]z}$ into the bulk and are therefore strongly localized near the surface plane, as schematically illustrated in Fig. 2.1.

Another important consequence of the broken inversion symmetry of surfaces can be deduced from symmetry considerations on the electron eigenvalues. We first analyze the effect of space inversion $\mathbf{r} \longleftrightarrow -\mathbf{r}$ on the electron energies $\epsilon_n^s(\mathbf{k})$, where we explicitly consider the spin quantum number s. Inversion symmetry reverses the sign of the crystal momentum while it does

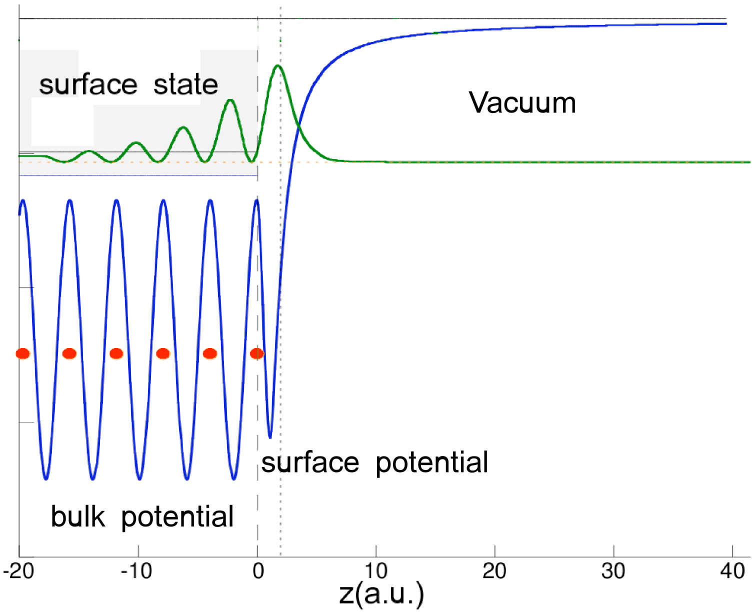

Figure 2.1: Schematic representation of the potential felt by the electrons along the surface-perpendicular direction, giving rise to the surface states.

not affect neither n nor s quantum numbers:

$$\text{Inversion symmetry: } \epsilon_n^s(\mathbf{k}) = \epsilon_n^s(-\mathbf{k}). \tag{2.1}$$

The other symmetry we consider here is time-reversal (TR). This symmetry is present in all nonmagnetic materials that do not support a net magnetic field. Its effect on the electron eigenvalues is to exchange both, the momentum and the electron spin, hence:

$$\text{TR symmetry: } \epsilon_n^s(\mathbf{k}) = \epsilon_n^{-s}(-\mathbf{k}), \tag{2.2}$$

which is konwn as the Kramers degeneracy.

If a material possess both, inversion and TR symmetry, the combination of Eqs. (2.1) and (2.2) imply:

$$\text{Inversion+TR symmetry: } \epsilon_n^s(\mathbf{k}) = \epsilon_n^{-s}(\mathbf{k}). \tag{2.3}$$

The above means that electrons with a given momentum **k** and opposite spin-state have the same energy, i.e. we say that the state is spin-degenerate.

The breakdown of the inversion symmetry relaxes the condition of Eq. (2.3) and leaves only the Kramers degeneracy (Eq. (2.2)) connecting states with opposite momenta. Thus, nonmagnetic surfaces are allowed to have spin-split states at a given momentum **k**, while the total magnetic field must still vanish due to TR symmetry. Noteworthy, we expect the spin-splitting to be most prominent in the electronic structure of the surface states, since these are the ones that feel most the inversion asymmetry of the surface.

2.1.1 Spin-orbit interaction and spin-DFT

The first measurement of spin-split surface states was performed by LaShell and co-workers in 1996 [40], who used angle-resolved photoemission spectroscopy (ARPES) techniques for analyzing the spectrum of the Au(111) surface. Rather surprisingly at that time, they discovered a splitting of $\sim$100 meV in the surface state dispersion. Furthermore, the measured splitting was not constant but varied in size depending on the momentum of the surface state. The authors interpreted the effect as a spin-splitting caused by the strong SOI associated to the surface,

$$H_{SOI} = -\frac{1}{4c^2}\boldsymbol{\sigma} \cdot \left(\boldsymbol{\nabla} V(\mathbf{r}) \times \mathbf{p}\right). \tag{2.4}$$

Above, c is the speed of light, $\boldsymbol{\sigma}$ the Pauli spin-operator and $V(\mathbf{r})$ the potential acting on the electrons, which in the KS scheme of Sec. 1.1 is equal to the effective potential $V_{\text{eff}}(\mathbf{r})$. The inversion asymmetry of surfaces enters in the SOC term through the gradient of the potential, $\boldsymbol{\nabla} V(\mathbf{r})$.

The SOI is a relativistic effect coupling the spin to the orbital motion, obtained from a Taylor series expansion of the Dirac equation up to order $(v/c)^2$ [57]. As a consequence, the SOI is only large in materials constituted by rather heavy elements (atomic number $Z \gtrsim 70$) such as Au, because only in these elements do electrons attain relativistic speeds. In surfaces made of heavy elements, the SOI induces spin-splittings of the order of 0.1 eV, i.e. about two orders of magnitude larger than in light element systems such as the semiconductors heterojunctions of silicon or germanium [37].

In order to incorporate the SOI into the DFT formalism of Sec. 1.1, the KS equation 1.3 needs to be generalized to the noncollinear spin case. This was first done by von Barth and Hedin [58], who showed that the KS equation of a noncollinear spin system takes the following form,

$$\sum_{s'=\pm} \left(-\frac{1}{2}\nabla^2 \delta_{ss'} + V_{\text{eff}}^{ss'}(\mathbf{r})\right) |\phi_{n\mathbf{k}}^{s'}\rangle = \epsilon_n^s(\mathbf{k})\, |\phi_{n\mathbf{k}}^{s}\rangle\,, \tag{2.5}$$

where we explicitly consider the spin quantum number. In this so-called spin-DFT (SDFT) formalism, the $|\phi_{n\mathbf{k}}^{\pm}\rangle$ entering the KS equation are spinor coefficients, the full KS state being a spinor orbital,

$$|\phi_{n\mathbf{k}}\rangle = \begin{pmatrix} |\phi_{n\mathbf{k}}^{+}\rangle \\ |\phi_{n\mathbf{k}}^{-}\rangle \end{pmatrix}. \tag{2.6}$$

In Eq. (2.5), the spinor coefficients $|\phi_{n\mathbf{k}}^{\pm}\rangle$ are coupled due to the spin-dependence of the effective potential, $V_{\text{eff}}^{ss'}(\mathbf{r})$, which is a 2×2 matrix. The exchange-correlation potential entering $V_{\text{eff}}^{ss'}(\mathbf{r})$ is commonly approximated within SDFT either with the spin-LDA (SLDA) [59] or spin-GGA

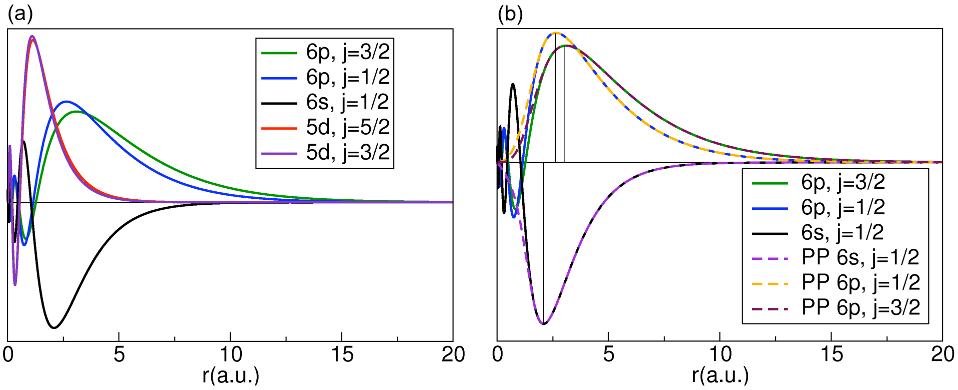

Figure 2.2: (a) Several exact wave functions of Tl: $5d_{5/2}$, $5d_{3/2}$, $6s_{1/2}$, $6p_{3/2}$ and $6p_{1/2}$ orbitals. (b) Exact (solid) and pseudo (dashed) wave functions for the $6s_{1/2}$, $6p_{3/2}$ and $6p_{1/2}$ orbitals. The cutoff radius for each state is marked by the vertical lines.

(SGGA) [60, 61]. Then, the way to proceed is analogous to the spin-independent DFT formalism, i.e. the KS equation must be iteratively solved with the aid of the density, which is a 2 × 2 matrix,

$$n_{ss'}(\mathbf{r}) = \sum_{n} \sum_{\mathbf{k}}^{1\mathrm{BZ}} f_{n\mathbf{k}} \phi^{s*}_{n\mathbf{k}}(\mathbf{r}) \phi^{s'}_{n\mathbf{k}}(\mathbf{r}). \tag{2.7}$$

The outcome of the self-consistent iterative process are the KS spinor orbitals and the associated eigenvalues.

Fully relativistic PPs

A common and widely used way to incorporate the contribution of the relativistic SOI into the SDFT formalism is the so-called fully relativistic PP approximation [62–64]. This procedure shares common features with the standard PP approximation reviewed in Sec. 1.1.5. The main difference is that in the present case, the atomic Schrödinger equation contains all relativistic effects up to order $(v/c)^2$ [64], namely the mass-velocity, Darwing and SOI terms. Precisely due to the last term, the eigenstates of the atomic Schrödinger equation are eigenstates of the total angular momentum $j = l + s$. Therefore, a fully relativistic PP must incorporate the dependence on this quantum number. [1]

As an illustrative example, in Fig. 2.2 we analyze the atomic electron wave functions of thallium, a rather heavy element with atomic number $Z = 81$. Fig. 2.2a shows the exact wave functions for the $5d_{5/2}$, $5d_{3/2}$, $6s_{1/2}$, $6p_{3/2}$

---

[1] We comment on the existence of the so-called scalar-relativistic PPs, which include all relativistic effects up to $(v/c)^2$ except the SOI.

and $6p_{1/2}$ atomic orbitals, where the subscript denotes the total angular momentum j. While $5d_{5/2}$ and $5d_{3/2}$ are quasi-degenerate, the orbitals $6p_{3/2}$ and $6p_{1/2}$ show a large difference for $r \gtrsim 2.5$ a.u.. This feature reveals that the SOI affects mainly the $6p$ orbitals, so these should be incorporated into the PP. Fig. 2.2b shows the calculated pseudo wave functions for $6s_{1/2}$, $6p_{3/2}$ and $6p_{1/2}$, which match the exact ones above some cutoff radius $R_c \sim 2.5$ a.u. and smoothly vanish as $r \rightarrow 0$. As in the standard PP approximation, the pseudo wave functions are required to be nodeless in order to avoid numerical problems when constructing the PP (see Eq. (1.19)).

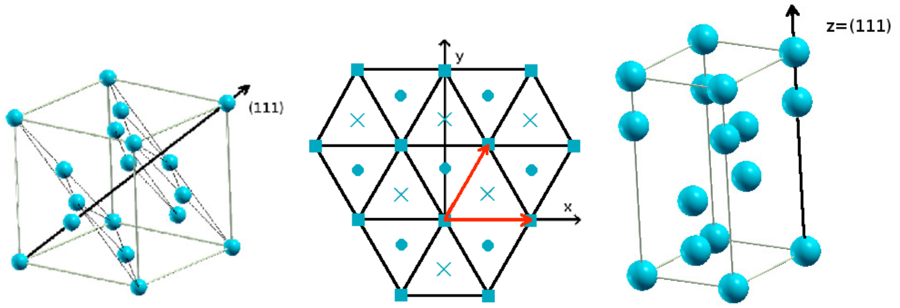

(a) (b) (c)

Figure 2.3: Diamond structure of bulk silicon. (a) Cubic unit cell with the atoms that form the honeycomb layers connected by black lines. (b) The three relative positions of the honeycomb layers are depicted by crosses, rectangles and circles. (c) Bulk unit cell used in the calculations.

2.1.2 An illustrative example: the Tl/Si(111) surface

In this section, we will apply the SDFT formalism to analyze the ground state properties of the Tl/Si(111) surface as an illustrative example. This system consists of silicon as the substrate material and a single overlayer of thallium covering the (111) termination. There are two main aspects that make this surface a particularly well suited example. First, it exhibits strong SOI effects associated to the large mass of thallium, $Z = 81$. Second, due to the semiconducting nature of silicon and the corresponding bulk band gap, the system contains 2D surface states located inside the bulk projected gap throughout the entire 1BZ.

We begin the analysis by considering the properties of bulk silicon, which crystallizes in the diamond structure as shown in Fig. 2.3a. This structure can be seen as formed by honeycomb layers stacked one above the other along the direction perpendicular to the cube diagonal, as illustrated in Fig. 2.3b. The 2D basis vectors corresponding to the honeycomb layer structure

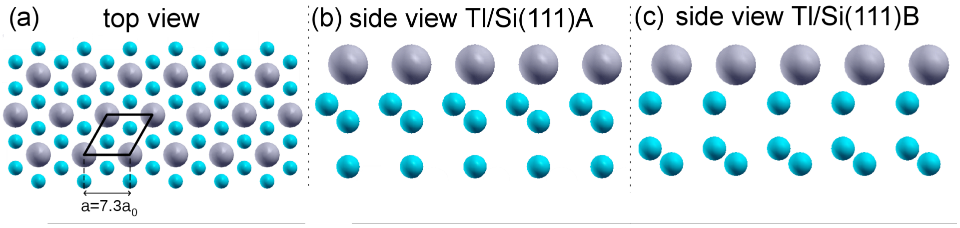

Figure 2.4: (a) Top view of the Tl/Si(111) surface. Big (gray) spheres represent the Tl surface monolayer, while the small (blue) ones are the Si substrate layers. The solid (black) lines denote the projection of the surface unit cell. (b) and (c) Side view of the Tl/Si(111)A and Tl/Si(111)B terminations corresponding to the *T4* and *H3* adsorbing sites, respectively.

are

$$\mathbf{a}_1 = a\hat{\mathbf{e}}_x \quad \text{and} \quad \mathbf{a}_2 = \frac{a}{2}(\hat{\mathbf{e}}_x + \sqrt{3}\hat{\mathbf{e}}_y), \tag{2.8}$$

with $a = 7.3$ a.u. for silicon. This geometry is symmetric under rotations of 120° around the z axis, commonly denoted as the C3 symmetry. The same honeycomb layered structure is also found in hexagonal close packed (hcp) geometries [17]. Since thallium crystallizes in hcp structure, the geometry of Si(111) is a prime candidate to adsorb a thallium surface monolayer.

The Si(111) termination possesses three possible adsorbing sites for the thallium monolayer, as depicted in Fig. 2.3b. In one of the possible configurations, the Tl surface is on top of the first Si layer. As determined by tensor low-energy electron diffraction (LEED) experiments [65], this 'on top' configuration is energetically unfavorable in comparison to the other two possible configurations. Thus, we discard it from our analysis. The other two adsorbing sites are the so-called *T4* and *H3* configurations, which are schematically shown in Figs. 2.4b-c under the names of Tl/Si(111)A and Tl/Si(111)B, respectively. Both LEED experiments and theoretical calculations [65, 66] indicate that the Tl/Si(111)A termination is the most stable, but with a tiny energy difference of $\Delta E_s \simeq 10^{-3}$ Ry per Tl atom compared to the Tl/Si(111)B structure. Thus, since the latter is an energetically competitive structure, we have also considered it in our analysis.

Computational details

The *ab-initio* calculations for analyzing the ground state electron structure of the two terminations have been performed within the SDFT framework as implemented in the QUANTUM-ESPRESSO package [23]. The exchange-correlation energy has been approximatted within the SGGA and an energy cutoff of 50 Ry has been used for the plane wave expansion. The PP approximation has been employed to include two $3s$ and two $3p$ valence electrons in the case of Si and two $6s$ and one $6p$ in the case of Tl. Following Sec.

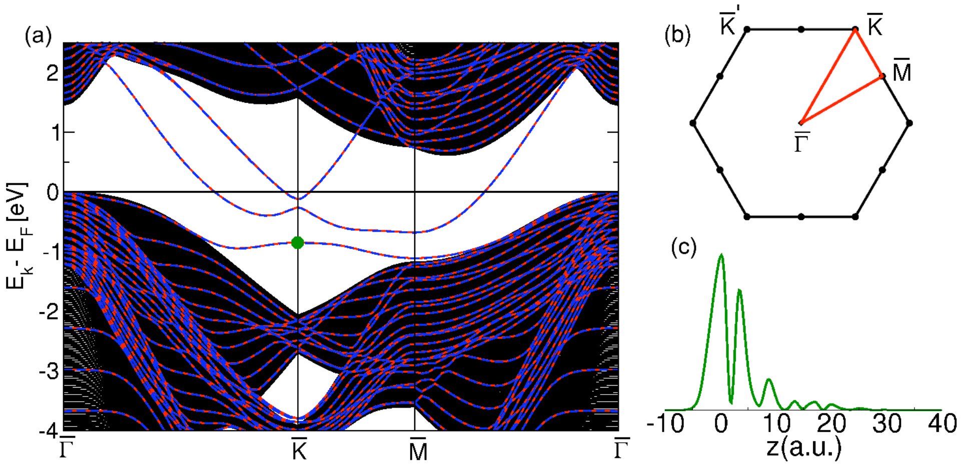

Figure 2.5: Properties of the bare Si(111) surface. (a) Electronic band structure along $\overline{\Gamma} - \overline{\mathrm{K}} - \overline{\mathrm{M}} - \overline{\Gamma}$. Red and blue (dashed) lines indicate the scalar and fully relativistic calculations, respectively. The bulk band projection is represented by the black background while the Fermi level is indicated by the horizontal black line. (b) SBZ corresponding to the honeycomb layered structure. (c) Probability amplitude $|\phi_{n\mathbf{k}}(z)|^2$ (arbitrary units) of the energetically lower surface band for $\mathbf{k} = \overline{\mathrm{K}}$ (see green dot in (a)) along the surface-perpendicular direction; $z = 0$ marks the position of the overlayer.

2.1.1, we have built fully relativistic PPs in order to take into account the effect of the SOI.

The **k** mesh considered for the integrations over the 1BZ has been 16 × 16 × 4 in the case of the bulk Si (Fig. 2.3c) and a 32 × 32 × 1 division for the surface unit cell, also called slab. The technical details regarding how to construct and optimize an slab for modeling a surface are included in the Appendix A. For the present example, we have considered an slab consisting of 24 Si layers covered by a Tl overlayer. All ionic positions have been obtained by geometry relaxation, optimizing the forces below 10^{-3} Ry a.u.$^{-1}$ per atom.

Bare Si(111) surface

Before analyzing the two terminations of the Tl/Si(111) surface, we first concentrate on the bare Si(111) surface in order to gain insight on the underlying structure. Although the Si(111) termination is not stable due to the formation of dangling bonds [67], it is still a valid example for our comparative purposes.

In Fig. 2.5 we illustrate several properties associated to the Si(111) surface. In Fig. 2.5b we have included the 2D surface Brillouin zone (SBZ), corresponding to the basis vectors in Eq. (2.8). This structure is a regular hexagon and contains 4 high symmetry points denoted as $\overline{\Gamma}$, $\overline{\mathrm{M}}$, $\overline{\mathrm{K}}$ and $\overline{\mathrm{K}'}$. [2] The first two are TR protected points, i.e. TR symmetry imposes spin-degeneracy at those points [68]. $\overline{\mathrm{K}}$ and $\overline{\mathrm{K}'}$, on the other hand, are not TR protected and spin-splitting is allowed at those points.

In Fig. 2.5a we show the calculated band structure of the bare Si(111) surface along $\overline{\Gamma} - \overline{\mathrm{K}} - \overline{\mathrm{M}} - \overline{\Gamma}$. The red and blue-dahsed lines correspond to a calculation performed with a scalar relativistic (SOI not included) and a fully relativistic (SOI included) approach, respectively. The continuum black background in the figure denotes the bulk band projection, which covers all the energies that are allowed for the electron states in the bulk. Thus, when the band structure of the Si(111) slab containing both, surface and bulk atoms, is superimposed to the bulk band projection, we can identify the contribution that comes exclusively from the surface as the bands lying outside the projection. In Fig. 2.5 we find three bands lying outside the bulk band projection in the -1.5 eV to 2.5 eV energy range. Consequently, we identify these three bands as surface bands that correspond to three well defined surface states. In order to confirm the origin of the surface bands, in Fig. 2.5c we analyze the probability amplitude of the KS state associated to the energetically lower surface band at $\overline{\mathrm{K}}$. The figure shows that the KS state is highly localized near the surface, in contrast to usual bulk states that are delocalized throughout the solid.

We notice that there is no appreciable difference between the scalar and fully relativistic calculations in the band structure of Fig. 2.5a. Therefore, we infer that the SOI is negligible in this system. This was to be expected since Si is a relatively light element with unimportant relativistic effects. Hence, even though the structure of Si(111) allows for the existence of surface states, in practice these do not spin-split due to the weakness of the SOI in this system.

The Tl/Si(111)A termination

After the introductory example, we now analyze the energetically most favored termination of the Tl/Si(111) surface, namely the Tl/Si(111)A termination (Fig. 2.4b). In Fig. 2.6 we illustrate the associated electron band structure and density of states (DOS) defined as

$$N(\epsilon) = \frac{1}{P} \sum_{n} \sum_{\mathbf{k}}^{\mathrm{SBZ}} \delta(\epsilon - \epsilon_n(\mathbf{k})), \tag{2.9}$$

with P the number of **k**-points used in the calculation. The DOS has been projected (PDOS) onto different angular momentum channels following the proccedure described in [69].

---

[2] We use an overbar to distinguish the 2D high symmetry points from usual 3D ones.

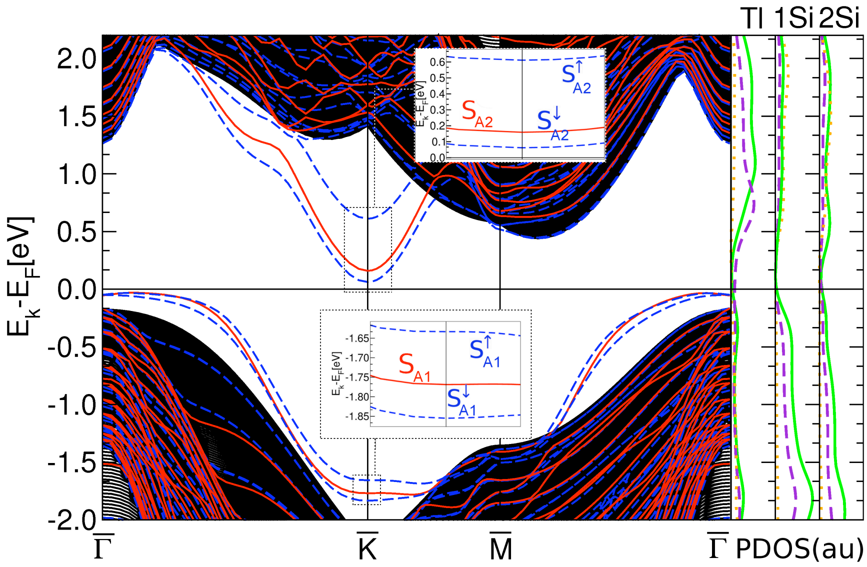

Figure 2.6: (Left) Band structure of the Tl/Si(111)A surface termination. The scalar relativistic and fully relativistic bands are represented by solid (red) and dashed (blue) lines, respectively. The continuous background denotes the bulk band projection. Inset figures show the details of the surface bands in the neighborhood of high symmetry point $\overline{\mathrm{K}}$. (Right) PDOS for the Tl surface monolayer and the first two Si layers. $np_{3/2}$, $np_{1/2}$ and $ns_{1/2}$ orbitals (principal quantum number $n = 6$ for Tl, $n = 3$ for Si) are represented by solid (green), dashed (violet) and dotted (orange) lines, respectively.

The scalar relativistic calculation produces two surface states, labeled as S_{A1} and S_{A2} (see Fig. 2.6), in contrast to the three surface states found in the bare Si(111) surface. Our calculation predicts a semiconductor state with an energy gap of approximately 0.2 eV, since neither S_{A1} nor S_{A2} bands cross the Fermi level. In contrast, the fully relativistic calculation presents four surface bands labeled as $S^{\downarrow}_{A1}$, $S^{\uparrow}_{A1}$, $S^{\downarrow}_{A2}$ and $S^{\uparrow}_{A2}$. These bands are interpreted as originating from the spin-splitting of the scalar relativistic S_{A1} and S_{A2} bands as a consequence of the SOI associated to the Tl overlayer.

It is evident from Fig. 2.6 that the SOI induces a considerable perturbation on the surface bands associated to the scalar relativistic calculation. The spin-degeneracy of the surface bands at the $\overline{\Gamma}$ and $\overline{\mathrm{M}}$ points is a consequence of the combination of the C3 rotational and the TR symmetry of the system [48]. In contrast, these symmetry considerations do not forbid a finite SOI-induced energy shift at high symmetry point $\overline{\mathrm{K}}$. The inset figures of Fig. 2.6 show the exact magnitude of the SOI close to the $\overline{\mathrm{K}}$ point, finding that the $S^{\downarrow}_{A1}$ and $S^{\uparrow}_{A1}$ bands are spin-split by approximately 0.25 eV, in good agreement with ARPES measurements [47]. In an analogous way, the $S^{\downarrow}_{A2}$

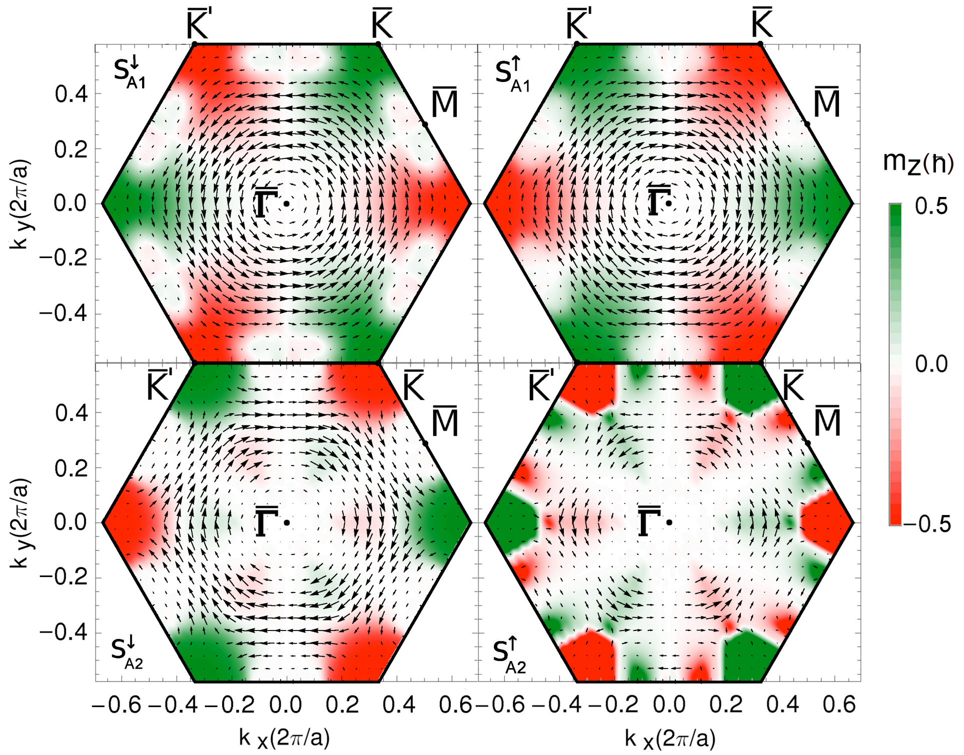

Figure 2.7: Spin-polarized structure through the entire SBZ. Arrows (black) represent the in-plane spin-polarization component, while the background reflects the surface-perpendicular component $m_{z,i}(\mathbf{k})$ (the scale ranges $[-0.5, 0.5]$).

and $S^{\uparrow}_{A2}$ bands suffer a maximum splitting of $\sim$ 0.6 eV, an extraordinarily large value for an SOI-induced energy shift. The energy band gap of this termination reduces roughly from a value of 0.2 eV in the scalar relativistic calculation to the 0.1 eV found in the fully relativistic bands.

In surfaces with such strong SOI, it is relevant to study the spin-polarization structure of the surface states, which is defined as the expectation value of the Pauli spin-operator,

$$\mathbf{m}_n(\mathbf{k}) = \frac{1}{V}\int \phi^*_{n\mathbf{k}}(\mathbf{r})\boldsymbol{\sigma}\phi_{n\mathbf{k}}(\mathbf{r})\mathrm{d}\mathbf{r}. \tag{2.10}$$

The above quantity measures the **k**-dependence of the spin quantization axis of the surface states, which due to the SOI possess a non-trivial structure. In Fig. 2.7 we show the calculated results for the four spin-split states. As depicted in the figure, a given surface state is spin-polarized in approximately the opposite direction with respect to its associated spin-split state. Note that the negligible spin-polarization around high symmetry points $\overline{\Gamma}$ and $\overline{\mathrm{M}}$ is consistent with the null spin-splitting observed in the band structure in

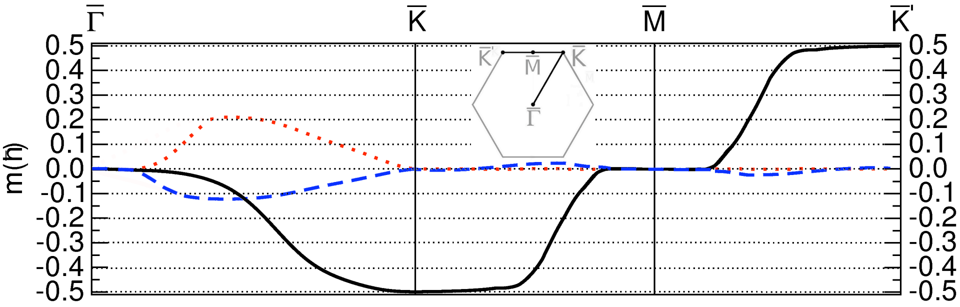

Figure 2.8: The calculated spin-polarization components $m_{x,S^{\downarrow}_{A2}}(\mathbf{k})$, $m_{y,S^{\downarrow}_{A2}}(\mathbf{k})$ and $m_{z,S^{\downarrow}_{A2}}(\mathbf{k})$ are represented along the high symmetry line $\overline{\Gamma} - \overline{\mathrm{K}} - \overline{\mathrm{M}} - \overline{\mathrm{K}}'$ by dotted (red), dashed (blue) and solid (black) lines, respectively.

these regions.

It is commonly accepted, on the grounds of the Rashba model [53] (cf. Appendix B), that the spin-polarization of surface electrons is constrained to lie parallel to the surface plane (Eq. (2.20)). Fig. 2.7 depicts an in-plane rotational spin-polarization around the $\overline{\Gamma}$ point, qualitatively resembling the Rashba picture. In addition, the figure reveals that close to $\overline{\mathrm{K}}$ and $\overline{\mathrm{K}}'$ symmetry points, the spin-state of surface electrons becomes predominantly polarized along the z direction, in agreement with recent spin-resolved ARPES (SR-ARPES) measurements [47]. This characteristic property is a consequence of the C3 rotational symmetry of the honeycomb layered structure of the surface, as it was recently shown by Ming-Hao and Ching-Ray [48].

In Fig. 2.8 we present a quantitative analysis of the spin-polarization components of the $S^{\downarrow}_{A2}$ band along the $\overline{\Gamma} - \overline{\mathrm{K}} - \overline{\mathrm{M}} - \overline{\mathrm{K}}'$ high symmetry lines. These results show that in the neighborhood of high symmetry points $\overline{\mathrm{K}}$ and $\overline{\mathrm{K}}'$, the absolute value of the z component reaches almost the maximum value, 0.5, while in-plane components become negligible. Furthermore, Fig. 2.8 indicates that electronic states around high symmetry points $\overline{\mathrm{K}}$ and $\overline{\mathrm{K}}'$ are spin-polarized in completely opposite directions. This shows that the 'valleys' associated to $\overline{\mathrm{K}}$ and $\overline{\mathrm{K}}'$ possess different spin-dependent properties, a feature that could be useful in the emerging field of 'valleytronics' [70, 71].

The Tl/Si(111)B termination

We proceed now to analyze the electronic structure of the Tl/Si(111)B termination. Fig. 2.9 shows the calculated electron band structure, where we find four spin-split surface bands ($S^{\downarrow}_{B1}$, $S^{\uparrow}_{B1}$, $S^{\downarrow}_{B2}$ and $S^{\uparrow}_{B2}$) crossing the Fermi level. Consequently, the system acquires a Fermi surface, illustrated in Fig. 2.10, which is formed exclusively by the spin-polarized surface states.

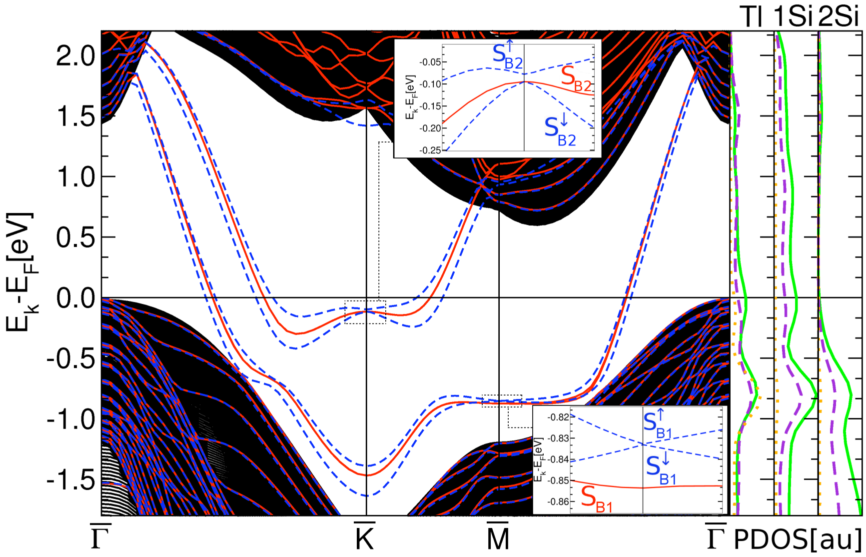

Figure 2.9: (Left) Band structure of the Tl/Si(111)B surface termination (different calculations are depicted as in Fig. 2.6). The inset figure connected to the $\overline{\mathrm{M}}$ point shows a complete spin-degeneracy of $S^{\downarrow}_{B1}$ and $S^{\uparrow}_{B1}$ bands. Inset figure connected to $\overline{\mathrm{K}}$ point reveals a quasi-degenerate configuration of $S^{\downarrow}_{B2}$ and $S^{\uparrow}_{B2}$ bands ($\Delta E_s \sim 25$ meV). (Right) PDOS for the Tl surface monolayer and the first two Si layers as in Fig. 2.6. Note that energy regions around -0.75 and -0.1 eV show non-negligible Tl 6s orbital contribution.

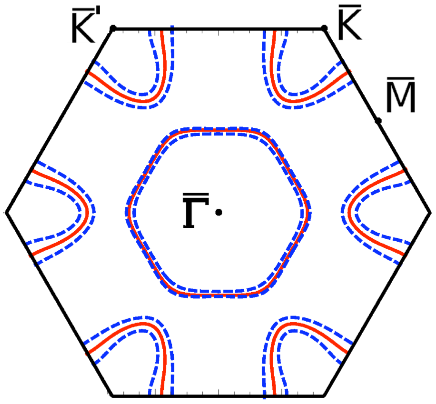

Figure 2.10: Fully spin-polarized Fermi surface of the Tl/Si(111)B surface termination. Solid (red) and dashed (blue) lines represent the Fermi crossing points of scalar relativistic and fully relativistic surface bands, respectively. The inner and outer electron pockets around $\overline{\mathrm{K}}$ and $\overline{\mathrm{K}}'$ points belong to $S^{\uparrow}_{B2}$ and $S^{\downarrow}_{B2}$ bands, while the inner and outer electron-hole pockets around the $\overline{\Gamma}$ point belong to $S^{\downarrow}_{B1}$ and $S^{\uparrow}_{B1}$ bands, respectively.

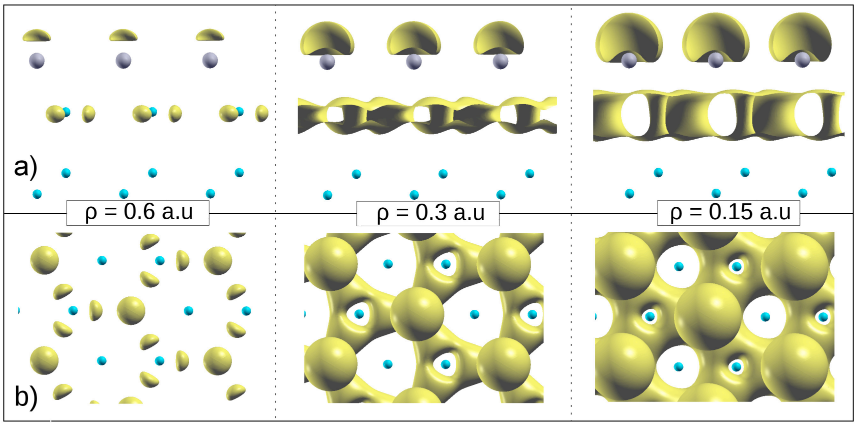

Figure 2.11: Charge distribution of $S^{\downarrow}_{B2}$ state at high symmetry point $\overline{\mathrm{K}}$. Big (gray) and small (blue) spheres represent Tl and Si atoms, respectively. (a) and (b) illustrate the side and top views of the charge density isosurfaces corresponding to $\rho = 0.6$, 0.3 and 0.15 a.u. The shape of the charge distribution around Tl atoms shows a 'front lobe' associated to a sp_z hybrid orbital with a predominant s to p_z ratio. An almost identical picture is obtained for the $S^{\uparrow}_{B2}$ state.

The $S^{\downarrow}_{B2}$ and $S^{\uparrow}_{B2}$ bands form several spin-polarized electron pockets around the high symmetry points $\overline{\mathrm{K}}$ and $\overline{\mathrm{K}}'$. Additionally, the $S^{\downarrow}_{B1}$ and $S^{\uparrow}_{B1}$ bands are occupied all over the SBZ except around high symmetry point $\overline{\Gamma}$, where we find an electron-hole pocket of radius $k_F \sim 0.46$ Å^{-1} (see Figs 2.9 and 2.10). Consequently, the Tl/Si(111)B termination exhibits a strong metallic character entirely induced by the fully relativistic surface bands. The $S^{\downarrow}_{B1}$ and $S^{\uparrow}_{B1}$ states are maximally spin-split close to $\overline{\mathrm{K}}$ ($\sim$ 0.25 eV). These bands become spin-degenerate at $\overline{\mathrm{M}}$, as appreciated in the inset of Fig. 2.9. Similarly, the overall spin-splitting for the $S^{\downarrow}_{B2}$ and $S^{\uparrow}_{B2}$ surface bands is found to be of the order of 0.2 eV. Noteworthy, these bands become quasi-degenerate close to the $\overline{\mathrm{K}}$ point, where the magnitude of the splitting diminishes to a negligible but finite value of $\sim$ 25 meV (inset of Fig. 2.9).

The s orbital character of the surface electronic wave functions is indicative of a possible spin-degeneracy. The right panel of Fig. 2.9 shows the PDOS for various orbital components. We find that the Tl 6s orbitals represent the largest contribution to the PDOS at approximately -0.75 eV. Similarly, we find a non-negligible contribution of these orbitals at around -0.1 eV. These two energy regions with non-negligible Tl 6s contribution coincide with the energy regions of the inset figures of Fig. 2.9.

In order to deepen in the analysis of quasi-degeneracy at $\overline{\mathrm{K}}$ and the Tl s orbital contribution, in Fig. 2.11 we illustrate several isosurfaces of the

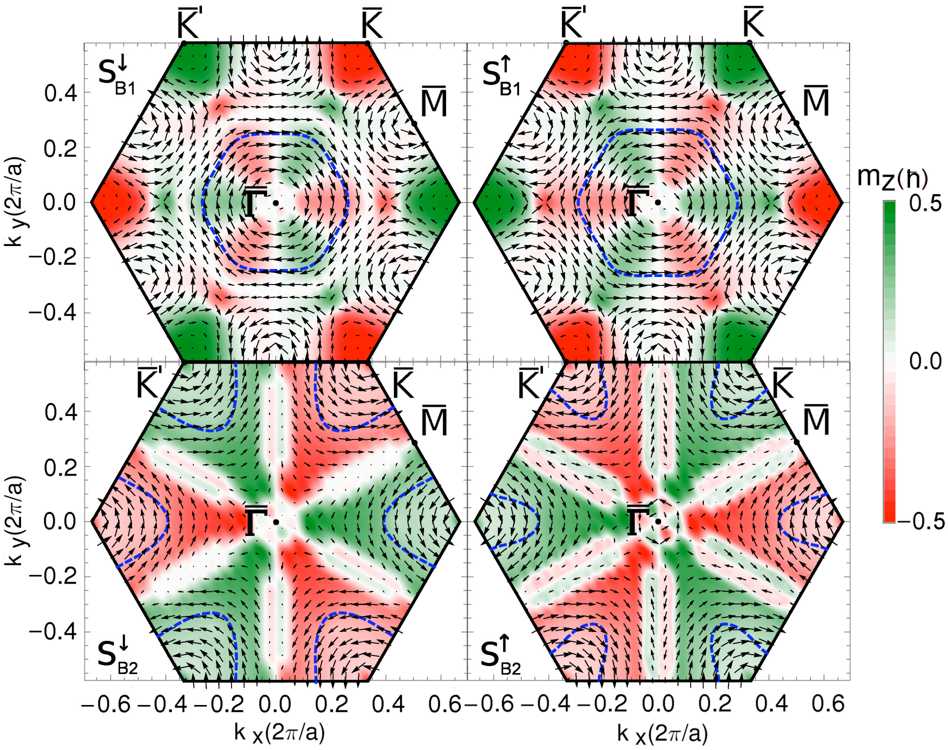

Figure 2.12: Spin-polarized structure through the entire SBZ. Arrows (black) represent the in-plane spin-polarization component, while the background reflects the surface-perpendicular component $m_{z,i}(\mathbf{k})$. The Fermi surface for each state is depicted by the dashed (blue) lines.

k-dependent charge density,

$$\rho_{n\mathbf{k}}(\mathbf{r}) = |\phi_{n\mathbf{k}}(\mathbf{r})|^2, \tag{2.11}$$

for $n = S^{\downarrow}_{B2}$ state at high symmetry point $\overline{\mathrm{K}}$. As demonstrated in the figure, this surface state is highly localized within the first two layers of the slab, where relativistic effects prevail. Close to Tl atoms, the charge distribution shows a characteristic 'front lobe' shape associated to an atomic sp_z hybrid orbital. The relatively large isosurface volume of the 'front lobe' indicates that the s character predominates over the p_z one. Interestingly, close to the $\overline{\mathrm{M}}$ point, very similar charge distributions are found for the $S^{\downarrow}_{B1}$ and $S^{\uparrow}_{B1}$ states. Therefore, we are in position to conclude that the Tl 6s character is predominant in the spin-degenerate regions.

Following with the analysis of the surface state properties, in Fig. 2.12 we present the calculated spin-polarization for the different surface states of the Tl/Si(111)B termination, exhibiting a far more complex structure than in the previous termination. In agreement with symmetry considerations, the spin is found to be 100% polarized along the surface-perpendicular direction at high symmetry points $\overline{\mathrm{K}}$ and $\overline{\mathrm{K}}'$, its orientation being reversed going from one point to the other. We find an important contribution of the z spin-polarized component over the entire SBZ, specially for the $S^{\downarrow}_{B2}$ and $S^{\uparrow}_{B2}$ states. The calculated Fermi surface extends over regions where the in-plane spin-polarization is combined with an important surface-perpendicular contribution (see Fig. 2.12). Noteworthy, the spin-polarization reverses its orientation over different electron pockets, providing the Tl/Si(111)B termination with interesting transport properties.

2.1.3 Partial conclusions

In this section we have analyzed the main features of the ground-state electron properties of surfaces with strong SOI, using the Tl/Si(111) surface as an illustrative example. The *ab-initio* calculations presented here have shown the impact of this relativistic effect on the electronic structure of the surface states. We have found that the SOI induces a spin-splitting as big as 0.6 eV on the surface bands, a value comparable to nonrelativistic contributions such as the kinetic or exchange-correlation energies. Similarly, the analysis of the spin-polarization structure has also shown remarkable effects associated to the SOI. In particular, we have found a predominant contribution of the surface-perpendicular spin-polarization component in a large area of the SBZ, a feature that completely departs from the standard Rashba model. These results are in very good agreement with experimental ARPES and SR-ARPES measurements [47], proving the adequacy of the SDFT approach for the analysis of the SOI in surfaces.

2.2 Spin-flip excitations via time-dependent electric fields

In this section, we analyze the transitions induced by a time-dependent electric field on spin-split surface states. For this purpose, we combine ground-state *ab-initio* calculations within the SDFT formalism and time-dependent first order perturbation theory. The matrix elements associated to these transitions involve **k**-space derivatives of the KS orbitals. As shown in Sec. 1.2, these type of orbitals possess an inherent phase indeterminacy in reciprocal space that make the **k**-space derivatives ill-defined in this representation. To overcome this problem, we make use of the Wannier representation introduced in Sec. 1.2, allowing the calculation and **k**-space interpolation of the transition matrix elements.

This section is divided into four different parts. After the brief introduction of Sec. 2.2.1, in Sec. 2.2.2 we present the formalism for calculating the spin-flip excitations. In Secs. 2.2.3 and 2.2.4, we apply the formalism to two different systems, the Au(111) and the Pb/Ge(111)$-\beta\sqrt{3}\times\sqrt{3}R30^\circ$ surfaces, respectively. The former is considered as the realization of the Rashba model, hence it serves as a test example. The Pb/Ge(111)$-\beta\sqrt{3}\times\sqrt{3}R30^\circ$ surface, on the other hand, shows a much more complex structure, proving the usefulness of the *ab-initio* approach.

2.2.1 Brief introduction

Due to the strong effects induced by the SOI in surfaces, these systems attract a great deal of interest as potential candidates for spintronic devices, where the spin of the electron governs the charge transport and other dynamical properties [41–44]. One particularly appealing aspect in this field is the possibility of manipulating the electron spin by means of externally applied electric fields [41]. The basic idea in this scenario is to control the spin orientation by inducing spin-flip excitations among the spin-split surface states [72]. In practice, this can be done using electric fields that couple to the electron velocity, which becomes spin-dependent due to the strong SOI of surfaces [73]. Given that electric fields can be easily created and manipulated inside semiconductor devices, this mechanism offers great perspectives for future applications.

2.2.2 Theoretical approach

We consider the effect of an external time-dependent electromagnetic field (EMF) with frequency ω and wavevector $\mathbf{q} = q\hat{\mathbf{e}}_z$ propagating along the surface-perpendicular direction z. This EMF is described by the classical vector potential field

$$\mathbf{A}^{(\alpha)}_{\text{ext}}(\mathbf{r},t) = \mathbf{A}^{(\alpha)}_0 e^{i\mathbf{q}\cdot\mathbf{r}} e^{-i\omega t} + \mathbf{A}^{(\alpha)*}_0 e^{-i\mathbf{q}\cdot\mathbf{r}} e^{i\omega t}. \tag{2.12}$$

Above, α stands for the polarization of the external field and $\mathbf{A}^{(\alpha)}_0$ is a vector constrained to the (x, y) plane. Throughout the work, we will consider x and y linearly polarized, $\mathbf{A}^{(x)}_0 = A_0\hat{\mathbf{e}}_x$ and $\mathbf{A}^{(y)}_0 = A_0\hat{\mathbf{e}}_y$, as well as right (R) and left (L) circularly polarized light, $\mathbf{A}^{(R,L)}_0 = A_0(\hat{\mathbf{e}}_x \pm i\hat{\mathbf{e}}_y)/\sqrt{2}$.

In surfaces with strong SOI, the leading term of the interaction Hamiltonian between an electron and the external field is [72],

$$\mathrm{H}_{\text{int}}(t) = -\frac{1}{c}\mathbf{v}\cdot\mathbf{A}^{(\alpha)}_{\text{ext}}(\mathbf{r},t), \tag{2.13}$$

with $\mathbf{v}$ the electron velocity operator,

$$\mathbf{v} = \frac{\partial\mathbf{r}}{\partial t} = -i\left[\mathbf{r}, H_0\right] = \boldsymbol{\nabla}_{\mathbf{p}}H_0, \tag{2.14}$$

and H_0 the ground-state Hamiltonian that incorporates the SOI. The derivation of Eq. (2.13), known as the electric coupling, is included in the Appendix D. As it is also shown in this Appendix, the electron velocity operator acquires a spin-dependent term as a consequence of the SOI,

$$\mathbf{v} = \mathbf{p} - \frac{1}{4c^2}\boldsymbol{\sigma} \times \boldsymbol{\nabla} V(\mathbf{r}), \tag{2.15}$$

with $\mathbf{p}$ the usual canonical contribution. Due to the spin-dependence of $\mathbf{v}$, the interaction Hamiltonian of Eq. (2.13) can induce transitions between spin-split surface states with opposite spin-polarization, i.e. spin-flip transitions.

The transition rate associated to this process can be calculated with the aid of the Fermi's golden rule. Considering the absorption of a photon through the term $\mathbf{A}_0^{(\alpha)} e^{-i\mathbf{q}\cdot\mathbf{r}} e^{-i\omega\cdot t}$ in Eq. (2.12), and working in the electric dipole approximation ($\mathbf{q} \to 0$ limit), the first order transition rate is given by

$$\begin{aligned}\gamma_{mn}^{(\alpha)}(\omega) =& 2\pi \int \left(f_{m\mathbf{k}} - f_{n\mathbf{k}}\right) |C_{mn}^{(\alpha)}(\mathbf{k})|^2 \\ &\times \delta(\epsilon_n(\mathbf{k}) - \epsilon_m(\mathbf{k}) - \omega) \frac{d^2\mathbf{k}}{(2\pi)^2},\end{aligned} \tag{2.16}$$

with the transition matrix elements

$$C_{mn}^{(\alpha)}(\mathbf{k}) = -\frac{1}{c}\mathbf{A}_0^{(\alpha)} \cdot \langle \phi_{m\mathbf{k}} | \, \mathbf{v} \, | \phi_{n\mathbf{k}} \rangle \, . \tag{2.17}$$

One possible way to proceed is to consider the expression of Eq. (2.15) for the velocity operator and compute the above matrix elements. However, this approach has an important drawback, namely that the calculated matrix elements cannot be interpolated in reciprocal space as a consequence of the phase indeterminacy characteristic of Bloch orbitals (cf. Sec. 1.2). Therefore, this means that all quantities entering the integral of Eq. (2.16) have to be calculated *ab-initio* at each $\mathbf{k}$-point. This integral, however, is very sensitive to the details of the Fermi surface structure associated to the spin-split surface states. In order to contribute to this integral, one of the states must be empty while the other must be occupied, as schematically depicted in Fig. 2.13. Therefore, the $\mathbf{k}$-space area contributing to the integral is rather small and, as a result, very fine $\mathbf{k}$-point meshes are usually required to yield converged results. The computational cost of this type of fine mesh *ab-initio* calculation can be very demanding [33, 54, 74–76].

In order to overcome this problem, here we make use of the Wannier interpolation scheme. Instead of using the expression of Eq. (2.15) for the velocity operator, we proceed by expanding the commutator $[\mathbf{r}, \mathrm{H}_0]$ in Eq. (2.14). Then, the matrix elements of Eq. (2.17) involving the position

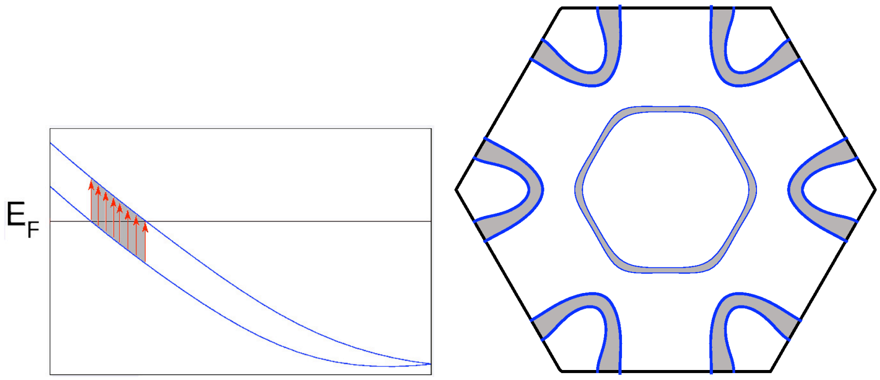

(a) (b)

Figure 2.13: Illustrative example of the **k**-space area where spin-flip excitations between spin-split states are allowed, denoted by the grey background in both figures. (a) Example of a typical band structure of spin-split surface states, indicated by blue lines. (b) Fully relativistic Fermi surface of Tl/Si(111)B, see Fig. 2.10. The blue lines indicate the cuts of the spin-split states at the Fermi level.

operator can be cast into the following form (see Eq. (1.26)),

$$C^{(\alpha)}_{mn}(\mathbf{k}) = -\frac{\big(\epsilon_n(\mathbf{k}) - \epsilon_m(\mathbf{k})\big)}{c}\mathbf{A}^{(\alpha)}_0 \cdot \langle u_{m\mathbf{k}}| \boldsymbol{\nabla}_{\mathbf{k}} |u_{n\mathbf{k}}\rangle \, . \tag{2.18}$$

The term $\langle u_{\mathbf{k}m}| \boldsymbol{\nabla}_{\mathbf{k}} |u_{\mathbf{k}n}\rangle$ in the right hand side is the so-called generalized Berry connection [77] associated to the spin-split states, which introduces a **k**-space derivative that is ill-defined in the Bloch representation. This problem can be fixed by expressing the matrix elements of Eq. (2.18) in the Wannier representation. The details of this procedure are included in Appendix C, following the novel approach by Wang and co-workers [54]. In this formalism, the use of MLWFs assures the smoothness of the matrix elements $C_{mn}(\mathbf{k})$, so that they can be interpolated into a fine **k** mesh. This process involves a routine application of the fast Fourier transform (FFT) algorithm, which represents an inexpensive computational cost compared to a full *ab-initio* calculation. Therefore, this approach is particularly appropriate for converging the integral of Eq. (2.16) that requires a large number of **k**-points.

To conclude with the theoretical analysis, let us note that the generalized Berry connection of Eq. (2.18) associated to the spin-split states is not in general null due to the spin noncollinearity induced by the SOI, as shortly illustrated in the next lines. Let us begin by considering a system without SOI and subjected to a constant magnetic field along the z axis. In these conditions, the spinor states would be collinearly polarized along the

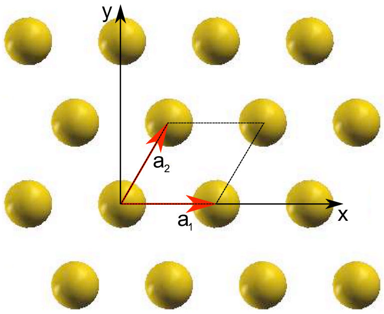

Figure 2.14: Top view of the Au(111) surface. [80] Gold atoms are represented by the spheres (yellow). The big (red) arrows denote the 2D direct lattice.

z axis, i.e. we would have $u_{\mathbf{k}n}(\mathbf{r}) = g_{\mathbf{k}n}(\mathbf{r})\begin{pmatrix}1\\0\end{pmatrix}$ and $u_{\mathbf{k}m}(\mathbf{r}) = g_{\mathbf{k}m}(\mathbf{r})\begin{pmatrix}0\\1\end{pmatrix}$. Then, since the momentum operator $\boldsymbol{\nabla}_{\mathbf{k}}$ is diagonal in the spin-basis, one deduces that the matrix elements entering Eq. (2.18) vanish identically. This is in contrast to the situation when a finite SOI is present. This interaction induces an explicit momentum dependence of the spinor wave function, $u_{\mathbf{k}i}(\mathbf{r}) = \begin{pmatrix}g^{+}_{\mathbf{k}i}(\mathbf{r})\\g^{-}_{\mathbf{k}i}(\mathbf{r})\end{pmatrix}$. In this case, the spinor $\boldsymbol{\nabla}_{\mathbf{k}}u_{\mathbf{k}n}(\mathbf{r}) = \begin{pmatrix}\boldsymbol{\nabla}_{\mathbf{k}}g^{+}_{\mathbf{k}n}(\mathbf{r})\\\boldsymbol{\nabla}_{\mathbf{k}}g^{-}_{\mathbf{k}n}(\mathbf{r})\end{pmatrix}$ does not generally describe a spin orientation parallel to the original spinor $u_{\mathbf{k}n}(\mathbf{r})$. Therefore, an appreciable magnitude of the $\langle u_{\mathbf{k}m}|\,\boldsymbol{\nabla}_{\mathbf{k}}\,|u_{\mathbf{k}n}\rangle$ matrix elements entering Eq. (2.18) is a direct consequence of the spin noncollinearity induced by the SOI.

2.2.3 A test example: the Au(111) surface

In this section, we will apply the approach presented in Sec. 2.2.2 to calculate the spin-flip excitations induced by a time-dependent electric field in the Au(111) surface. This system is considered as the paradigm of a 2D free electron-like gas under the influence of a Rashba-type SOI term [53] (cf. Appendix B). Both theory and experiments show [37, 40, 78, 79] that ground-state properties of the Au(111) surface states, such as the spin-splitting or the spin-polarization structure, are well described in terms of the Rashba model. Thus, this system represents an ideal test example for our purposes as it allows the comparison of the calculated *ab-initio* results with model predictions.

Ground-state electron structure

We have calculated the ground-state electronic properties of the Au(111) surface using SDFT and a plane wave basis set as implemented in the QUANTUM-ESPRESSO package [23]. The convergence of the plane wave

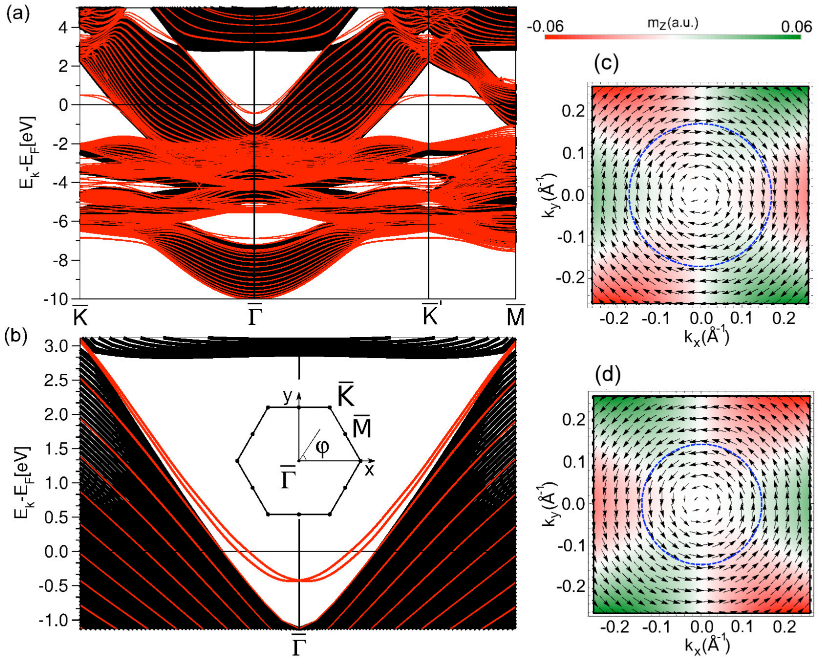

Figure 2.15: (a) Electron band structure of the Au(111) surface. Red lines represent the fully relativistic calculation, while the continuous background denotes the bulk band projection. (b) Zoom of the band structure near the $\overline{\Gamma}$ point where the metallic spin-split surface bands are located. The inset shows the details of the SBZ. (c) and (d) *Ab-initio* momentum dependent spin polarization associated to lower and higher spin-split sub-bands, respectively. Arrows represent the in-plane spin-polarization component, whereas the background color code indicates the surface perpendicular component, $m_{i,z}(\mathbf{k})$. Dashed (blue) lines indicate the calculated *ab-initio* Fermi surface associated with each surface sub-band. The radii of the circles in (c) and (d) are k_F^- and k_F^+, respectively.

basis has been achieved with an energy cutoff of 55 Ry, and the integrations over the SBZ have been performed considering a 32×32 $\mathbf{k}$ mesh. The exchange-correlation energy has been approximated using the SLDA, and the effects of the SOI have been taken into account with a fully relativistic PP for Au which includes the $5d$ and $6s$ electrons. We have modeled the Au(111) surface following the repeated slab technique (cf Appendix A) considering 21 Au layers. A top view of the honeycomb layered (111) termination is shown in Fig. 2.14. The 2D direct lattice vectors of the surface unit cell are the same as for Tl/Si(111) (Eq. (2.8)), with lattice parameter $a = 5.49$ a.u..

In Fig. 2.15a we present the calculated electron band structure of the Au(111) surface. The relativistic bands correspond to the solid (red) lines,

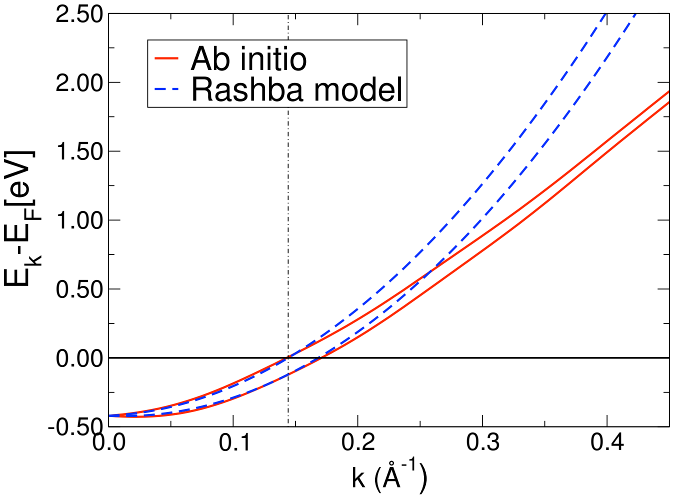

Figure 2.16: Comparison between the Rashba model prediction for the energy dispersion (Eq. (2.19)) and the calculated *ab-initio* band structure of the surface states. The Rashba parameter α_R has been fitted at $|\mathbf{k}| = 0.145\text{Å}^{-1}$, indicated by the vertical line.

while the the bulk band projection is indicated by the background continuum (black). The relativistic calculations present two spin-split metallic surface bands in the neighborhood of high symmetry point $\overline{\Gamma}$, as shown in Fig. 2.15b. Overall, the spin-splitting is of the order of ∼100 meV. Away from $\overline{\Gamma}$, the surface bands gradually spin-degenerate as they approach the bulk projection (continuum) and become resonance states. The calculated binding energy at $\overline{\Gamma}$ is 420 meV, while the spin-splittings at the Fermi level range approximately from 120 to 135 meV, corresponding to the Fermi wave vectors $k_F^{\uparrow} = 0.145\text{Å}^{-1}$ and $k_F^{\downarrow} = 0.175\text{Å}^{-1}$, respectively.

It is instructive to compare the calculated band structure of the surface states with the Rashba model energy dispersion

$$\epsilon_{\pm}(\mathbf{k}) = \frac{\mathbf{k}^2}{2m^*} \pm \alpha_R|\mathbf{k}|, \tag{2.19}$$

where ± denote the spin-split states (cf. Appendix B). This equation predicts a spin-splitting that grows linearly with $|\mathbf{k}|$: $\Delta E = 2|\mathbf{k}|\alpha_R$, with α_R the so-called Rashba parameter. An explicit value for this parameter can be obtained by extracting ΔE and $|\mathbf{k}|$ from the *ab-initio* band structure. Since we will be interested in the details close to the Fermi surface when analyzing the spin-flip transitions, we use the calculated Fermi wave vector, $|\mathbf{k}| = k_F^{\uparrow} = 0.145\text{Å}^{-1}$, and the corresponding spin-splitting, $\Delta E = 0.12$ eV, to obtain $\alpha_R = \Delta E/2|\mathbf{k}| = 0.419$ eV·Å. This value is in good agreement with recent ARPES experiments [78] measuring $\alpha_R = 0.396$ eV·Å. Besides, we obtain an effective mass of $m^* = 0.23$ (see Eq. (2.19)) from a parabolic fit to the band structure, which also agrees well with experiments, $m^* = 0.25$ [78]. Using the calculated values for α_R and m^*, in Fig. 2.16 we compare the *ab-initio* band structure of the surface states with the Rashba model energy dispersion (Eq. (2.19)). The figure shows a good agreement for energies below the Fermi level. As expected, at $|\mathbf{k}| = k_F^{\uparrow}$ the *ab-initio* and Rashba model energies coincide exactly. For $|\mathbf{k}| > k_F^{\uparrow}$, the *ab-initio* band structure ceases to grow linearly and, furthermore, it starts decreasing, clearly deviating from the Rashba energy dispersion.

We now analyze the spin-polarization structure (Eq. 2.10) of the surface states, illustrated in Figs. 2.15c and 2.15d. Both surface states are spin-polarized in practically the opposite direction in agreement with spin-resolved ARPES measurements [40, 78], and describe a circular spin structure around the $\overline{\Gamma}$ point following the Rashba model,

$$\mathbf{m}_{\pm}(\mathbf{k}) = \pm\frac{1}{2}\begin{pmatrix} \sin\varphi \\ -\cos\varphi \\ 0 \end{pmatrix}. \tag{2.20}$$

Our calculations confirm that $\boldsymbol{m}_i(\mathbf{k})$ is almost parallel to the surface for $|\mathbf{k}| \lesssim k_F^{+}$, which is the region where the Rashba model is expected to properly describe the properties of the surface states. Instead, the calculated surface-perpendicular component ($m_{z,i}(\mathbf{k})$) acquires a finite value for $|\mathbf{k}| \gtrsim k_F^{+}$, indicating a departure from the Rashba model in this region. As shown by Henk *et al.* [81], this feature is a consequence of in-plane components of the potential gradient associated with the real surface structure. In our calculations, we find that at k_F^{+}, the surface-perpendicular component represents the 3% of the total magnitude of the spin polarization.

Spin-flip excitations

We come now to analyze the spin-flip transitions induced by a time-dependent EMF on the spin-split surface states, following the approach of Sec. 2.2.2. For this purpose, in Fig. 2.17 we present the calculated spin-flip transition probability associated to the surface states,

$$P_{mn}^{(\alpha)}(\mathbf{k}) \equiv \frac{|C_{mn}^{(\alpha)}(\mathbf{k})|^2}{|\mathbf{A}_0^{(\alpha)}|^2}, \tag{2.21}$$

where the $C_{mn}^{(\alpha)}(\mathbf{k})$ are the transition matrix elements of Eq. (2.18). We notice that the transition probability as defined in Eq. (2.21) is independent of the external field intensity A_0 (see Eq. (2.17)). Figs. 2.17a-b illustrate the results corresponding to x and y linearly polarized light, respectively, while Figs. 2.17c-d correspond to R and L circularly polarized light, respectively.

Our results confirm a qualitative agreement between the *ab-initio* calculations and the Rashba model prediction. For the R and L circularly

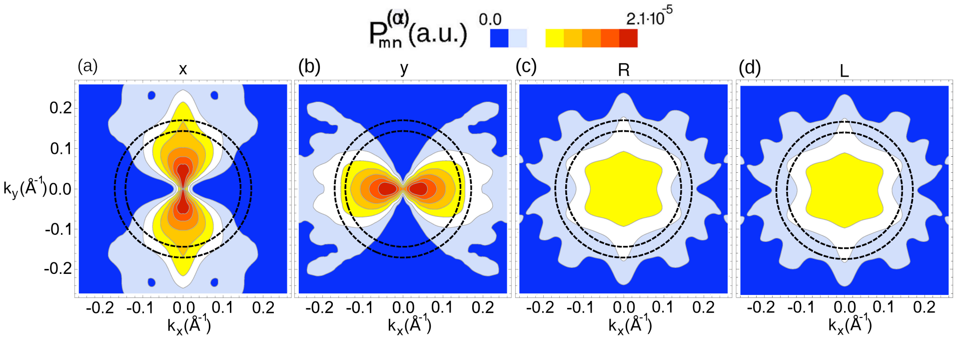

Figure 2.17: Spin-flip transition probability associated with the spin-split surface states. (a), (b), (c) and (d) show the calculated results for $\alpha = x, y, R$ and L polarized light, respectively. The solid contour lines indicate the degree of localization of the probability distribution. The dashed lines (black) denote the Fermi surface associated to the spin-polarized states.

polarized light (Figs. 2.17c and 2.17d), the calculations predict equal and highly isotropic angular distribution, i.e. our results do not show a significant dependence on φ apart from a slight hexagonal-like shape. This feature is in agreement with the Rashba model, which predicts a constant and equal transition probability,

$$P_{-+}^{(R,L)} = \frac{\alpha_R^2}{2c^2}. \tag{2.22}$$

For x and y linearly polarized light (Figs. 2.17a and 2.17b), the spin-flip transition probability is also in qualitative agreement with the sinusoidal functions predicted by the Rashba model,

$$P_{-+}^{(x)}(\varphi) = \frac{\alpha_R^2}{c^2} \sin^2 \varphi, \tag{2.23}$$

$$P_{-+}^{(y)}(\varphi) = \frac{\alpha_R^2}{c^2} \cos^2 \varphi. \tag{2.24}$$

Interestingly, our *ab-initio* calculations show a clear deviation from the Rashba model in one important aspect; the dependence of the calculated spin-flip transition probability on the momentum magnitude $|\mathbf{k}|$. This feature is particularly evident for x and y linearly polarized light (Figs. 2.17a and 2.17b), but it is also present in the case of R and L circularly polarized light (Figs. 2.17c and 2.17d). In the four cases, the spin-flip transition probability diminishes with increasing momentum. This is understood as the surface bands approaching the bulk continuum lose gradually their surface character, and is in clear contrast with the Rashba model predicting a transition probability independent of $|\mathbf{k}|$.

In Figs. 2.18a and 2.18b we analyze the probability distribution for x and y linearly polarized light along circular paths centered at high symmetry

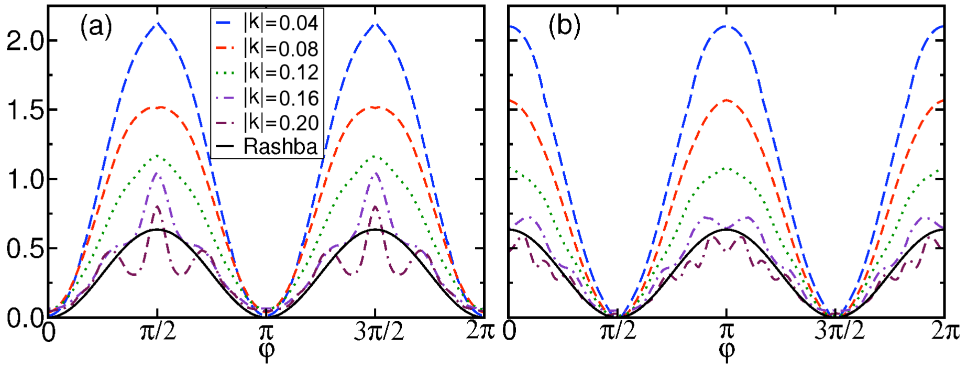

Figure 2.18: (a) and (b) Respectively, calculated $P_{mn}^{(x)}(\mathbf{k})$ and $P_{mn}^{(y)}(\mathbf{k})$ (units of 10^{-5} a.u.) along various circles centered at $\overline{\Gamma}$, each with different radius $|\mathbf{k}|$ (see inset, values in units of $2\pi/a$). The solid (black) line depicts the Rashba model prediction, which is independent of $|\mathbf{k}|$.

point $\overline{\Gamma}$. The figures show the calculated results for several magnitudes of the momentum $|\mathbf{k}|$. We observe that the calculated $P_{mn}^{(x)}(\mathbf{k})$ and $P_{mn}^{(y)}(\mathbf{k})$ closely follow the dipole-like functional shape of the Rashba model $(\sin^2\varphi, \cos^2\varphi)$, specially for small momenta, $|\mathbf{k}| \lesssim k_F^{\uparrow}$. The results in this regime differ from the Rashba model basically because the parameter α_R was fitted by considering the *ab-initio* data at $k_F^{\uparrow}$. We find that even though the order of magnitude coincides for all $|\mathbf{k}|$, the calculated spin-flip transition probability shows a remarkable modulation with respect to the Rashba model result near $k_F^{\uparrow}$.

In Fig. 2.19 we present the absorption rate associated to spin-flip excitations,

$$\Lambda_{mn}^{(\alpha)}(\omega) = \frac{\omega \cdot \gamma_{mn}^{(\alpha)}(\omega)}{\mathcal{P}}, \tag{2.25}$$

where $\gamma_{mn}^{(\alpha)}(\omega)$ is the spin-flip transition rate (Eq. (2.16)) and $\mathcal{P} = |A_0|^2\omega^2/\pi c$ the optical power per unit area of the incident field. Therefore, $\Lambda_{mn}^{(\alpha)}(\omega)$ measures the percentage of the total irradiated light absorbed in spin-flip processes. In the present example, the absorption rate has been obtained integrating the contribution of 1000×1000 interpolated $\mathbf{k}$-points, which has allowed us to consider a very fine Gaussian width of $4 \cdot 10^{-4}$ eV for the integral. The calculated results ($\alpha = x, y, R, L$) are shown as colored lines in the figure. The grey line represents the analytic Rashba model prediction (Eq. (B.17)) which is independent of both, the external field polarization and the Rashba parameter α_R. We have also applied the same broadening to this analytic result (dot-dot-dashed black line) in order to reflect the accuracy of the integration.

Fig. 2.17e shows that light is absorbed in the 120-135 meV energy range,

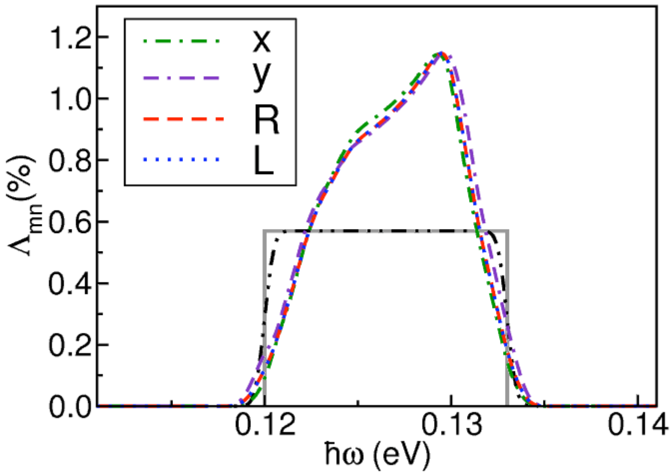

Figure 2.19: Integrated spin-flip absorption rate for the Au(111) surface. Super-imposed dashed (red), dotted (blue), dot-dashed (green) and dot-dash-dashed (purple) lines represent the calculated results corresponding to the x and y linear and R and L circularly polarized light, respectively. The constant solid (grey) and dot-dot-dashed (black) lines denote respectively the Rashba model prediction without and with broadening.

corresponding to the spin-splitting of the surface states at the Fermi level. Our calculations confirm that the absorption rate is practically independent of the external field polarization, in qualitative agreement with the Rashba model prediction. The spatial isotropy between x and y directions of Fig. 2.17e is expected since the surface states in Au(111) are mainly composed of s, p_z and d_{z^2} orbitals [78]. The equality in the absorption of R and L circularly polarized light, on the other hand, is imposed by the TR symmetry of the system [10, 71].

Fig. 2.17e reveals that the Rashba model underestimates the maximum magnitude of the spin-flip absorption rate by approximately 30% compared to our *ab-initio* results. This is a consequence of the Fermi surface structure depicted in Figs. 2.17a-d. In the **k**-space area where electron spin-flip excitations are allowed ($k_F^{\uparrow} < |\mathbf{k}| < k_F^{\downarrow}$), the calculated values for the transition probability matrix elements are $\sim$ 1-1.5 times larger than the ones predicted by the Rashba model. This feature leads to the enhancement of the calculated spin-flip absorption rate depicted in Fig. 2.17e.

2.2.4 The Pb/Ge(111)$-\beta\sqrt{3}\times\sqrt{3}R30^\circ$ surface

In this section, we apply the formalism of Sec. 2.2.2 to calculate the spin-flip excitations in the Pb/Ge(111)$-\beta\sqrt{3}\times\sqrt{3}R30^\circ$ ($\sqrt{3}$Pb/Ge(111)) surface. This system presents two well defined spin-split surface states crossing the Fermi level as measured by recent ARPES measurements [50], while the

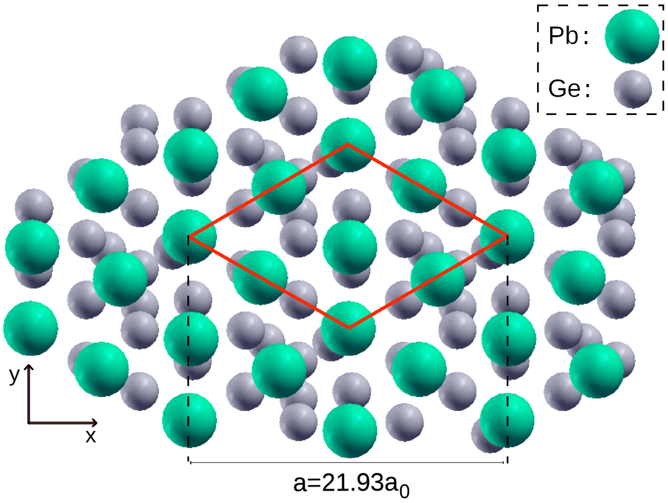

Figure 2.20: Top view of the $\sqrt{3}$Pb/Ge(111) surface [80]. The small (gray) spheres symbolize the Ge substrate layers, whereas the big (green) spheres represent the Pb surface monolayer. The solid (red) parallelogram indicates surface unit cell.

bulk substrate remains semiconducting. Thus, we face a problem involving a completely spin-polarized 2D electron gas which is essentially decoupled from the bulk, i.e. an optimum scenario for studying surface spin-flip transitions. Another interesting feature about this surface is that it does not follow the Rashba model prediction. This is so because the surface bands are located far from high symmetry point $\overline{\Gamma}$, whereas the Rashba model is expected to work at low values of the momentum. Therefore, the *ab-initio* approach is specially useful in this case.

Ground-state electron structure

We have calculated the ground-state electronic properties of the $\sqrt{3}$Pb/Ge(111) surface using SDFT and a plane wave basis as implemented in the QUANTUM-ESPRESSO package [23]. The convergence of the plane wave basis has been achieved with an energy cutoff of 40 Ry, and the integrations over the SBZ have been performed considering a 27×27 $\mathbf{k}$ mesh. The exchange-correlation energy has been approximated using the SLDA, and the effects of the SOI have been taken into account by a fully relativistic PP for Pb which includes the $6s$ and $6p$ electrons. The $\sqrt{3}$Pb/Ge(111) surface has been simulated by the repeated slab technique (cf. Appendix A) containing 14 Ge layers. In Fig. 2.20 we include a top view of the surface. The 2D direct lattice vectors conforming the surface unit cell are ($a = 21.92$ a.u.)

$$\mathbf{a}_1 = \frac{a}{2}(\hat{\mathbf{e}}_x + \frac{\hat{\mathbf{e}}_y}{\sqrt{3}}), \quad \mathbf{a}_2 = \frac{a}{2}(-\hat{\mathbf{e}}_x + \frac{\hat{\mathbf{e}}_y}{\sqrt{3}}). \tag{2.26}$$

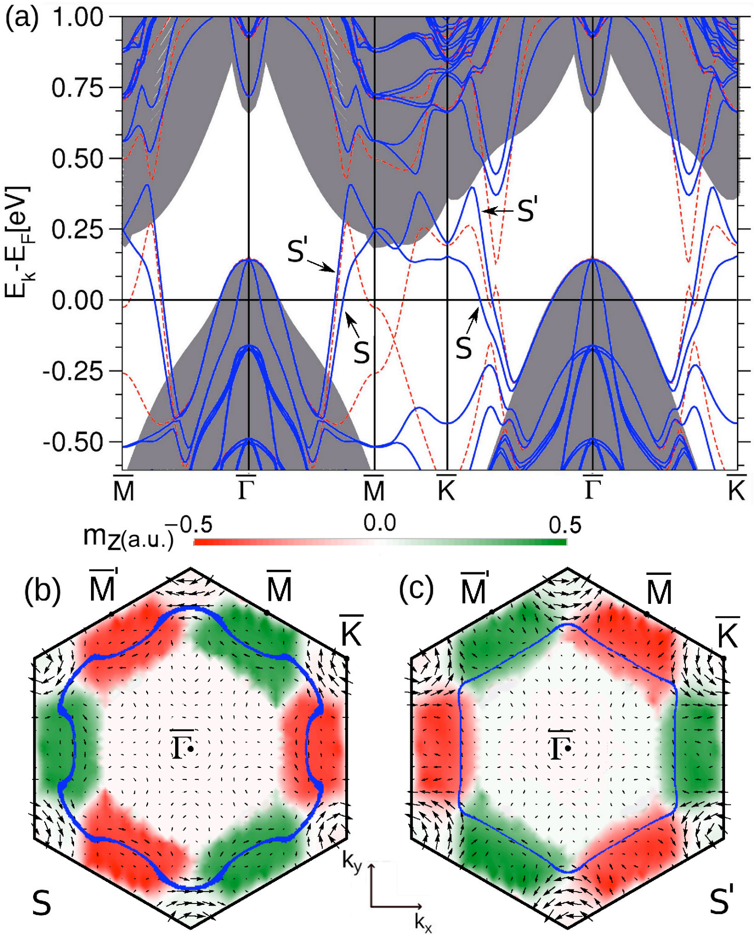

Figure 2.21: Electron structure of the $\sqrt{3}$Pb/Ge(111) surface. (a)Electron band structure of the $\sqrt{3}$Pb/Ge(111) surface. The scalar and fully relativistic bands are represented by dashed (red) and solid thick (blue) lines, respectively. The continuous background is the bulk band projection. The fully relativistic metallic surface states are labeled as S and S'. (b) and (c) Momentum dependent spin-polarization structure associated to the S and S' surface states, respectively. Arrows represent the in-plane spin-polarization component, whereas the background color code indicates the surface-perpendicular component of the magnetization, $m_z(\mathbf{k})$. The Fermi surface of each state is indicated by solid (blue) lines.

Fig. 2.21a shows the calculated band structure of the $\sqrt{3}$Pb/Ge(111) surface. While the scalar relativistic calculation (dashed) shows a single spin-degenerate surface band crossing the Fermi level, fully relativistic calculations present two spin-polarized surface bands labeled as S and S'. The SOI has a huge impact on the electron structure close to the Fermi level, such that this term cannot be treated perturbatively. Its contribution is even more important than some non-relativistic DFT terms, such as the exchange-correlation energy. In this context, the SOI completely determines the metallic character of the S and S' surface states, which exist as surface states only outside the area close to the $\overline{\Gamma}$ point, where S and S' become resonances entering the bulk projection (continuum in Fig. 2.21a). Outside this region, the SOI-induced spin-splitting is in overall of the order of 100 meV, reaching a maximum of 300 meV near the high symmetry point $\overline{\mathrm{M}}$. The calculated Fermi wave vectors along the high symmetry direction $\overline{\Gamma}-\overline{\mathrm{M}}$, $k_F^S \simeq 0.41$ Å^{-1} and $k_F^{S'} \simeq 0.37$ Å^{-1}, are in very good agreement with recent ARPES experiments reporting $k_F^S = 0.40$ Å^{-1} and $k_F^{S'} = 0.36$ Å^{-1} [50].

In Figs. 2.21b and 2.21c we present the calculated spin-polarization structure (Eq. 2.10) for the S and S' surface states in the entire SBZ. These figures demonstrate that the S and S' states are spin-polarized in almost the opposite direction, in agreement with recent SR-ARPES measurements [50]. The negligible spin-polarization around $\overline{\Gamma}$ is consistent with the overlap of the surface bands with the bulk projection (see Fig. 2.21a). In this area, the electron states become resonances with a large penetration, so that any surface effect, such as the enhancement of the SOI, is almost completely absent.

The anisotropic character of the SOI is evidenced by the highly non-collinear structure of the calculated spin-polarization for S and S'. We observe that the spin-state is polarized mainly along the surface-perpendicular direction, a phenomenon that extends to a significant area around the high symmetry points $\overline{\mathrm{M}}$ and $\overline{\mathrm{M}}'$. Such an important contribution of the out-of-plane spin-polarization is a consequence of strong in-plane gradients of the ionic potential, as in the case of the Tl/Si(111) surface. Our calculations further identify an important area of almost pure in-plane circular spin-polarization around high symmetry point $\overline{\mathrm{K}}$.

Spin-flip transitions

We come now to analyze the spin-flip transitions between the S and S' surface states. In Fig. 2.22 we show the calculated spin-flip transition probability as defined in Eq. (2.21) for linearly polarized light. The matrix elements have been interpolated into a fine 300×300 **k**-point mesh using the Wannier interpolation scheme.

We begin by analyzing the result for x linearly polarized light (Fig. 2.22a). Consistently with the band structure, the spin-flip transition probability is practically null in the neighborhood of the $\overline{\Gamma}$ point. In contrast, we find a very high localization of the spin-flip transition probability in several 'hot spots' close to the high symmetry point $\overline{\mathrm{K}}$. In comparison, the magnitude of the transition probability in these regions is two orders of magnitude larger than in the Au(111) surface (see Fig. 2.17). In order to understand the origin of these hot spots, in Fig. 2.22c we superimpose the spin-flip tran-

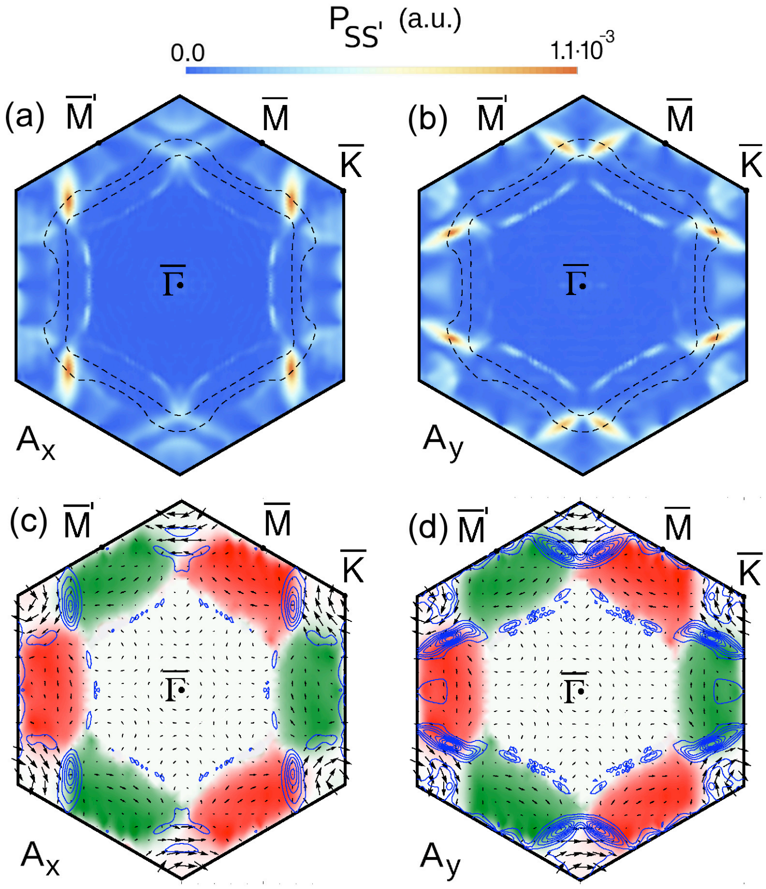

Figure 2.22: (a) and (b) show the calculated spin-flip transition probability for x and y linearly polarized light, respectively. The dashed lines indicate the Fermi surface associated with the surface states. In (c) and (d), we have respectively superimposed the transition probability shown in (a) and (b) as contour lines to the spin polarization of the S' state.

sition probability to the spin-polarization structure of the S' state. This figure shows that the hot spots are localized in the boundaries separating the surface-perpendicular and surface-parallel spin-polarized regions in the SBZ. Furthermore, we notice that the boundaries are perpendicular to the x direction, which is the direction of polarization of the incident light. In the case of y linearly polarized light, we find a similar situation: the transition probability is also distributed in several hot spots (Fig. 2.22b) that correspond to the boundaries of different spin-polarization regions (Fig. 2.22d). These boundaries are almost perpendicular to the y direction.

The above analyzed distribution of the hot spots is consistent with the expression of the transition matrix elements of Eq. (2.18). The **k**-space derivative entering this equation evaluates the variation of the wave function

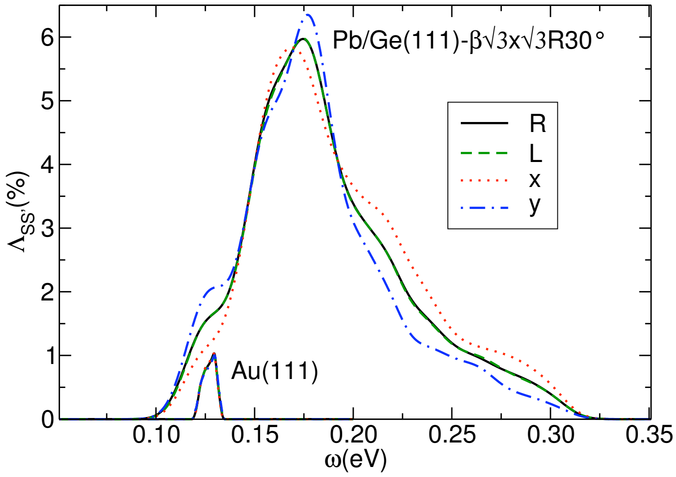

Figure 2.23: Calculated spin-flip absorption rate in $\sqrt{3}$Pb/Ge(111) and Au(111). Solid (black), dashed (green), dotted (red) and dashed-doted (blue) lines represent the results corresponding to the R and L circularly polarized and x and y linearly polarized light, respectively.

in reciprocal space. Since the spin-polarization is also a measure of the wave function through Eq. 2.10, it is sensible that the regions where the spin-polarization experiences a sudden rotation correspond to high values of the transition probability. As a further remark, this interpretation also serves to explain the dependence of the hot spots on the external field polarization.

Fig. 2.23 illustrates the calculated absorption rate (Eq. (2.16)) associated to the spin-split surface states in the $\sqrt{3}$Pb/Ge(111) surface. As shown in the figure, the absorption spectrum is bounded in the 0.1-0.3 eV energy range, corresponding approximately to the spin-splitting at the Fermi level. The spectrum presents a prominent peak close to 0.17 eV, where the spin-flip absorption rate reaches a remarkable maximum value of 6%. This result demonstrates that a significant part of the incoming light is dissipated exclusively in spin relaxation phenomena. In comparison to the Au(111) surface (Fig. 2.19), the spin-flip absorption in $\sqrt{3}$Pb/Ge(111) is one order of magnitude larger.

It is noteworthy that the bare spin-flip contribution to the absorption rate in $\sqrt{3}$Pb/Ge(111) is almost three times higher than the total absorption of a graphene layer (2.3%), where the electron spin does not play any significant role [82, 83]. Therefore, the *a priori* weaker relativistic SOI in $\sqrt{3}$Pb/Ge(111) exceeds the effect of the usually predominant non-relativistic terms such as the electric dipole mechanism. The reason why the spin-flip contribution in this system is so important is that the hot spot matrix elements (Figs. 2.22a-b) lie inside the SBZ area where the S state is occupied while S' state remains empty. In this way, the Fermi occupation factors allow electron transitions precisely where the matrix elements are maximal. From the discussion above we can conclude that a large anomalous feature associated to the enhanced spin-flip excitation mechanism should be accessible by infrared optical spectroscopy in the $0.1 - 0.3$ eV energy range.

2.3 Conclusions

Throughout this chapter we have analyzed several electronic properties associated to surfaces with strong SOI. The results presented here have shown a very good agreement with available ARPES and SR-ARPES experimental data, proving the adequacy of the SDFT approach for studiyng surface phenomena. The two main ground-state electron properties, namely the relativistic band structure and the spin-polarization structure, have provided useful information about the nature of the SOI in surfaces. We have seen, for instance, that surface states acquire a finite spin-polarization component perpendicular to the surface due to the strong in-plane gradients of the surface potential. This is a nice example of how the details of a surface can induce complex effects, and the need to employ approaches that go beyond simple standard models. The calculations presented in this chapter have also shown that the SOI can have a large impact on the energy dispersion associated to the surface states. Indeed, a spin-splitting as big as 0.6 eV has been predicted by the calculations, an extraordinarily large amount for a relativistic effect.

In the second half of this chapter we have analyzed the low-energy spin-flip excitations induced by a time-dependent EMF. The associated transition matrix elements have been calculated employing a technique based on the MLWFs, which has enabled to consider fine integration $\mathbf{k}$ meshes in order to reliably account for the details close to the Fermi level. Using this approach, we have investigated the role of the SOI on the light absorption rate of the Au(111) and $\sqrt{3}$Pb/Ge(111) surfaces. In Au(111), the magnitude of the absorption rate is similar to the prediction of the standard Rashba model (cf. Appendix B). In contrast, the calculations for the $\sqrt{3}$Pb/Ge(111) surface have revealed that the spin-flip transitions capture as much as 6% of the total incident power, representing an enhancement of one order of magnitude in comparison to Au(111). These results have shown that a substantial part of the low-energy absorption spectrum in $\sqrt{3}$Pb/Ge(111) is dominated exclusively by the spin-flip excitations associated to the spin-polarized states. We have seen that the origin of such a huge absorption rate is closely related to the strong anisotropy exhibited by the spin-polarization structure in this surface, which is one of the most important results presented in this Chapter. In conclusion, we have predicted that a clear fingerprint of the spin-flip absorption mechanism should be accessible in the infrared range, a feature that may be worth verifying experimentally.

Chapter 3

Plasmon dispersion in sodium under pressure

Pressure can be effectively used to tune the properties of materials. A clear example is provided by materials which, even though at ambient pressures do not possess remarkable superconducting properties, they become good superconductors at high pressures. This is the case, for instance, of lithium and calcium. These simple alkalies are bad superconductors at ambient pressure, with a critical temperature, T_c, of the order of mK. Under compression, however, this quantity can be raised by almost five orders of magnitude, reaching remarkable values of the order of 10 K [84, 85]. But superconductivity is not the only phenomenon emerging at high pressures. Structural phase transitions to less compact structures [86, 87], metal-insulator transitions [88, 89] or anomalous melting curves associated to phonon instabilities [90–92] are other interesting phenomena that arise when pressure is applied to *a priori* simple metals.

Within this context, sodium represents an interesting example. At ambient pressure, this element is one of the closest realizations of the free-electron gas that can be found in solid-state materials. Under compression, however, the simple metal behavior of Na is considerably modified by the non-free-electron-like features of its band structure, which are mainly associated to the increasing electronic hybridization of the chemical bondings and the strong non-local character of the pseudopotential, among other causes [93]. As a consequence, sodium under pressure develops a variety of unexpected processes including phase transitions to extremely complex structures [94], loss of the metallic character [88] or anomalies in the optical response [16, 95]. These remarkable phenomena challenge the classical viewpoint that pressure should make simple metals even simpler.

According to room temperature X-ray diffraction experiments [16, 88, 94–96], sodium undergoes a series of structural phase transformations from 0 to ∼180 GPa before it experiences a metal-insulator transition that suppresses its metallic properties. Over this wide pressure range, sodium first adopts the bcc structure (0 to 65 GPa), followed by the fcc (65 to 105 GPa), the cI16 (105 to 118 GPa), the oP8 (118 to 125 GPa) and the tI19 (125 to ∼180 GPa) configurations [97]. Similar to what happens in lithium and calcium, the metallic properties of sodium at high pressures are strongly modified. In particular, the high and uniform reflectivity (characteristic of good metals) of the bcc, fcc and cI16 phases has been measured to drop drastically in the high pressure phases oP8 and tI19, accompanied by a decrease of the metallic character [16, 95]. The origin of such a behavior is closely related to the emergence of low-energy interband plasmons arising from the increasing localization of the valence electrons [98], as it is the case of Li and Ca [92, 99].

In this chapter, we will perform an *ab-initio* analysis of the electronic response properties of Na in a pressure domain ranging from 0 to 180 GPa, covering all the metallic phases of sodium. With this aim, we have considered the linear response theory within time-dependent DFT (TDDFT), introduced in Sec. 3.1. This formalism goes beyond the first-order time-dependent perturbation theory applied in Sec. 2.2 since TDDFT is a self-consistent approach that is able to describe the rearrangement of the electrons under the influence of an external perturbation. However, the aimed higher accuracy is also computationally more demanding, as the contribution of several bands above the Fermi level must be taken into account in order to yield converged results. Additionally, the Fermi surface associated to the different metallic phases of Na requires a fine sampling of the reciprocal space in order to fully capture the excited properties of the system. Therefore, 'brute-force' calculations are very time demanding, and some scheme for reducing the computational cost is advisable.

To overcome the computational bottleneck, in Sec. 3.2 we will consider MLWFs as the basis for expanding the electron response function. In this formalism, the basis has a trivial dependence on the momentum of the external perturbation, $\mathbf{q}$. Therefore, the evolution of the response function as a function of $\mathbf{q}$ can be efficiently computed, since the MLWFs basis is calculated just once. Additionally, this approach has the advantage that the response function, as well as other $\mathbf{k}$-dependent quantities, can be interpolated into a fine $\mathbf{k}$ mesh thanks to the localization properties of the MLWFs. This way, integrations over the 1BZ are rapidly converged, reducing enormously the cost of the calculations.

The method will be applied to analyze the response properties of Na in Sec. 3.3. In Sec. 3.3.2, we will cover the 0-105 GPa range studying simple bcc and fcc phases, while in Sec. 3.3.3 we will analyze the 105-180 GPa range, where sodium adopts more complex structures. Summary and conclusions will be presented in Sec. 3.4.

3.1 Linear response within TDDFT

In this section we will review the linear response theory within TDDFT [100, 101]. In particular, we will pay special attention to the formalism for analyzing collective electronic charge excitations, commonly known as plasmons.

We begin analyzing the electronic response to an external time-dependent perturbation characterized by a frequency ω and momentum $\mathbf{q}$. To this end, it is useful to consider the retarded (non-interacting) KS response function, which in terms of the ground-state KS orbitals is defined as [102]

$$\chi^{\mathrm{KS}}_{\mathbf{q}}(\mathbf{r},\mathbf{r}',\omega) = \sum_{n_1,n_2} \sum_{\mathbf{k}}^{\mathrm{1BZ}} \frac{f_{n_1\mathbf{k}} - f_{n_2\mathbf{k}+\mathbf{q}}}{\omega + \epsilon_{n_1}(\mathbf{k}) - \epsilon_{n_2}(\mathbf{k}+\mathbf{q}) + i\delta} \times \phi^*_{n_1\mathbf{k}}(\mathbf{r})\phi_{n_2\mathbf{k}+\mathbf{q}}(\mathbf{r})\phi^*_{n_2\mathbf{k}+\mathbf{q}}(\mathbf{r}')\phi_{n_1\mathbf{k}}(\mathbf{r}'), \quad (3.1)$$

where δ is an infinitesimal positive parameter ensuring causality. In general terms, the above quantity measures the variation induced by the external perturbation on the electron density of the non-interacting system. In particular, it contains information about the electronic excitations between KS orbitals differing in energy ω and in momentum $\mathbf{q}$.

The KS response function of Eq. 3.1 does not describe the response of the real interacting system, which should also take into account the rearrangement of the electron density as a consequence of the external perturbation, i.e. it must be a self-consistent response function. This more complex quantity is related to $\chi^{\mathrm{KS}}_{\mathbf{q}}$ by a Dyson integral equation [103],

$$\chi_{\mathbf{q}}(\mathbf{r},\mathbf{r}',\omega) = \chi^{\mathrm{KS}}_{\mathbf{q}}(\mathbf{r},\mathbf{r}',\omega) + \frac{1}{V}\int d\mathbf{r}_1 \frac{1}{\Omega}\int d\mathbf{r}_2 \times \chi^{\mathrm{KS}}_{\mathbf{q}}(\mathbf{r},\mathbf{r}_1,\omega) K_{\mathbf{q}}(\mathbf{r}_1,\mathbf{r}_2,\omega)\chi_{\mathbf{q}}(\mathbf{r}_2,\mathbf{r}',\omega). \quad (3.2)$$

In the equation above, the kernel $K_{\mathbf{q}}(\mathbf{r},\mathbf{r}',\omega)$ takes into account electron-electron effective interactions,

$$K_{\mathbf{q}}(\mathbf{r},\mathbf{r}',\omega) = \frac{1}{|\mathbf{r}-\mathbf{r}'|} + f^{\mathrm{xc}}_{\mathbf{q}}(\mathbf{r},\mathbf{r}',\omega). \quad (3.3)$$

The first term in Eq. (3.3) is the bare Coulomb interaction associated to the electronic charge, while $f^{\mathrm{xc}}_{\mathbf{q}}(\mathbf{r},\mathbf{r}',\omega)$ contains the exchange and correlation effects. In the present work, we go a step beyond the random phase approximation (RPA) [104], $f^{\mathrm{xc}}_{\mathbf{q}}(\mathbf{r},\mathbf{r}',\omega) = 0$, and use the LDA parametrization for the exchange-correlation kernel [19, 105],

$$f^{\mathrm{xc}}_{\mathbf{q}}(\mathbf{r},\mathbf{r}',\omega) = \delta(\mathbf{r}-\mathbf{r}')\left[\frac{\mathrm{d}^2(n\epsilon^{hom}_{xc}(n))}{\mathrm{d}n^2}\right]_{n(\mathbf{r})}, \quad (3.4)$$

with $\epsilon_{xc}^{hom}(n)$ the energy density of the homogeneous electron gas. Here, we follow the parametrization given by Perdew and Zunger in [106] for this quantity.

The interacting response function defined in Eq. (3.2) is a central quantity in the linear response theory, providing a direct link to experimentally measurable properties. For instance, it is directly connected to the dielectric function, $\epsilon_{\mathbf{q}}(\mathbf{r}, \mathbf{r}', \omega)$, which contains diverse information about the response properties of materials, such as the screening of electrons or collective excitations. The inverse of the dielectric function is related to the response function as

$$\epsilon_{\mathbf{q}}^{-1}(\mathbf{r}, \mathbf{r}', \omega) = \delta(\mathbf{r} - \mathbf{r}')\delta(\omega) + \int \mathrm{d}\mathbf{r}'' K_{\mathbf{q}}(\mathbf{r}'', \mathbf{r}', \omega)\chi_{\mathbf{q}}(\mathbf{r}'', \mathbf{r}', \omega). \tag{3.5}$$

It is useful to project the above quantity into the $\mathbf{K} = \mathbf{0}$ plane wave component,

$$\hat{\boldsymbol{\epsilon}}_{\mathbf{q}}^{-1}(\omega)_{\mathbf{00}} = \left\langle \mathbf{0} \,\middle|\, \epsilon_{\mathbf{q}}^{-1}(\mathbf{r}, \mathbf{r}', \omega) \,\middle|\, \mathbf{0} \right\rangle \tag{3.6}$$

In the current description, the peaks of the imaginary part of the above function, $\mathrm{Im}\, \hat{\boldsymbol{\epsilon}}_{\mathbf{q}}^{-1}(\omega)_{\mathbf{00}}$, serve to identify the collective electronic charge excitations, i.e. the plasmons. These are a type of quasiparticles resulting from the quantization of the electron plasma oscillations [104]. The analysis of plasmons is a relevant issue when characterizing the response properties of a material, specially in the case of metals, as they play a central role in determining the optical properties.

Another relevant quantity is the so-called dynamical structure factor, which is related to the inverse dielectric function by the fluctuation-dissipation theorem [102, 103, 107],

$$S(\mathbf{q}, \omega) = -\frac{|\mathbf{q}|^2}{4\pi^2}\,\mathrm{Im}\, \hat{\boldsymbol{\epsilon}}_{\mathbf{q}}^{-1}(\omega)_{\mathbf{00}}. \tag{3.7}$$

In practice, the above quantity can be accurately measured by inelastic neutron or X-ray scattering experiments [22, 108], providing valuable information about the plasmon dispersion.

3.2 MLWFs as basis set for the KS response function

Having introduced the basics of TDDFT, in this section we will construct an appropriate basis set for calculating $\chi_{\mathbf{q}}^{\mathrm{KS}}(\mathbf{r}, \mathbf{r}', \omega)$ in terms of the MLWFs following the approach by Rousseau, Eiguren and Bergara [109]. We begin by considering the relationship between the KS states and MLWFs of Eq. (1.24),

$$w_{n\mathbf{R}}(\mathbf{r}) = \frac{1}{N}\sum_{\mathbf{k}} e^{-i\mathbf{k}\mathbf{R}} \sum_{m=1}^{M} U_{mn}(\mathbf{k})\phi_{m\mathbf{k}}(\mathbf{r}). \tag{3.8}$$

With the aid of the above expression, the products between KS states entering Eq. 3.1 can be expressed as

$$\phi^*_{n_1\mathbf{k}}(\mathbf{r})\phi_{n_2\mathbf{k}+\mathbf{q}}(\mathbf{r}) = \sum_{m_1,m_2}\sum_{\mathbf{R_1},\mathbf{R_2}} e^{i\mathbf{q}\cdot\mathbf{R_2}} e^{i\mathbf{k}\cdot(\mathbf{R_2}-\mathbf{R_1})} \\ \times U_{n_1m_1}(\mathbf{k}) w^*_{m_1\mathbf{R}_1}(\mathbf{r}) w_{m_2\mathbf{R}_2}(\mathbf{r}) U^\dagger_{m_2n_2}(\mathbf{k}+\mathbf{q}). \quad (3.9)$$

Then, by defining the following bare basis functions

$$B_{I,\mathbf{q}}(\mathbf{r}) = V\sum_{\mathbf{R}'} e^{i\mathbf{q}\cdot(\mathbf{R}'-\mathbf{r})} w^*_{m_1\mathbf{R}'-\mathbf{R}}(\mathbf{r}) w_{m_2\mathbf{R}'}(\mathbf{r}), \quad (3.10)$$

with $I \equiv \{m_1, m_2, \mathbf{R}\}$, the non-interacting response function of Eq. 3.1 can be cast into the following form,

$$\chi^{\mathrm{KS}}_{\mathbf{q}}(\mathbf{r},\mathbf{r}',\omega) = \sum_{IJ}\Big[B_{I,\mathbf{q}}(\mathbf{r})\Big]\boldsymbol{\chi}^{\mathrm{KS}}_{IJ}(\mathbf{q},\omega)\Big[B_{J,\mathbf{q}}(\mathbf{r})\Big]^*, \quad (3.11)$$

with $J \equiv \{m_3, m_4, \mathbf{R}'\}$. We notice that the bare basis of Eq. (3.10) has a trivial dependence on the external momentum $\mathbf{q}$, as it only enters in the exponential factor. Thus, once the product $w^*_{m_1\mathbf{R}'-\mathbf{R}}(\mathbf{r})w_{m_2\mathbf{R}'}(\mathbf{r})$ is calculated and stored, the bare basis for different momenta is straightforwardly obtained. This allows to efficiently map the evolution of the response function as a function of $\mathbf{q}$, which is of critical importance when analyzing the dispersion of plasmons.

The coefficients $\boldsymbol{\chi}^{\mathrm{KS}}_{IJ}(\mathbf{q},\omega)$ entering Eq. (3.11) do not explicitly depend on the MLWFs, but only on the unitary matrices,

$$\boldsymbol{\chi}^{\mathrm{KS}}_{IJ}(\mathbf{q},\omega) = \frac{1}{V}\sum_{\mathbf{k}}^{\mathrm{1BZ}} e^{i\mathbf{k}\cdot(\mathbf{R}-\mathbf{R}')}\sum_{n_1,n_2}\frac{f_{n_1\mathbf{k}} - f_{n_2\mathbf{k}+\mathbf{q}}}{\omega + \epsilon_{n_1}(\mathbf{k}) - \epsilon_{n_2}(\mathbf{k}+\mathbf{q}) + i\delta} \\ \times U_{n_1m_1}(\mathbf{k}) U^\dagger_{m_2n_2}(\mathbf{k}+\mathbf{q}) U^\dagger_{m_3n_1}(\mathbf{k}) U_{n_2m_4}(\mathbf{k}+\mathbf{q}). \quad (3.12)$$

In practice, we have collected all the $\mathbf{k}$-dependent quantities into the above coefficients, being the bare basis functions $B_{I,\mathbf{q}}(\mathbf{r})$ $\mathbf{k}$-independent. Noteworthy, all the ingredients in Eq. (3.12) can be calculated on a fine $\mathbf{k}$ mesh using the Wannier interpolation scheme, allowing a very fine sampling of $\boldsymbol{\chi}^{\mathrm{KS}}_{IJ}(\mathbf{q},\omega)$.

We notice that in contrast to the bare basis, the dependence of $\boldsymbol{\chi}^{\mathrm{KS}}_{IJ}(\mathbf{q},\omega)$ on the external momentum is not trivial as it involves terms like $U_{mn}(\mathbf{k}+\mathbf{q})$, $\epsilon_n(\mathbf{k}+\mathbf{q})$ and $f_{n\mathbf{k}+\mathbf{q}}$. In principle, these terms should be calculated *ab-initio* for each different $\mathbf{q}$. However, if the point $\mathbf{k}+\mathbf{q}$ lies inside the interpolated grid, then the $\mathbf{q}$-dependent quantities of Eq. (3.12) are directly available. In practice, Wannier interpolation allows to consider such fine $\mathbf{k}$ meshes so that choosing $\mathbf{q}$ inside the interpolated grid does not represent a limitation.

From the computational point of view, it is of practical interest to express the central equation describing the interacting response function (Eq. 3.2) as a matrix equation. Let us consider the kets $|B_{I,\mathbf{q}}\rangle$ associated to the bare basis functions and represent the KS response function as

$$\hat{\boldsymbol{\chi}}_{\mathbf{q}}^{\mathrm{KS}} = \sum_{IJ} |B_{I,\mathbf{q}}\rangle \, \boldsymbol{\chi}_{IJ}^{\mathrm{KS}}(\mathbf{q},\omega) \, \langle B_{J,\mathbf{q}}| \, . \tag{3.13}$$

In this way, Eq. 3.2 can be written as a matrix equation,

$$\hat{\boldsymbol{\chi}}_{\mathbf{q}} = \left(\hat{\mathbf{1}} - \hat{\boldsymbol{\chi}}_{\mathbf{q}}^{\mathrm{KS}} \cdot \hat{\boldsymbol{K}}_{\mathbf{q}}\right)^{-1} \cdot \hat{\boldsymbol{\chi}}_{\mathbf{q}}^{\mathrm{KS}}. \tag{3.14}$$

Obviously, this matrix equation must be truncated into a finite size problem in order to be solved numerically. Given that the bare basis functions are not linearly independent [109], it is suboptimal to compute all the coefficients $\boldsymbol{\chi}_{IJ}^{\mathrm{KS}}(\mathbf{q},\omega)$ independently. Instead, it is convenient to establish a minimal basis set that describes the essential physics of the problem.

Crystal local field effects

We have already mentioned that plasmons are described as peaks in $\mathrm{Im}\,\hat{\boldsymbol{\chi}}_{\mathbf{q}}(\omega)_{\mathbf{00}}$ (Eq. (3.6)). Therefore, it is sensible to explicitly include the plane wave $|\mathbf{0}\rangle$ into the minimal basis set. In addition, crystal local field effects (CLFE) often play an important role in determining the plasmon dispersion; usually, wave vectors other than $\mathbf{q}$ are needed for describing the spatial variation of external fields inside the solid due to the inhomogeneity of the system [102, 104]. Generally, the use of a finite number of $\mathbf{K}$ vectors properly describes the CLFE [103, 110]. Therefore, we include plane waves into the minimal basis set; as in the case of the plane wave expansion of the KS orbitals (Eq. 1.12), the number of $\mathbf{K}$ vectors to include is a parameter to be converged.

Therefore, the minimal basis is conformed by the functions

$$|g_i\rangle \in \{|\mathbf{0}\rangle \, , \{|\mathbf{K}\rangle\}\} \, . \tag{3.15}$$

In this way, the self-consistent Eq. (3.14) regarding the interacting response function can be solved by projecting the relevant functions into the minimal basis set,

$$[\hat{\boldsymbol{\chi}}_{\mathbf{q}}]_{ij} \simeq \sum_{l} \left[\left(\hat{\mathbf{1}} - \hat{\boldsymbol{\chi}}_{\mathbf{q}}^{\mathrm{KS}} \cdot \hat{\boldsymbol{K}}_{\mathbf{q}}\right)^{-1}\right]_{il} [\hat{\boldsymbol{\chi}}_{\mathbf{q}}^{\mathrm{KS}}]_{lj} \, , \tag{3.16}$$

where $[\ ]_{ij} \equiv \langle g_i | \quad | g_j \rangle$.

Similarly, we can write the projection of the inverse dielectric function (Eq. (3.5)) too,

$$\left[\hat{\boldsymbol{\epsilon}}_{\mathbf{q}}^{-1}\right]_{ij} \simeq \delta_{ij} + \sum_{l} \left[\hat{\boldsymbol{K}}_{\mathbf{q}}\right]_{il} \cdot [\hat{\boldsymbol{\chi}}_{\mathbf{q}}]_{lj} \, . \tag{3.17}$$

Since we explicitly included the $|\mathbf{0}\rangle$ function into the minimal basis set, the $\left[\hat{\boldsymbol{\epsilon}}_{\mathbf{q}}^{-1}\right]_{00}$ term is precisely the one carrying information about plasmon modes.

3.3 Electron response properties of sodium under pressure

In this section we present the calculated electronic properties of sodium using the formalism introduced in Sec. 3.1. Our calculations cover a pressure range from 0 to 180 GPa. We divide the analysis in two different parts, namely the 0-105 GPa range, analyzed in Sec. 3.3.2, and the 105-180 GPa range, analyzed in Sec. 3.3.3. In the first one, sodium adopts the bcc and fcc structures, which are considerably simpler than the ones arising above 105 GPa. All these structures are illustrated in Fig. 3.1. The computational details are described below.

3.3.1 Computational details

The DFT calculations for the ground state eigenvalues and eigenfunctions have been performed using the QUANTUM-ESPRESSO package [23], with plane waves as the basis set for the expansion of the KS orbitals. The cutoff energy used to determine the size of the plane wave basis has been 120 Ry. The exchange-correlation energy has been approximated within the LDA parametrization [19, 106] and the 1BZ has been sampled on a 12 × 12 × 12 **k**-point mesh [111].

The electron-ion interaction has been modeled considering a non-relativistic PP for Na generated with the OPIUM code [112] and tested with all-electron calculations performed with the ELK code [113]. We have included $2s^2 2p^6 3s^1$ states in the valence in order to properly describe short range effects induced by pressure.

The postprocessing step for obtaining the MLWFs has been done using the WANNIER90 code [30]. We have taken into account all bands up to 35 eV above the Fermi level. Once the MLWFs have been constructed, the necessary ingredients for calculating the interacting response function, namely eigenvalues, occupation factors and rotation unitary matrices, have been interpolated on a fine 80 × 80 × 80 **k**-point mesh. Regarding CLFE, the use of 3 reciprocal lattice shells has yielded converged results in all the phases.

The effects of compression have been simulated by reducing the lattice parameter. For the bcc and fcc configurations, we have used the experimental parameters extracted from the equation of state of sodium at the corresponding pressures [114]. For the cI16 and oP8 phases, we have considered the lattice parameters reported in high pressure experiments [16, 94]. For the tI19 phase, sodium adopts an incommensurate host-guest configu-

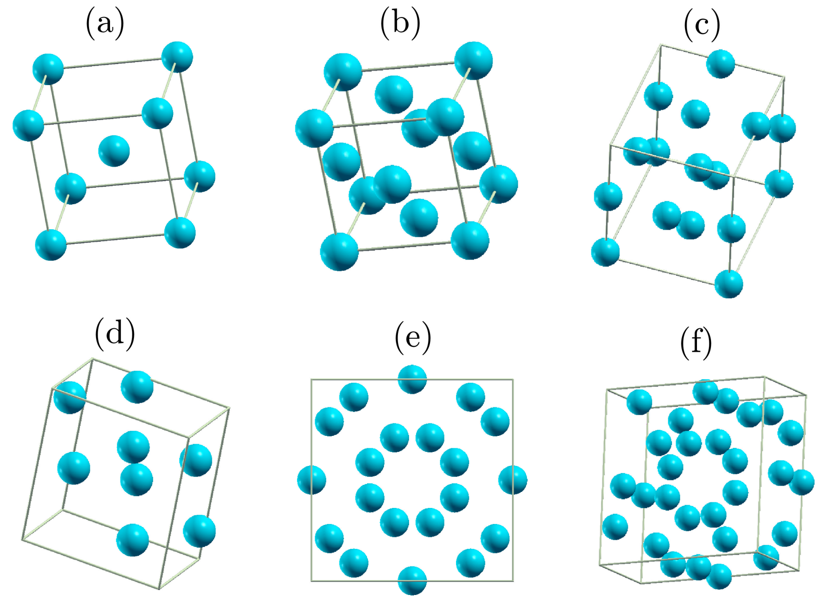

Figure 3.1: Sketch of the different structures that sodium adopts from 0 to 180 GPa. (a) and (b) illustrate the simplest structures: bcc (0-65 GPa) and fcc (65-105 GPa). (c) shows the cI16 structure (105-118 GPa), which contains 8 atoms per unit cell in a bcc-like structure [94]. (d) illustrates the distribution of Na atoms in the oP8 (118-125 GPa) configuration, which is a simple primitive orthorhombic structure with 8 atoms per unit cell [94]. (e) and (f) correspond to two different viewpoints of the tI20 conmensurate structure considered to simulate the inconmensurate tI19 structure (125-180 GPa).

ration with 16 host atoms distributed in a tetragonal bcc structure [94]. We have modeled this incommensurate phase by the closely related commensurate tI20 structure, containing 20 atoms per unit cell [16]. Due to the wide stability pressure range of tI19 (125 to 180 GPa), we have analyzed the evolution of its electronic properties at different pressures. As for this structure there is no accessible experimental lattice parameters at the present time, we have used the theoretically calculated ones: $a = 6.59, 6.46, 6.34$ a.u. and $c = 3.65, 3.54, 3.42$ a.u. for 125, 150 and 180 GPa, respectively.

3.3.2 Simple phases of sodium

The bcc phase (0-65 GPa)

We begin by analyzing the electron-hole and collective excitations of bcc Na at ambient pressure. In Fig 3.2a, we show the calculated dynamical structure factor, while the electron-hole excitation spectrum is analyzed in Fig. 3.2b through the calculated KS response function, $\mathrm{Im}\,\hat{\chi}^{\mathrm{KS}}_{\mathbf{q}}(\omega)_{\mathbf{00}}$.

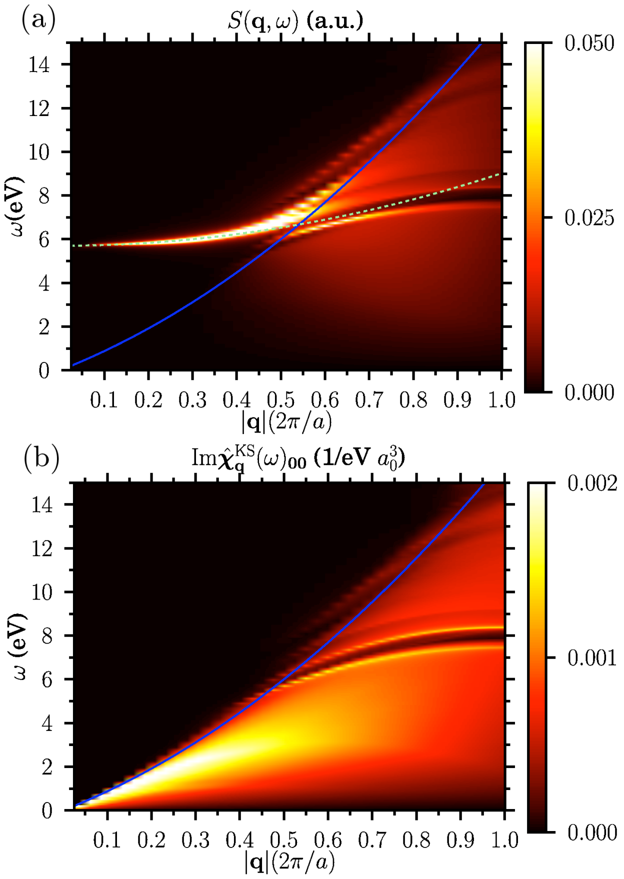

Figure 3.2: (a) and (b) show the dynamical structure factor and imaginary part of the KS response function of bcc Na at ambient pressure along the ΓP direction, respectively. In (a), dashed (green) line depicts the plasmon dispersion in the RPA free-electron model (Eq. (3.18)), while in (b) it represents the boundary $q^2/2m_{\mathrm{eff}}+qv_F$ of the intraband electron-hole excitations.

Fig 3.2 shows a quantitative agreement between our calculations and the predictions of the free-electron model. For low values of the momentum, the calculated plasmon dispersion (Fig. 3.2a) follows the classical expression in the RPA [104],

$$E_p(q) = \omega_p + \frac{\alpha_{RPA}}{m_{\mathrm{eff}}}q^2, \tag{3.18}$$

with m_{eff} the effective electron mass, $\alpha_{RPA} = \frac{3}{5}\frac{E_F}{m_{\mathrm{eff}}\omega_p}$ a dimensionless dispersion constant, E_F the Fermi energy and $\omega_p = \sqrt{4\pi n}/m_{\mathrm{eff}}$ the intraband plasmon energy in the free-electron model, where n is the valence electron density. At ambient pressure, the free-electron-like intraband plasmon for $\mathbf{q} \to 0$ is expected to be located around $E_p(q \to 0) = \omega_p \simeq 5.8$ eV, in good agreement with the calculated value ~ 5.7 eV.

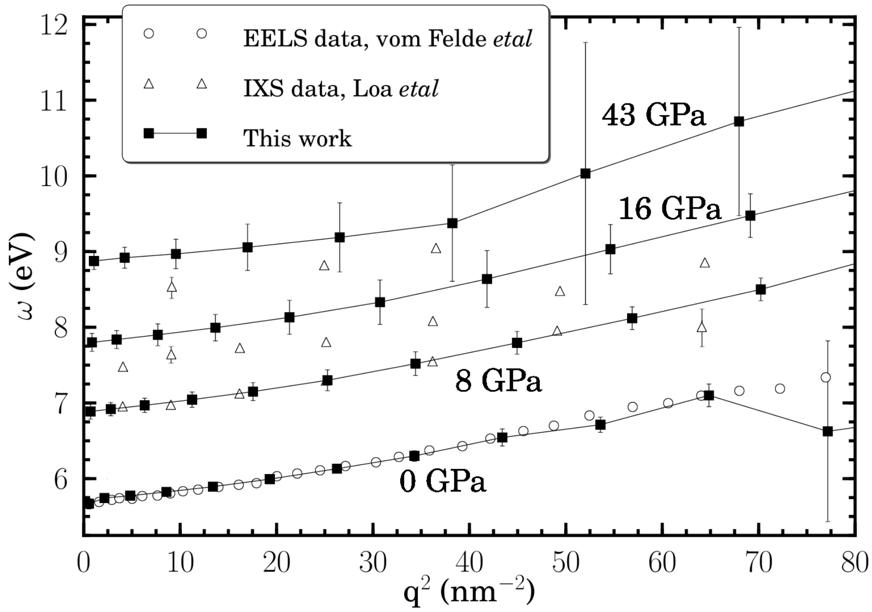

Figure 3.3: Plasmon dispersion $E_p(q^2)$ of bcc Na for various pressures. Squares represent our *ab-initio* results, with the calculated plasmon linewidth indicated by the markers. The full lines are simple guides to the eye. Circles denote experimental EELS data taken from Ref. [115], while triangles denote experimental IXS data taken from Ref. [16]. In the latter case, we have included the available experimental linewidth. The experimental energy resolutions are 0.16 eV and 0.6 eV for the EELS [115] and the IXS [16] data, respectively.

Fig. 3.2a displays a smooth parabolic dispersion of the plasmon until it decays into the electron-hole continuum at around 6.3 eV. This is clear from Fig. 3.2b, where the border of electron-hole continuum can be inferred from the free-electron model prediction,

$$\omega \leq \frac{q^2}{2m_{\text{eff}}} + qv_F, \tag{3.19}$$

with $v_F = \sqrt{2E_F/m_{\text{eff}}}$ the Fermi velocity. The above dispersion is shown as a solid blue line in Fig. 3.2b, matching very well the calculated border.

In Fig. 3.3 we present the calculated plasmon dispersion at 0, 8, 16 and 43 GPa extracted from the position of the peaks in the energy-loss function at these pressures. We have plotted the plasmon energies as a function of q^2, since we expect the parabolic dependence of Eq. (3.18). Overall, we find that the dispersion is indeed very close to parabolic at all pressures, though the results at 0 and 43 GPa show a slight slope change at $q^2 \sim 40$ nm^{-2} and

$q^2 \sim 65$ nm^{-2}, respectively. As revealed by the calculated linewidth, which increases up to ∼2 eV at the mentioned momenta, the change of slope is due to the damping of the plasmon, which ceases to be a well defined collective excitation at those points.

For comparison, in Fig. 3.3 we have included experimental data obtained by electron energy-loss spectroscopy (EELS) at ambient pressure [116] and inelastic X-ray scattering (IXS) at higher pressures [16]. As it can be appreciated, our results are essentially in agreement with the experimental data. In the case of 0 and 8 GPa, both the calculated energies and dispersion slopes are practically identical to the experimental ones. At 16 and 43 GPa, the calculated peaks are slightly overestimated by $\sim$ 0.3 eV with respect to the measured ones. This is barely larger than the standard error of the IXS experimental data, which had an energy resolution of 0.6 eV [117]. Furthermore, the agreement between the calculated and experimental slopes at these two pressures indicates the adequacy of our calculations for describing the collective electronic properties of the system at different pressures.

The fcc phase (65-105 GPa)

At 65 GPa sodium undergoes a phase transformation from the bcc to the fcc structure. Unlike the rest of alkali metals, the Fermi surface of Na remains spherical up to $\sim$ 105 GPa [118] and, furthermore, the plasmon dispersion retains the features of the free-electron model [119]. Therefore, fcc Na can be regarded as a simple metal. Our *ab-initio* calculations verify both the spherical shape of the Fermi surface and the free-electron-like plasmon dispersion of Na over all the stability pressure range of the fcc phase. However, we also characterize an anisotropic interband plasmon along the ΓL direction that indicates a significant departure of fcc Na from the simple metal behavior.

In Fig. 3.4a we display the calculated dynamical structure factor of fcc Na at 75 GPa along ΓL, showing an intraband plasmon with parabolic dispersion that emerges at around 9.5 eV, in reasonable agreement with IXS experiments measuring $\omega_p \simeq 9.25$ eV [119]. Remarkably, we also find a (weaker) second plasmon branch which does not follow at all the free-electron-like parabolic dispersion (see inside the dashed circle). The analysis of the energy-loss function (Fig. 3.4b) shows that this second branch emerges and disappears at finite values of the momentum, $|\mathbf{q}| \sim 0.2 \cdot 2\pi/a$ and $|\mathbf{q}| \sim 0.5 \cdot 2\pi/a$, respectively. Furthermore, the vanishingly small plasmon linewidth of Fig. 3.4b indicates that the associated collective excitation is practically undamped.

In order to identify the nature of this plasmon, we have performed an analysis of the energy-loss function along different directions, and we have not found any similar peak of $-\operatorname{Im}\hat{\epsilon}_{\mathbf{q}}^{-1}(\omega)_{\mathbf{00}}$ in any other direction. This fact reveals a strong anisotropy of the system. In accordance, the electronic

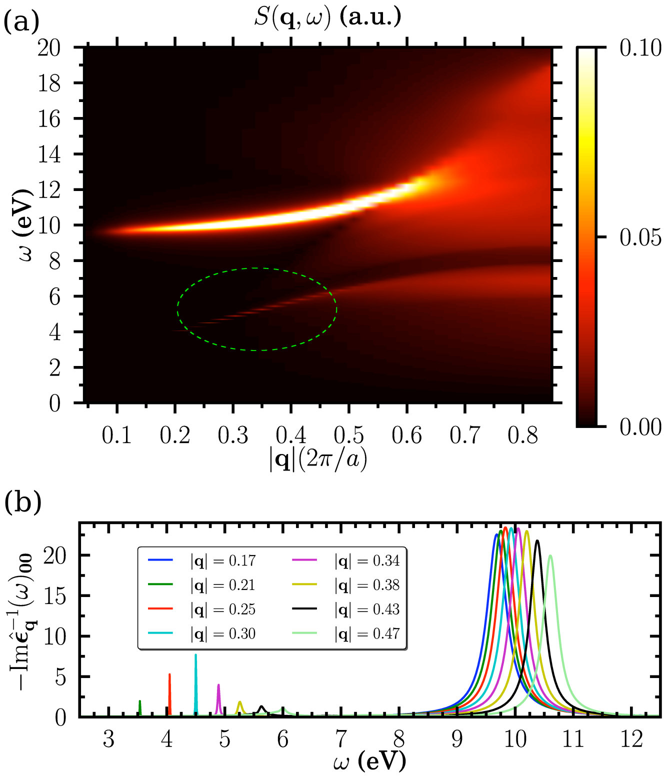

Figure 3.4: (a) and (b) show the dynamical structure factor and energy-loss function of fcc Na at 75 GPa along the ΓL direction, respectively. In (a), the dashed (green) circle encloses the area where the anisotropic interband plasmon emerges. In (b), the values of the momentum considered are depicted in the inset (units of $2\pi/a$).

band structure of fcc Na (Fig 3.5) displays important anisotropic features. Specifically, the free-electron-like band presents a gap at significantly different energies for different directions; the gap opens at $\sim$ 1 eV along ΓL, while for the rest of directions it starts around 3 to 4 eV. As shown in the next paragraph, the band structure has a direct impact on the electron-hole excitations and is the origin of the anisotropic plasmon that we have found.

In Fig. 3.6 we display the real and imaginary parts of the dielectric function along ΓL and ΓX for various values of the momentum. Whereas for a given direction the calculations for different $\mathbf{q}$'s share similar features, the results along ΓL and ΓX exhibit important differences. We first analyze the results along ΓL (Fig. 3.6a). Focusing on $|\mathbf{q}| = 0.25 \cdot 2\pi/a$, we observe a decrease of $\mathrm{Im}\,\hat{\epsilon}_{\mathbf{q}}(\omega)_{\mathbf{00}}$ until it completely vanishes at $\sim$3.0 eV. This value coincides approximately with the energy at which intraband excitation along ΓL vanish due the opening of a band gap (see inset of Fig. 3.5). The absence of electron-hole excitations remains up to $\sim$3.6 eV, where interband

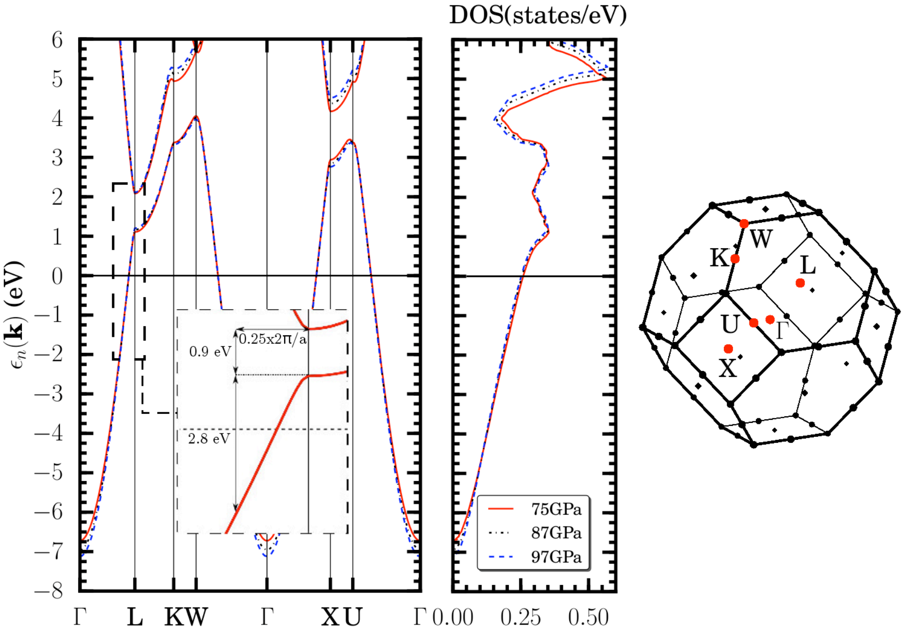

Figure 3.5: (Left panel) Electronic band structure of fcc Na at 75, 87 and 97 GPa. The inset shows the details of the band gap around high symmetry point L at 75 GPa. The Fermi level is indicated by the horizontal solid (black) line. (Central panel) Total DOS (states/eV). (Right panel) 1BZ of the fcc structure.

transitions begin; again, this energy coincides with the end of the band gap along ΓL. The strength of interband excitations is evidenced by the prominence of the peak at ∼3.7 eV in $\mathrm{Im}\,\hat{\boldsymbol{\epsilon}}_{\mathbf{q}}(\omega)_{\mathbf{00}}$. Due to Kramers-Kronig relations [103], the peak in the imaginary part drives the real part to the positive side, passing through zero at ∼3.6 eV. This has a direct impact in the energy loss function through the relation

$$\mathrm{Im}\,\hat{\boldsymbol{\epsilon}}_{\mathbf{q}}^{-1}(\omega)_{\mathbf{00}} = -\frac{\mathrm{Im}\,\hat{\boldsymbol{\epsilon}}_{\mathbf{q}}(\omega)_{\mathbf{00}}}{(\mathrm{Re}\,\hat{\boldsymbol{\epsilon}}_{\mathbf{q}}(\omega)_{\mathbf{00}})^2 + (\mathrm{Im}\,\hat{\boldsymbol{\epsilon}}_{\mathbf{q}}(\omega)_{\mathbf{00}})^2}. \tag{3.20}$$

As appreciated in Fig. 3.6a, the vanishing value of $\mathrm{Re}\,\hat{\boldsymbol{\epsilon}}_{\mathbf{q}}(\omega)_{\mathbf{00}}$ and $\mathrm{Im}\,\hat{\boldsymbol{\epsilon}}_{\mathbf{q}}(\omega)_{\mathbf{00}}$ at ∼3.6 eV induces a peak in $\mathrm{Im}\,\hat{\boldsymbol{\epsilon}}_{\mathbf{q}}^{-1}(\omega)_{\mathbf{00}}$ at this energy, giving rise to the so-called interband plasmon.

The above described situation remains very similar for $|\mathbf{q}|$ =0.30, 0.34 and 0.38·$2\pi/a$, the only relevant difference being an overall shift of all the features to higher energies, including the plasmon peak (see Fig. 3.6a). For even higher momenta (results not shown), we find that the intraband and interband excitations overlap so that $\mathrm{Im}\,\hat{\boldsymbol{\epsilon}}_{\mathbf{q}}(\omega)_{\mathbf{00}}$ does not completely vanish in the intermediate energy region, leading to a significant broadening and weakening of the plasmon peak. Finally, for $|\mathbf{q}| < 0.2 \cdot 2\pi/a$ the interband

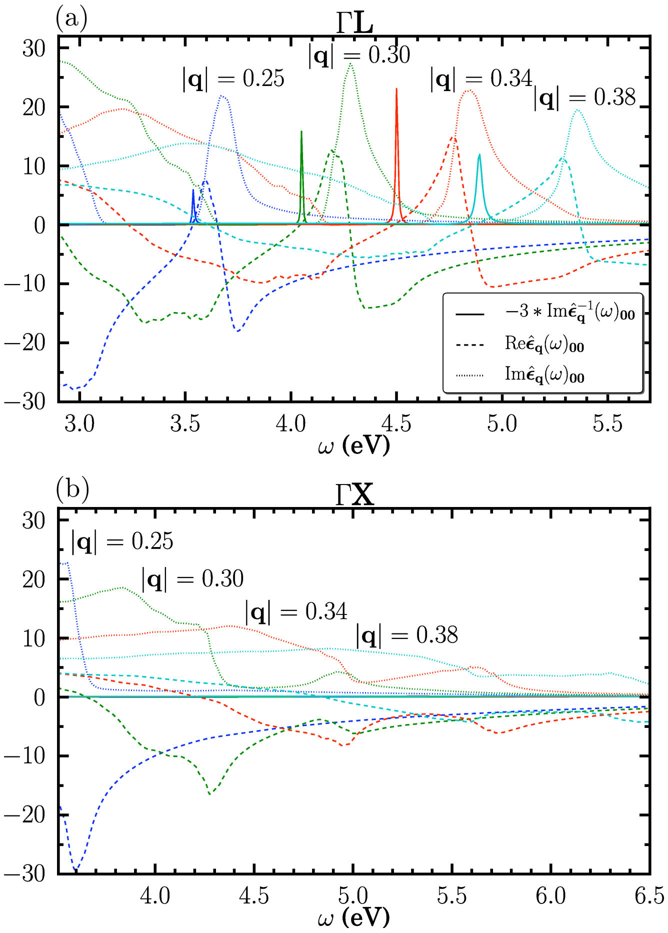

Figure 3.6: Real (dashed lines), imaginary (dotted lines) and inverse imaginary part (solid lines) of the dielectric function of fcc Na at 75 GPa along ΓL (a) and ΓX (b). Note the different scale for $-\operatorname{Im}\hat{\boldsymbol{\epsilon}}_{\mathbf{q}}^{-1}(\omega)_{\mathbf{00}}$. Shown results are for $|\mathbf{q}| = 0.25$, 0.30, 0.34 and 0.38 (units of $2\pi/a$).

transitions are not sufficiently strong for driving $\operatorname{Re}\hat{\boldsymbol{\epsilon}}_{\mathbf{q}}(\omega)_{\mathbf{00}}$ to the positive part and, therefore, we do not find any plasmon peak in the energy-loss function.

The calculated results along ΓX, illustrated in Fig. 3.6b, display two major differences with respect to the ones in Fig. 3.6a. First, the intraband excitations end at significantly higher energies than in Fig. 3.6a due to the absence of band gaps in the band structure up to ∼3 eV from the Fermi energy (see Fig. 3.5). As a consequence, the intraband and interband excitations overlap even for $|\mathbf{q}| = 0.25 \cdot 2\pi/a$, preventing $\operatorname{Im}\hat{\boldsymbol{\epsilon}}_{\mathbf{q}}(\omega)_{\mathbf{00}}$ from vanishing. The second major difference resides in the strength of the interband excitations, which is much weaker along the ΓX direction and is reflected by the relative decrease of the interband peak of $\operatorname{Im}\hat{\boldsymbol{\epsilon}}_{\mathbf{q}}(\omega)_{\mathbf{00}}$ as

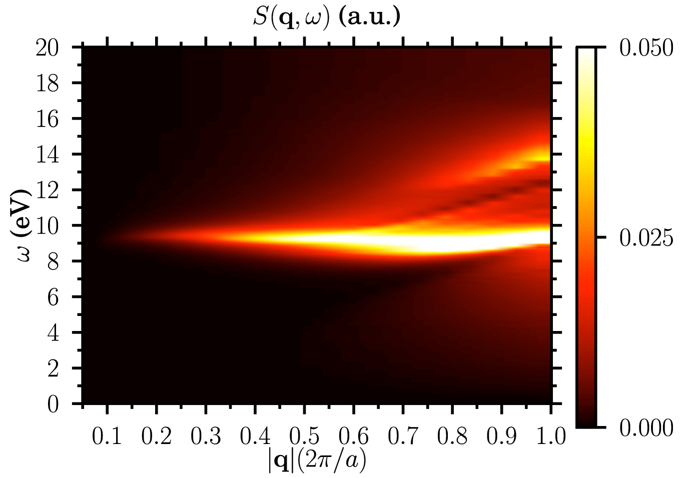

Figure 3.7: Dynamical structure factor of cI16 Na along ΓP at 105 GPa.

compared to that along ΓL. As a consequence, Kramers-Kronig relations do not drive $\mathrm{Re}\,\hat{\boldsymbol{\epsilon}}_{\mathbf{q}}(\omega)_{\mathbf{00}}$ to the positive part in the 3-7 eV energy range. Thus, unlike along ΓL, we do not find any interband plasmon along this or any other high symmetry directions.

We have performed the same analysis at 87 GPa and 97 GPa, verifying that the anisotropic plasmon along ΓL persists at these pressures as well. This is consistent with the associated band structures (see Fig. 3.5), which share very similar features as pressure increases in the fcc structure, including the band gap along ΓL at ~1 eV above the Fermi level. Therefore, our calculations suggests that besides the free-electron-like plasmon at ~ 10 eV, fcc Na should present an additional interband plasmon at ~3.5-5.5 eV all over its stability pressure range.

3.3.3 Complex phases of sodium

As characterized by several high pressure experiments [88, 94, 96], sodium adopts considerably more complex structures than the previous bcc and fcc phases above 105 GPa. Additionally, it exhibits clear fingerprints of pressure-induced complexity in this regime. As an example, the reflectivity of Na has been measured to drastically drop at low frequencies [16], indicating a clear departure from the expected free-electron-like behavior. The connection between the reflectivity and the dielectric function of a material is given by

$$R(\omega) = \frac{(1 - n(\omega))^2 + \kappa^2(\omega)}{(1 + n(\omega))^2 + \kappa^2(\omega)}, \tag{3.21}$$

with $n(\omega) = \mathrm{Re}\sqrt{\hat{\boldsymbol{\epsilon}}_{\mathbf{q}}(\omega)_{\mathbf{00}}}$ and $\kappa(\omega) = \mathrm{Im}\sqrt{\hat{\boldsymbol{\epsilon}}_{\mathbf{q}}(\omega)_{\mathbf{00}}}$. In this section, we will analyze the evolution of this quantity as a function of pressure, allowing to

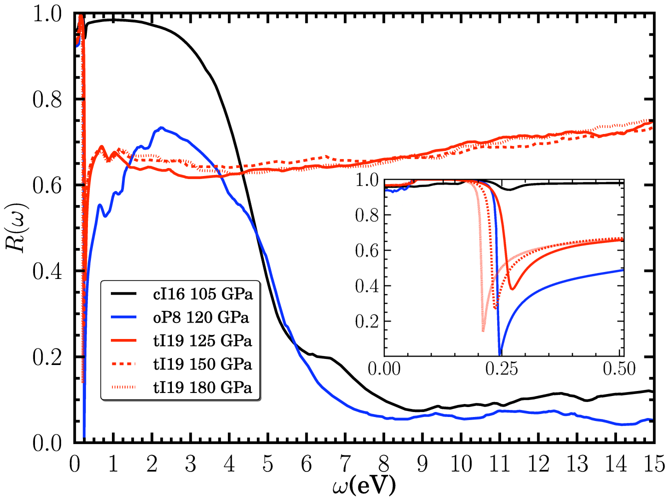

Figure 3.8: The reflectivity spectrum of sodium in the phases cI16 (105 GPa), oP8 (120 GPa) and tI19 (125, 150 and 180 GPa). The inset addresses the 0-0.5 eV range.

confirm and extend the experimental measurements.

The cI16 phase (105-118 GPa)

From 105 to 118 GPa, sodium adopts the cI16 structure. Interestingly, we have not found any anisotropic interband plasmon in this pressure range. This is exemplified in Fig. 3.7, where the calculated dynamical structure factor along the ΓP direction shows a single intraband plasmon at around 9.7 eV, which is $\sim 15\%$ lower than the one predicted by the free-electron model. Furthermore, our calculations indicate that the evolution of the plasmon with respect to the momentum is not parabolic; in fact, Fig. 3.7 describes an almost momentum-independent plasmon dispersion all along ΓP. Therefore, pressure significantly modifies the free-electron nature of sodium in the cI16 phase.

In Fig. 3.8 we show the calculated reflectivity (Eq. (3.21)) for cI16 Na. Our results indicate an almost complete light reflection from 0 to 3 eV. This property is in reasonable agreement with recent experiments [16] measuring a constant reflectivity $R(\omega) \simeq 0.85$ over the same frequency range. At 3 eV, the reflectivity starts a smooth decrease that ends at around 10 eV, where $R(\omega)$ is practically suppressed as a consequence of the intraband plasmon.

The oP8 phase (118-125 GPa)

Beyond 118 GPa, after a phase transformation favoring the oP8 structure [94], sodium exhibits an anomalous behavior associated to its optical

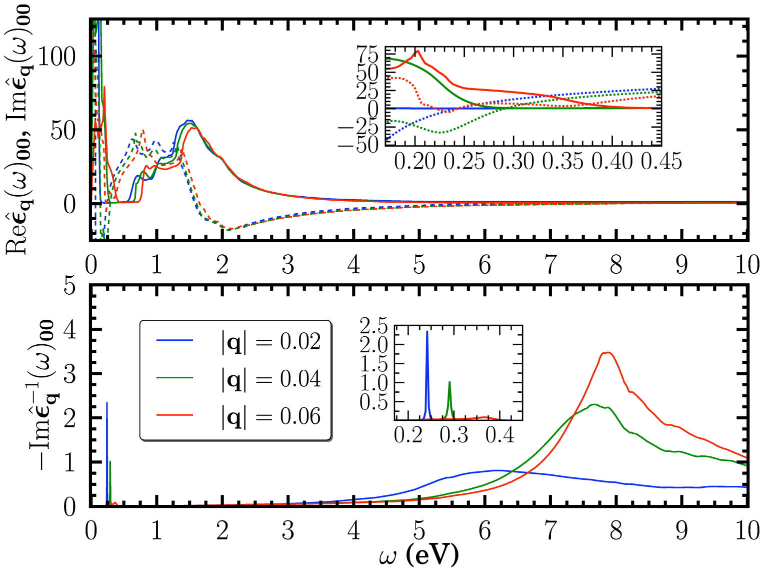

Figure 3.9: Dielectric function of oP8 Na at 120 GPa. Top panel: $\mathrm{Im}\,\hat{\epsilon}_{\mathbf{q}}(\omega)_{\mathbf{00}}$ and $\mathrm{Re}\,\hat{\epsilon}_{\mathbf{q}}(\omega)_{\mathbf{00}}$ are depicted by solid and dashed lines, respectively. Bottom panel: $-\mathrm{Im}\,\hat{\epsilon}^{-1}_{\mathbf{q}}(\omega)_{\mathbf{00}}$. In both panels, results are shown for $|\mathbf{q}|$ =0.02, 0.04 and $0.06 \cdot 2\pi/a$. Both insets illustrate the 0-0.5 eV range.

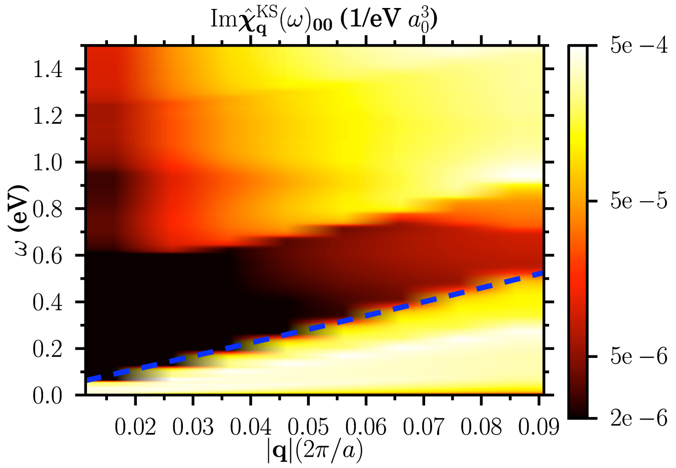

Figure 3.10: Imaginary part of the KS response function of oP8 Na at 120 GPa. The dashed (blue) line indicates the boundary of the intraband excitations. Note the logarithmic scale of $\mathrm{Im}\,\hat{\chi}_{\mathbf{q}}(\omega)_{\mathbf{00}}$ (right).

response. This fact is clearly exemplified by Fig. 3.8, where the calculated reflectivity (Eq. (3.21)) of oP8 Na shows a sudden dip at around 0.25 eV, vanishing almost completely. This behavior is in agreement with recent X-ray diffraction experiments showing a drop of the reflectivity to 0.05 at

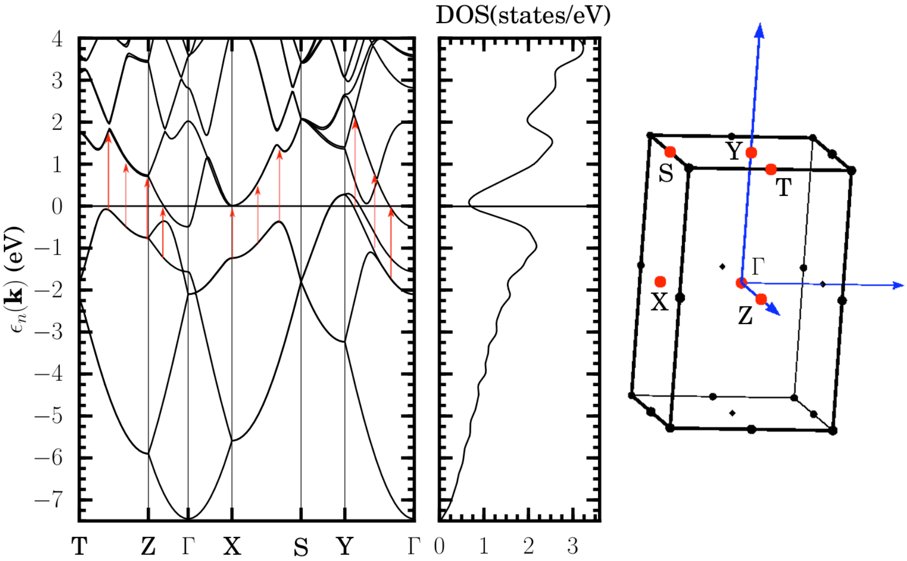

Figure 3.11: (Left panel) Electronic band structure of oP8 Na at 120 GPa. Red arrows depict the interband transitions responsible for the emergence of the low-energy plasmon. The Fermi level is indicated by the horizontal solid (black) line. (Central panel) Total DOS (states/eV). (Right panel) 1BZ of the oP8 structure.

practically the same energy [16]. At higher energies, the reflectivity of oP8 Na increases, but around 2 eV it starts a smooth decrease until $\sim$ 7 eV, where it becomes almost zero (see Fig. 3.8).

In Fig. 3.9 we analyze the various components of the dielectric function of oP8 Na. This figure reveals that the anomalous behavior of $R(\omega)$ in the optical range originates from a low-energy plasmon emerging at around 0.25 eV. This plasmon shares common features with the one theoretically predicted in calcium under pressure [99], which also induces a dip in the calculated reflectivity. It is essentially undamped since both $\mathrm{Im}\,\hat{\boldsymbol{\epsilon}}_{\mathbf{q}}(\omega)_{\mathbf{00}}$ and $\mathrm{Re}\,\hat{\boldsymbol{\epsilon}}_{\mathbf{q}}(\omega)_{\mathbf{00}}$ become almost zero at $\omega \simeq 0.25$ eV, making the plasmon linewidth vanishingly small at this energy. For increasing values of the momentum, the linewidth of the low-energy plasmon starts broadening until $|\mathbf{q}| = 0.06 \cdot 2\pi/a$, where the peak in the energy-loss function is practically suppressed. At higher energies, our calculations evidence the existence of an intraband plasmon at around 6−8 eV that coincides with the final loss of reflectivity depicted in Fig. 3.8.

The interband nature of this low-energy plasmon is analyzed in Fig. 3.10, where we present the KS response function of oP8 Na. For $|\mathbf{q}| < 0.04$ $2\pi/a$, our calculations evidence a gap ($\sim$0-0.6 eV) between the intraband and interband excitations, where $\mathrm{Im}\,\hat{\boldsymbol{\chi}}^{\mathrm{KS}}_{\mathbf{q}}(\omega)_{\mathbf{00}}$ completely vanishes. As appreciated in the top panel of Fig. 3.9, this gap is also present in $\mathrm{Im}\,\hat{\boldsymbol{\epsilon}}_{\mathbf{q}}(\omega)_{\mathbf{00}}$.

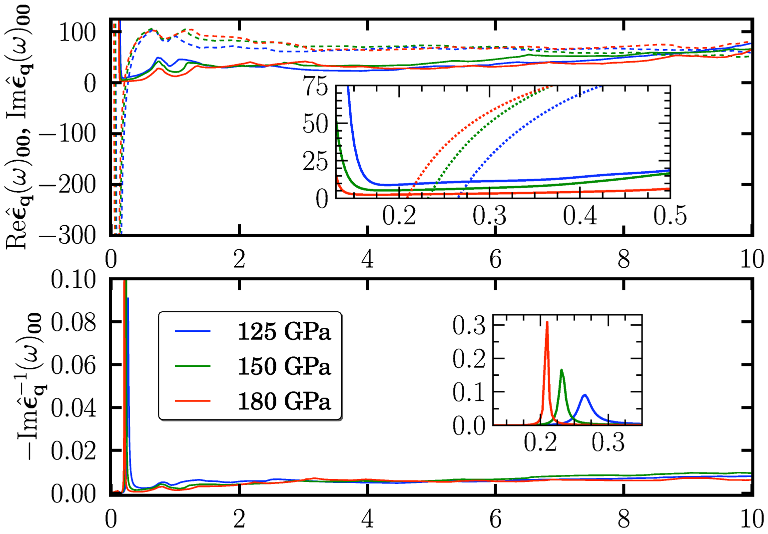

Figure 3.12: Dielectric function of tI19 Na at 125, 150 and 180 GPa for $|\mathbf{q}| = 0.03 \cdot 2\pi/a$ along ΓX. Top panel: $\mathrm{Im}\,\hat{\boldsymbol{\epsilon}}_{\mathbf{q}}(\omega)_{\mathbf{00}}$ and $\mathrm{Re}\,\hat{\boldsymbol{\epsilon}}_{\mathbf{q}}(\omega)_{\mathbf{00}}$ are depicted by solid and dashed lines, respectively. Bottom panel: $-\mathrm{Im}\,\hat{\boldsymbol{\epsilon}}_{\mathbf{q}}^{-1}(\omega)_{\mathbf{00}}$.

Driven by the Kramers-Kronig relations, the gap and the subsequent interband excitations contributing to the imaginary part ($\omega > 0.6$ eV) force the real part of the dielectric function to become positive at $\omega \simeq 0.25$ eV, giving rise to the low-energy interband plasmon at that energy.

The relevant interband excitations contributing to $\mathrm{Im}\,\hat{\boldsymbol{\epsilon}}_{\mathbf{q}}(\omega)_{\mathbf{00}}$ in the $\mathbf{q}\to 0$ limit are characterized in the band structure of oP8 Na depicted in Fig. 3.11, alongside with the calculated DOS, which reproduces the weakening of the metallic character at the Fermi level reported in other works [16, 95]. As indicated by the red arrows in Fig. 3.11, there exist quasi-parallel occupied-unoccupied bands separated by 1-2 eV along various directions in reciprocal space: ZT, ΓZ, XS and ΓY, among others. The energy difference between these bands coincides with the interband excitations contributing to $\mathrm{Im}\,\hat{\boldsymbol{\epsilon}}_{\mathbf{q}}(\omega)_{\mathbf{00}}$ for $\omega \gtrsim 1$ eV (see top panel of Fig. 3.9), and are therefore directly responsible for the emergence of the low-energy plasmon.

The tI19 phase (125-180 GPa)

At 125 GPa sodium adopts the tI19 structure [94]. As in the oP8 phase, we have also characterized a very low-energy plasmon, shown in Fig. 3.12, that induces a sudden dip on the optical reflectivity at around 0.25 eV (see Fig. 3.8), in qualitative agreement with X-ray reflectivity measurements [16]. We find two major differences between the reflectivity spectrum of the oP8 and tI19 phases. First, the minimum of $R(\omega)$ ranges from ~ 0.4 to ~ 0.2 throughout the stability pressure range of the tI19 phase, whereas in

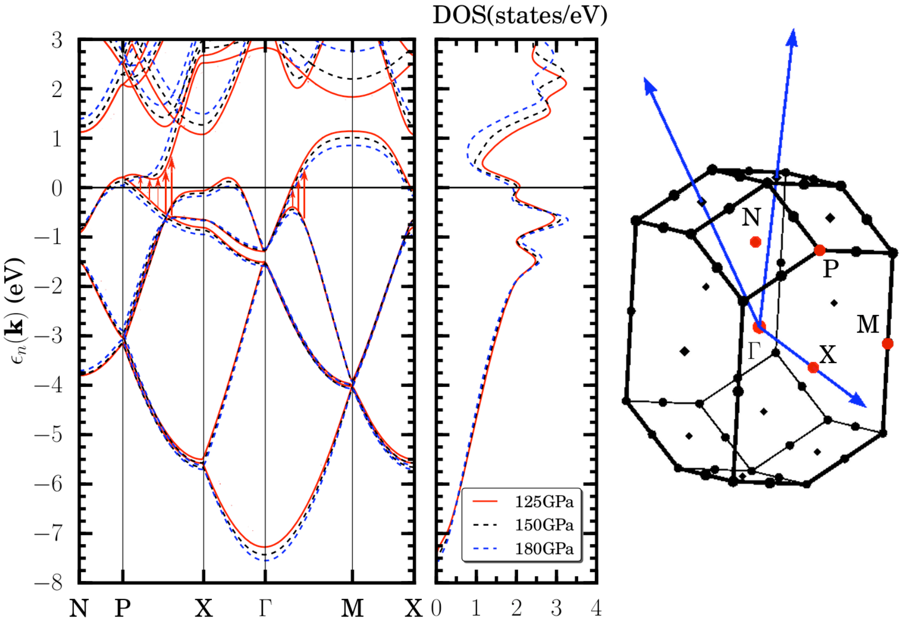

Figure 3.13: (Left panel) Electronic band structure of tI19 Na at 125, 150 and 180 GPa. Red arrows depict the interband transitions responsible for the emergence of the low-energy plasmon. The Fermi level is indicated by the horizontal solid (black) line. (Central panel) Total DOS (states/eV). (Right panel) 1BZ of the oP8 structure.

the oP8 phase $R(\omega) \simeq 0$ at the dip. Second, unlike in the case of oP8 Na, the reflectivity of tI19 Na is almost totally recovered in the infrared regime, i.e. $R(\omega) \geq 0.6$ for $\omega > 0.75$ eV. These experimentally supported features [16] indicate that tI19 Na shows better metallic properties than oP8 Na, excluding a possible metal-insulator transition between the two phases.

We have performed an analysis of the dielectric response function throughout the stability pressure range of tI19 Na from 125 to 180 GPa, as shown in Fig. 3.12. We find that the low-energy plasmon persists over all the studied domain. Moreover, our calculations indicate that the plasmon becomes undamped as pressure is increased, i.e. its linewidth decreases with increasing pressure (see Fig. 3.12b). As shown in the inset of Fig. 3.12a, $\mathrm{Im}\,\hat{\boldsymbol{\epsilon}}_{\mathbf{q}}(\omega)_{\mathbf{00}}$ does not completely vanish in the $\sim 0.2 - 0.5$ eV range, where $\mathrm{Re}\,\hat{\boldsymbol{\epsilon}}_{\mathbf{q}}(\omega)_{\mathbf{00}}$ becomes vanishingly small. As a consequence, the resulting plasmon acquires a finite linewidth; since $\mathrm{Im}\,\hat{\boldsymbol{\epsilon}}_{\mathbf{q}}(\omega)_{\mathbf{00}}$ decreases (approaches zero) with increasing pressure, so does the plasmon linewidth.

In Fig. 3.13 we show the calculated electronic band structure and DOS of tI19 Na at 125, 150 and 180 GPa. The electronic excitations contributing to $\mathrm{Im}\,\hat{\boldsymbol{\epsilon}}_{\mathbf{q}}(\omega)_{\mathbf{00}}$ in the $0.5 - 1.0$ eV range (see Fig. 3.12a) are characterized by the red arrows, evidencing, as in the oP8 phase, the interband nature of the low-energy plasmon. Another important detail revealed by Fig. 3.13 is that tI19 Na develops two hole-pockets, one around high symmetry point P and the other one halfway between Γ and X. Low-energy intraband excitations to these hole-pockets are the reason why $\mathrm{Im}\,\hat{\epsilon}_{\mathbf{q}}(\omega)_{\mathbf{00}}$ does not completely vanish in the $\sim 0.2-0.4$ eV energy range. Furthermore, Fig. 3.13 indicates that the area of the hole-pockets diminishes with increasing pressure, yielding weaker low-energy excitations at high pressures. We conclude that the behavior of the low-energy plasmon revealed by Fig. 3.12b is directly associated to the evolution of the hole-pockets under pressure.

3.4 Conclusions

In this chapter, we have presented *ab-initio* calculations describing the electronic dielectric response of sodium in its five known metallic phases from 0 to 180 GPa. We have applied a formalism based on Wannier interpolation that provides an accurate sampling of reciprocal space and allows the resolution of sharp features associated to the dielectric function. In this way, we have found a low-energy plasmon in the high pressure phases oP8 and tI19 that explains the anomalous behavior of the optical reflectivity recently measured in X-ray experiments [16], which is also reproduced by our calculations. The combined analysis of the KS response function and the electronic band structure reveals the interband nature of this low-energy plasmon, which is associated to electron-hole transitions between quasi-parallel bands. Additionally, our calculations have characterized an anisotropic interband plasmon along the stability pressure range of the fcc configuration (65 to 105 GPa), revealing an unexpected departure of fcc Na from the free-electron-like behavior. This plasmon is found exclusively along the ΓL direction due to an anisotropic non-free-electron-like band structure effect. Therefore, the calculations presented in this Chapter provide a clear fingerprint of pressure-induced complexity in sodium.

Chapter 4

Tight binding models for optical lattices

The experimental realization of Bose-Einstein condensates through laser cooling and evaporative cooling of atoms has become a routine procedure since it was first achieved in 1995 by three different groups [120–122]. Nowadays, the study of cold atoms trapped in 2D periodic optical lattices is a versatile alternative to study electrons in crystal structures [123]. In fact, optical lattices possess a number of advantages over crystals, such as a great control over the relevant parameters that determine the properties of the periodic structure (shape and strength of the light potential), the absence of lattice defects or other type of effects that destroy the quantum coherence.

As a consequence, optical lattices are widely used to emulate diverse properties of electrons in solids. As an example, Mott insulating phases have been achieved through the accurate control of atomic interactions [124, 125], providing a better understanding of the strongly correlated regime of materials. Similarly, the relativistic properties of electrons in systems such as graphene can also be accessed and simulated by trapping atoms in honeycomb optical lattices [126–132]. The versatility for studying diverse phenomena makes the field of cold atoms of growing interest in the condensed matter community.

In general, potentials describing optical lattices can be expressed in simple analytic forms as the combination of a number of sinusoidal functions [127, 131]. However, from the theoretical point of view it is often more convenient to describe the system by means of a tight binding (TB) approach on a discrete lattice. In fact, the potential intensity can be tuned to sufficiently high values in order to localize the atoms in the lowest vibrational states of the potential wells, i.e. the potential minima. This localization justifies a description of optical lattices in terms of tunneling coefficients related to the hopping between neighboring sites [123].

A crucial ingredient for the connection between the continuous and discrete versions of the system Hamiltonian is the existence of a basis of functions localized around the potential minima. This is important not only conceptually - in order to justify the TB expansion - but also from the practical point of view, as a precise knowledge of the basis functions is needed to connect the TB coefficients with the actual experimental parameters [133]. In the simple case of optical lattices with a 2D cubic-like arrangement containing a single well per unit cell, for instance, this basis is provided by the exponentially decaying WFs first discussed by Kohn [123, 134, 135], from which one can derive analytic expressions for the TB coefficients [136]. In general, however, this approach fails when the potential has more than one well per unit cell. For example, in the case of a 2D potential with two degenerate minima in the unit cell, the Kohn-Wannier function cannot be associated to a single lattice site, as it occupies both minima for symmetry reasons [137, 138]. This 2D case was recently analyzed by Lee and coworkers [127], who applied a semiclassical approach to analytically calculate localized WFs and the associated TB coefficients.

In the context of complex optical geometries containing more than one minimum per unit cell, a powerful approach is based on the MLWFs, as they can incorporate the contribution of several bands. In this regard, Modugno and Pettini [133] showed how to construct analytic MLWFs for one-dimensional periodic potentials with a double-well per unit cell. The corresponding TB coefficients allowed to accurately reproduce the exact spectrum, proving the usefulness of the MLWFs as TB basis functions in this context. However, applications of MLWFs to optical lattices are rather scarce, partly because they were originally developed in the context of the electronic structure of solids. Only very recently a number of works [139–141] have analyzed TB models of 2D optical lattices in terms of the MLWFs, with successful results.

In this Chapter, we analyze how to construct TB models for ultracold atoms in a variety of 2D optical lattice structures by means of the MLWFs. In Sec. 4.1 we present the general formalism to calculate the tunneling coefficients of interest via the MLWFs.In Secs. 4.2 and 4.3 we apply the formalism to the honeycomb and strectched-honeycomb optical lattices, respectively. The first one serves as a basic test example, while the second one will allow to consider several optical geometries by varying the optical parameters. In both cases, we provide explicit calculations of the MLWFs and the tunneling coefficients. We also discuss the degree of accuracy of different TB approximations in reproducing the exact Bloch spectrum. These results show that TB models based on MLWFs are successful in reproducing the properties of the experimentally accessible optical lattices in a broad parameter range, using only a relatively small number of tunneling coefficients.

4.1 Tight binding models using MLWFs

When cold atoms are trapped in the potential wells of an optical lattice, their state is usually described by the lowest vibrational level. In such cases, a description of the system in terms of non-interacting particles is adequate. Therefore, we consider the following single particle Hamiltonian,

$$H_0 = -\frac{1}{2}\nabla^2 + V(\mathbf{r}), \tag{4.1}$$

where $V(\mathbf{r})$ represents the one body 2D optical potential induced by the laser beams. For formal derivations, it will be useful to consider the Hamiltonian density associated to Eq. (4.1) in the language of second quantization,

$$\mathcal{H}_0 = \int d\mathbf{r}\ \psi^\dagger(\mathbf{r}) H_0 \psi(\mathbf{r}), \tag{4.2}$$

where $\psi(\mathbf{r})$ denotes the field operator of the cold atoms. The above Hamiltonian density can be conveniently mapped onto a TB model defined on the discrete lattice corresponding to the potential minima of $V(\mathbf{r})$. This is achieved by expanding the field operator in terms of a set of functions $w_{n\mathbf{R}}(\mathbf{r})$ localized at each minimum, as

$$\psi(\mathbf{r}) \equiv \sum_n \sum_{\mathbf{R}} a_{n\mathbf{R}} w_{n\mathbf{R}}(\mathbf{r}). \tag{4.3}$$

In 2D, the cell label contains two components, i.e. $\mathbf{R} = (R_1, R_2)$. In Eq. (4.3), $a^\dagger_{n\mathbf{R}}$ ($a_{n\mathbf{R}}$) represent the creation (destruction) operators of a single particle in the cell $\mathbf{R}$.

As already mentioned in the introduction, we consider MLWFs for composite bands introduced in Sec. 1.2 as the basis functions, $w_{n\mathbf{R}}(\mathbf{r}) = \langle \mathbf{r} \,|\, \mathbf{R}n \rangle$. The optical potentials $V(\mathbf{r})$ that we analyze throughout this work contain two potential minima per unit cell. Thus, we construct a basis of MLWFs by considering the two lowest Bloch bands of the system, which we name A and B. We calculate the mentioned Bloch bands using a modified version of the QUANTUM-ESPRESSO package [23], intended to solve the single particle Schrödinger equation associated to Eq. (4.1). The technical details regarding the procedure are included in Appendix E. As a next step, we compute the MLWFs considering the approach implemented in the WANNIER90 program [30], which follows the steps outlined in Sec. 1.2.

The approach of including two Bloch bands is the so-called minimal approximation, corresponding to the generalization of the usual *single band approximation* for cubic-type lattices [123]. In this approximation, the Hamiltonian density of Eq. (4.2) can be written as

$$\mathcal{H}_0 \simeq \sum_{nn'=A,B} \sum_{\mathbf{R}\mathbf{R}'} a^\dagger_{n\mathbf{R}} a_{n'\mathbf{R}'} \langle \mathbf{R}n | H_0 | \mathbf{R}'n' \rangle \equiv \mathcal{H}_0^{tb}, \tag{4.4}$$

where we have restricted the sum over states to the two lowest states, A and B.

In Eq. (4.4), $\langle \mathbf{R}n|H_0|\mathbf{R}'n'\rangle$ are the tunneling coefficients between neighboring lattice sites, and play a central role in determining the quality and usefulness of the TB approach. In general, it is desirable to achieve a good compromise between accuracy and simplicity if a TB model is to be useful. The accuracy is measured by the ability of the model to reproduce the properties of the optical lattice, such as the band structure, while the simplicity is related to the number of coefficients contained in the model; the fewer coefficients, the simpler is the model.

Due to the maximal localization of the MLWFs, we expect that the expansion of Eq. 4.4 may be truncated including only a few tunneling coefficients around a given site $\mathbf{R}$,

$$T_{nn'}^{\mathbf{R}-\mathbf{R}'} \equiv -\langle \mathbf{R}n|H_0|\mathbf{R}+\mathbf{R}'n'\rangle. \tag{4.5}$$

In other words, we expect the TB models in terms of MLWFs optimize accuracy and simplicity. In the above coefficient, we distinguish the dominant terms in the expansion, i.e. the onsite energies,

$$\epsilon_n^{\mathrm{ons}} \equiv \langle \mathbf{R}n|H_0|\mathbf{R}n\rangle. \tag{4.6}$$

In general, the rest of the tunneling coefficients that should be included into the model depends on the geometry and properties of the system under study. In the examples that we will analyze throughout the next two sections, we will describe the accuracy of different levels of the TB approximation including different number of coefficients.

4.2 The honeycomb potential

As a first example, we consider the 2D graphene-like lattice discussed by Lee and co-workers [127]. This lattice is generated by the interference of three co-planar laser beams whose wavevectors differ by an angle of $2\pi/3$ but have equal frequency, strength and linear polarization (see [142] for a detailed explanation). The 2D potential generated by superimposing these laser beams is

$$V(\mathbf{r}) = sE_R\left(3 + 2\cos\left[(\mathbf{b}_1+\mathbf{b}_2)\cdot\mathbf{r}\right] + 2\sum_{i=1,2}\cos\left(\mathbf{b}_i\cdot\mathbf{r}\right)\right). \tag{4.7}$$

The reciprocal basis vectors are

$$\mathbf{b}_1 = \sqrt{3}k_L\frac{\hat{\mathbf{e}}_x - \sqrt{3}\hat{\mathbf{e}}_y}{2}, \quad \mathbf{b}_2 = \sqrt{3}k_L\frac{\hat{\mathbf{e}}_x + \sqrt{3}\hat{\mathbf{e}}_y}{2}, \tag{4.8}$$

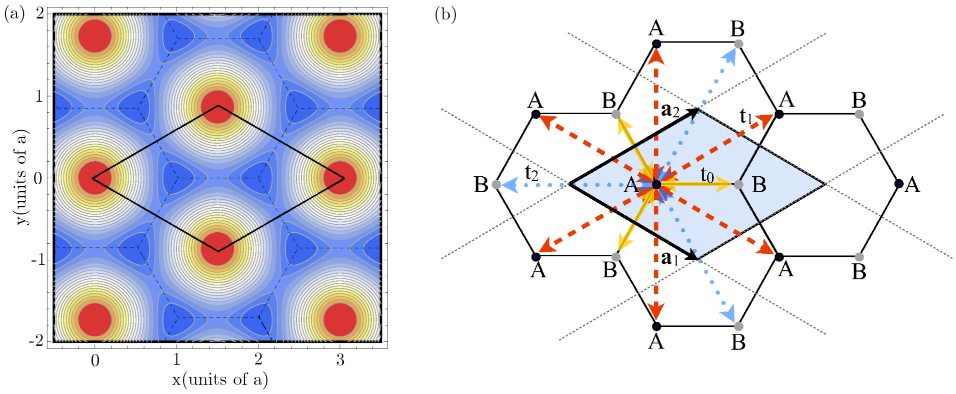

Figure 4.1: (a) Structure of the potential of Eq. (4.7) for $s = 5$. Hot and cold colors denote high and low values, being the potential maximum (red) nine times higher than the minimum (blue). (b) Sketch of the honeycomb lattice structure and the diamond-shaped elementary cell with basis A and B. The length of each side of the hexagon is $a = 4\pi/(3\sqrt{3}k_L)$. Arrows indicate different tunneling coefficients of type A defined in the text.

where k_L is the modulus of the laser wavevectors and s in Eq. (4.7) represents the potential amplitude in units of the recoil energy,

$$E_R = \frac{k_L^2}{2}. \tag{4.9}$$

In Fig. 4.1a we illustrate the real space structure of the potential of (4.7), where the minima of the potential are distributed in a honeycomb structure, similar to the distribution of carbon atoms in a graphene layer. The corresponding real-space Bravais lattice is generated by the two fundamental vectors,

$$\mathbf{a}_1 = \Lambda\frac{\hat{\mathbf{e}}_x - \sqrt{3}\hat{\mathbf{e}}_y}{2}, \quad \mathbf{a}_2 = \Lambda\frac{\hat{\mathbf{e}}_x + \sqrt{3}\hat{\mathbf{e}}_y}{2}, \tag{4.10}$$

with $\Lambda = 4\pi/3k_L$ the common length of the Bravais primitive vectors, being $\Lambda = \sqrt{3}a$, with a the length of each side of the hexagon in the honeycomb lattice.

4.2.1 Band structure and MLWFs

Before constructing the TB model, we first analyze the properties of the two lowest states associated to the honeycomb potential of Eq. (4.7). The calculated *ab-initio* band structure of the two lowest states, $E_{A/B}(\mathbf{k})$, is shown in Fig. 4.2b for various values of the potential amplitude s. These two bands are characterized by so-called Dirac points at $\mathbf{k}_D = \mathrm{K}, \mathrm{K}'$ (note that we have fixed $E_{A/B}(\mathbf{k}_D) = 0$). At these points, the local dispersion of

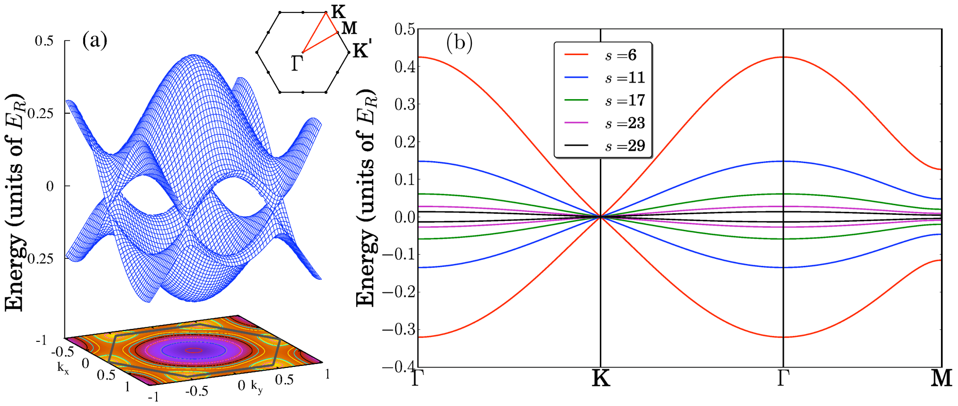

Figure 4.2: (a) 3D band structure of the lowest two bands for $s = 6$. The hexagon represents the SBZ. (b) Plot of the band structure along the path $\Gamma - \mathrm{K} - \Gamma - \mathrm{M}$ for various values of the potential amplitude s.

the band structure is linear, resembling the dispersion of relativistic massless particles. Furthermore, the two bands are degenerate at K and K$'$, a situation known as a semi-metal or a zero-gap semi-conductor state. In Fig. 4.2b, the existence of the Dirac point is not affected since varying s does not change the symmetry of the potential. However, the band dispersion decreases significantly as s is raised, revealing the stronger localization of the associated Bloch orbitals.

Once the band dispersion of the two lowest Bloch bands has been described, we focus now on the associated MLWFs, which have been calculated following the procedure outlined in Sec. 4.1. We have performed calculations for the potential amplitude s ranging from 0 to 30. In all the cases, we have found that the converged MLWFs are real and exponentially localized around one of the potential minima. The typical shape of the calculated MLWFs is shown in Fig. 4.3. The strong localization of $|w_{n\mathbf{0}}(\mathbf{r})|^2$ $(n = A, B)$ around sites A and B, and their exponential decay are clearly visible in panel (a). Panel (c) shows the distribution of $|w_{A\mathbf{0}}(\mathbf{r})|^2$ around the home unit cell $\mathbf{R} = \mathbf{0}$. The figure reveals an appreciable overlap of the MLWF with neighboring B and A sites, indicated respectively by yellow and red arrows in Fig. 4.1. In addition, the MLWFs are characterized by the presence of nodes in passing from site A to B.

4.2.2 Tunneling coefficients

Considering the exponential localization of the MLWFs shown in Fig. 4.3, we expect that a TB description of the system incorporating only a few tunneling coefficients in the expansion of Eq. (4.4) will capture the main properties of the system. Thus, we have included up to third-nearest neighbors in Eq. (4.5), i.e. $\mathbf{R}' \equiv (0, \pm 1; 0, \pm 1)$ in units of the direct lattice defined in Eq. (4.10). Note that the tunneling coefficients depend only on the relative distance owing to the uniformity of the lattice. As we explain below, these coefficients can be divided in three classes, as shown in Fig. 4.1b for the case $n = A$.

(i) Terms corresponding to the overlap between $A(B)$ and the three nearest neighbors of type $B(A)$, yellow arrows in Fig. 4.1. We will use the following notation based on Eq. 4.5,

$$t_0 \quad = \quad T_{AB}^{(0,0)}. \tag{4.11}$$

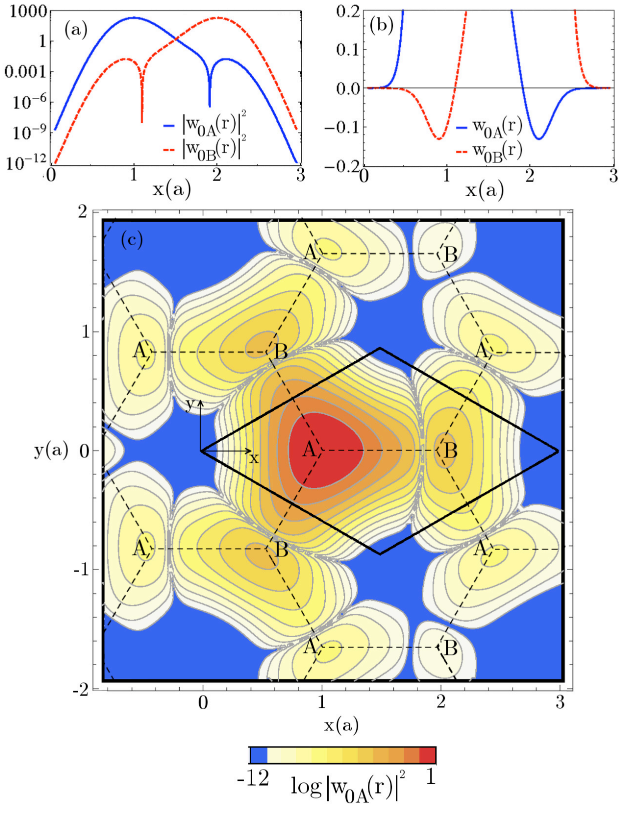

Figure 4.3: Example of the calculated MLWFs for $s = 15$. (a) Profile of $|w_{A\mathbf{0}}(\mathbf{r})|^2$ (solid, blue) and $|w_{B\mathbf{0}}(\mathbf{r})|^2$ (dashed, red) along the line joining the A and B sites ($y = 0$) in the original unit cell. (b) Profile of $w_{A\mathbf{0}}(\mathbf{r})$ and $w_{B\mathbf{0}}(\mathbf{r})$ along the same path as in (a) with a zoom into the small values of the MLWFs. Note that $w_{A\mathbf{0}}(\mathbf{r})$ ($w_{B\mathbf{0}}(\mathbf{r})$) becomes negative in the neighborhood of site B (A). (c) Contour plot of the function $\log |w_{A\mathbf{0}}(\mathbf{r})|^2$. The solid and dashed lines depict the original unit cell and the honeycomb lattice, respectively.

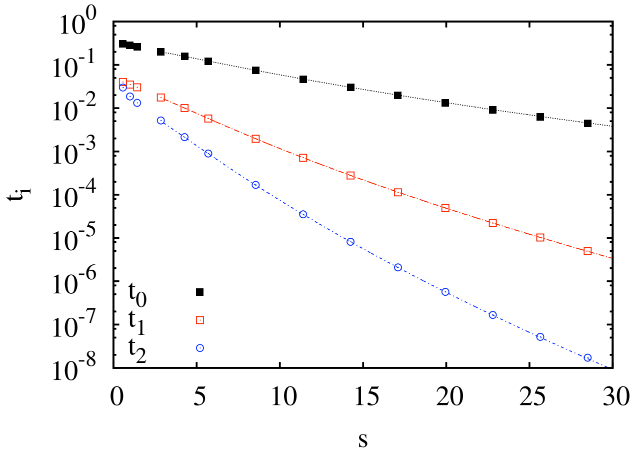

Figure 4.4: Evolution of the various tunneling coefficients as a function of the lattice intensity s. The lines are the result of a fit of the numerical data, and those for t_0 and t_1 coincide with that extracted from a fit of the Bloch spectrum (see text).

Above, (0,0) is the difference between the real-space Wannier indexes of the two sites, i.e. $\mathbf{R} - \mathbf{R}' = (0, 0)$ (see Eq. 4.5).

(ii) Terms corresponding to the overlap between sites of the same type (A or B) within neighboring cells, as indicated by red arrows in Fig. 4.1,

$$t_1 \quad = \quad -T^{(1,0)}_{nn}, \quad n = A, B. \tag{4.12}$$

We notice that the sign in Eq. (4.12) is chosen so that t_1 is positive defined. This sign is a consequence of the MLWFs nodes analyzed in Fig. 4.3b, which make diagonal and off-diagonal terms of opposite sign.

(iii) Terms corresponding to the overlap between $A(B)$ and $B(A)$ at opposite corners of the hexagon, as indicated by blue arrows in Fig. 4.1,

$$t_2 \quad = \quad T^{(1,1)}_{AB}. \tag{4.13}$$

The behavior of the different tunneling coefficients as a function of the lattice intensity s is shown in Fig. 4.4. In order to extract an analytic expression from the numerical values, we have considered a fit of the type $t_i = As^{\alpha}e^{-\beta\sqrt{s}}$ $(i = 0, 1, 2)$, in the range $s > 3$, with A, α, and β as fitting parameters. For t_0 we find

$$t_0 = 1.16 s^{0.95} e^{-1.634\sqrt{s}}. \tag{4.14}$$

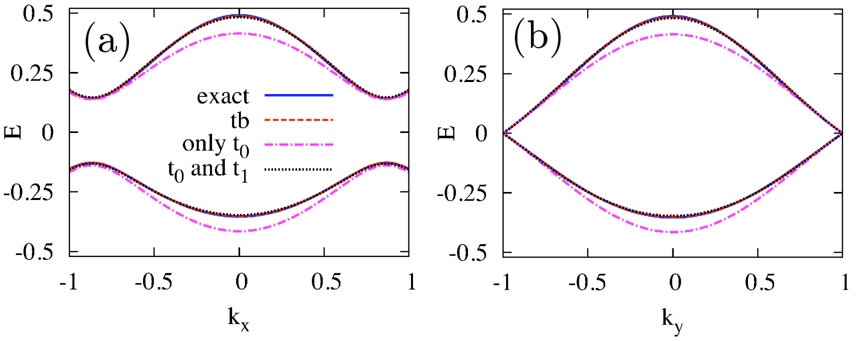

Figure 4.5: (b,c) Band structure for $k_y = 0$ and $k_x = 0$, respectively (blue, solid lines). The latter are compared with the prediction of the full TB model (red dashed line), that with t_0 and t_1 (black dotted line), and with just t_0 (magenta dot-dashed line). Note the asymmetry of the two bands.

For the other two terms we get

$$t_1 = 0.78 s^{1.85} e^{-3.404\sqrt{s}}, \tag{4.15}$$

$$t_2 = 1.81 s^{2.75} e^{-5.196\sqrt{s}}. \tag{4.16}$$

4.2.3 Accuracy of the tight binding model

A convenient way to check the regime of validity of a given TB approximation is to compare its prediction for the energy spectrum with the exact Bloch spectrum. The procedure for deriving the TB spectrum in terms of the tunneling coefficients has been included in Appendix F. Here we show an specific example of the TB spectrum in Figs. 4.5b-c for a particular value of the potential amplitude, $s = 5$. The figure shows that the TB model with just t_0 is not sufficient to reproduce the band structure, and at least the inclusion of the coefficient t_1 is needed. In particular, it is clear that the latter is necessary to account for the band asymmetry.

A further way to test the quality of the TB approximation is to analyze the overall mismatch between the TB and exact bands. Here, we evaluate this mismatch using the following expression,

$$\delta\varepsilon_n \equiv \frac{1}{\Delta E_n}\sqrt{\sum_{\mathbf{k}} [E_n(\mathbf{k}) - \epsilon_n(\mathbf{k})]^2}, \tag{4.17}$$

with ΔE_n the $n-$th bandwidth ($n = 1, 2$), and $E_n(\mathbf{k})$ and $\epsilon_n(\mathbf{k})$ the exact (*ab-initio*) and approximate (TB) eigenvalues, respectively.

The results for the mismatch are shown in Fig. 4.6. This figure shows that the TB model with up to third-nearest neighbors accurately reproduces the band structure for $s \gtrsim 3$, with an error below 1%. In fact, this is a range of the potential intensity where one would expect the MLWFs to localize

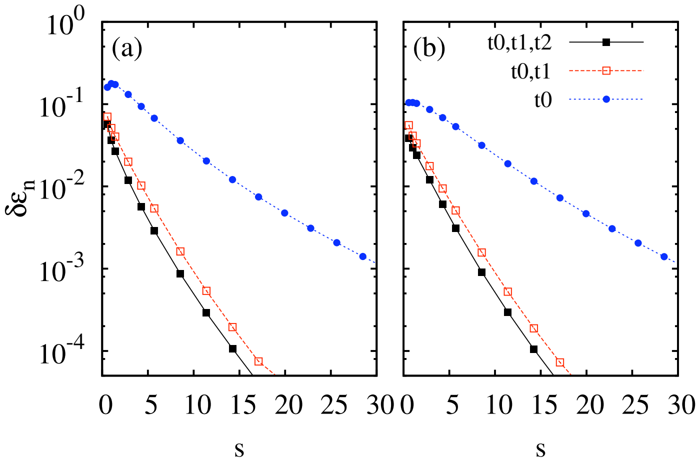

Figure 4.6: Energy mismatch, $\delta\varepsilon_n$, for the first (a) and second (b) band, considering different levels of approximation of the TB model.

strongly around each minimum (that is, a proper TB regime). While the inclusion of t_2 provides only a minor correction, the model with just the nearest neighbor tunneling coefficient, t_0, is clearly less accurate, reaching the level $\delta\varepsilon_n \lesssim 1\%$ only for high values of the potential intensity, $s \gtrsim 15$. This may be particularly relevant for the range of parameters of current experiments since they are performed in a regime of relatively low potential amplitudes ($s \lesssim 5$).

4.2.4 First conclusions

In this section, we have analyzed the 2D honeycomb optical lattice with two minima per unit cell, an example that allows to mimic the physics of graphene as it contains so-called Dirac points. We have shown that MLWFs are a powerful tool for determining the parameters of TB models describing the optical lattice. In particular, the TB model in terms of the three closest nearest neighbor coefficients calculated with the aid of the MLWFs has accurately reproduced the features of the exact system, with an overall error below 1% in the regimes of practical interest.

4.3 Stretched-honeycomb potential

In this section we will analyze the potential reproduced experimentally in Ref. [131] by Tarruel and co-workers,

$$\begin{aligned} V(x,y) = &- V_{\overline{X}} \cos^2(k_L x + \theta/2) - V_X \cos^2(k_L x) \\ &- V_Y \cos^2(k_L y) - 2\alpha\sqrt{V_X V_Y}\cos(k_L x)\cos(k_L y)\cos(\varphi), \end{aligned} \tag{4.18}$$

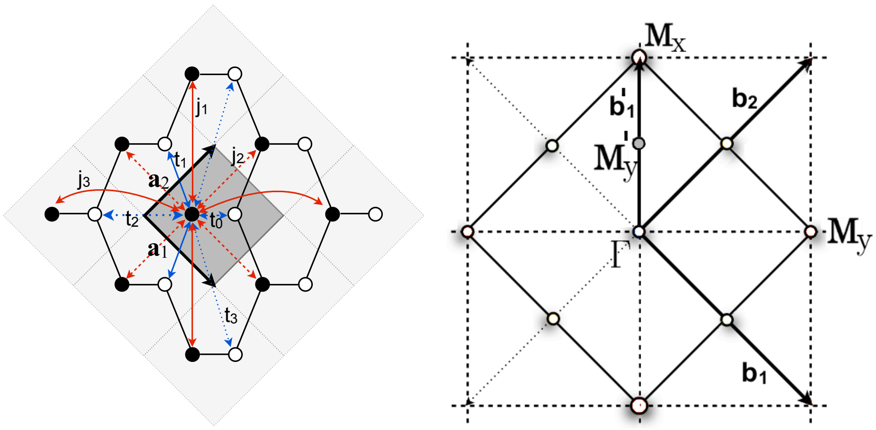

(a) (b)

Figure 4.7: (a) Bravais lattice associated to the potential in Eq. (4.18) for the stretched honeycomb configuration. Black and white circles refers to minima of type A and B, respectively. The elementary cell is highlighted in gray. The various diagonal and off-diagonal tunneling coefficients of our TB expansion are indicated for the site of type A in the central cell. (b) The associated 2D BZ. The high symmetry points of interest are indicated.

where all the parameters can be controlled and tuned in the experiment. In particular, by varying the laser intensities $V_{\overline{X}}$, V_X and V_Y, several structures can be realized by continuous deformations, ranging from chequerboard to triangular, dimmer, honeycomb, and square lattices, including 1D-chains (see Figs. 4.8(a-c) for three examples). Additionally, tuning the angle θ away from π allows to break the degeneracy between the two potential minima contained in the associated unit cell. Thus, the present case, generally referred as the stretched-honeycomb potential, allows for an ample degree of freedom compared to the ideal honeycomb potential analyzed in the previous section. The aim of this section is therefore to test the validity of the MLWFs as a TB basis in a more general case.

The Bravais lattice associated to the potential in Eq. (4.18) is generated by the following basis vectors

$$\mathbf{a}_1 = \frac{\pi}{k_L}(\hat{\mathbf{e}}_x - \hat{\mathbf{e}}_y), \quad \mathbf{a}_2 = \frac{\pi}{k_L}(\hat{\mathbf{e}}_x + \hat{\mathbf{e}}_y). \tag{4.19}$$

The associated real space structure is shown in Fig. 4.7a, which contains two basis points, denoted as A and B.

The corresponding basis vectors in reciprocal space are

$$\mathbf{b}_1 = k_L(\hat{\mathbf{e}}_x - \hat{\mathbf{e}}_y), \quad \mathbf{b}_2 = k_L(\hat{\mathbf{e}}_x + \hat{\mathbf{e}}_y), \tag{4.20}$$

obtained from $\mathbf{a}_i \cdot \mathbf{b}_j = 2\pi\delta_{ij}$. The associated 2D BZ is represented in Fig. 4.7b.

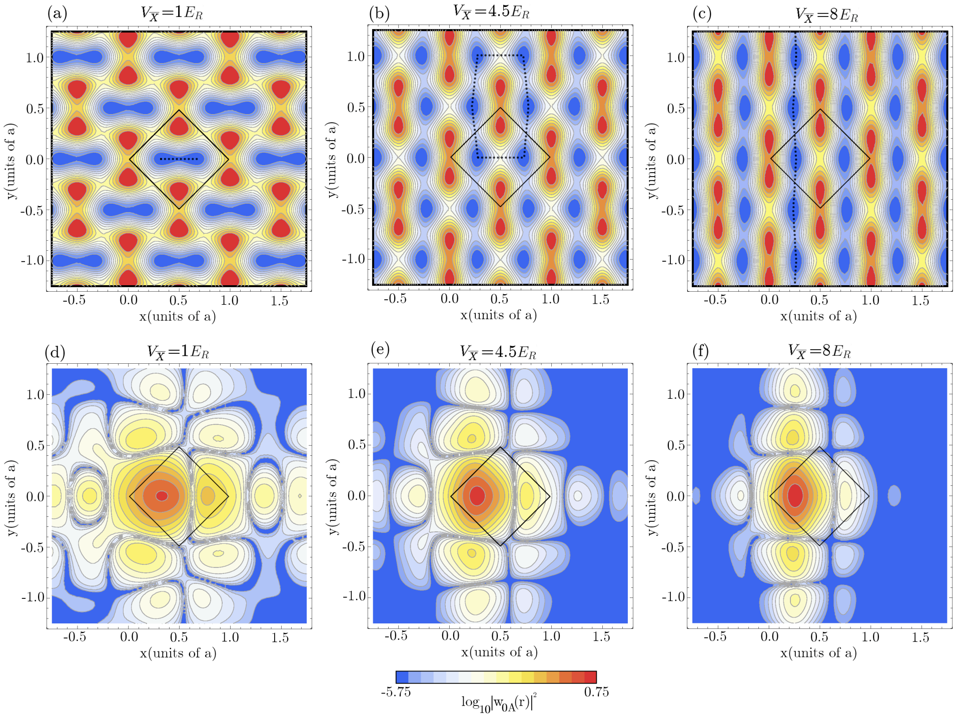

Figure 4.8: (a-c) Examples of the three potential types that can be obtained by varying $V_{\overline{X}}$ from 1 to 8 with fixed $V_X = 0.28$ and $V_Y = 1.8$ in the symmetric case ($\theta = \pi$, $\varphi = 0$). (a) Dimmer, $V_{\overline{X}} = 1$. (b) Stretched-honeycomb, $V_{\overline{X}} = 4.5$. (c) 1D-chain, $V_{\overline{X}} = 8$. Red and blue colors denote high and low values of the potential, respectively. The unit cell is represented by solid black lines. (d-f) Representation of the calculated MLWFs (sublattice A) for the same potential setup as in (a-c) .

To begin our analysis of the potential of Eq. (4.18), we first focus on the non-degenerate (symmetric) case obtained by setting $\theta = \pi$, $\varphi = 0$. This is the most interesting configuration due to the presence of Dirac points, as will be shown in the following section. The effect of parity breaking ($\theta \neq \pi$) generates a gap at the Dirac point, and will be covered in Sec. 4.3.4. In the rest of the section, we will set $k_L = 1$ without loss of generality. This corresponds to measuring lengths in units of $1/k_L$ and energies in units of the recoil energy, E_R (see Eq. (4.9)).

4.3.1 From the dimmer configuration to the 1D-chain regime

As in the reference experiment by Tarruel and co-workers [131], we will restrict our analysis to the structures obtained by varying the potential parameter $V_{\overline{X}}$ from 1 to 8, while we maintain fixed the values $V_X = 0.28$ and $V_Y = 1.8$, with symmetric configuration ($\theta = \pi$, $\varphi = 0$). In this range,

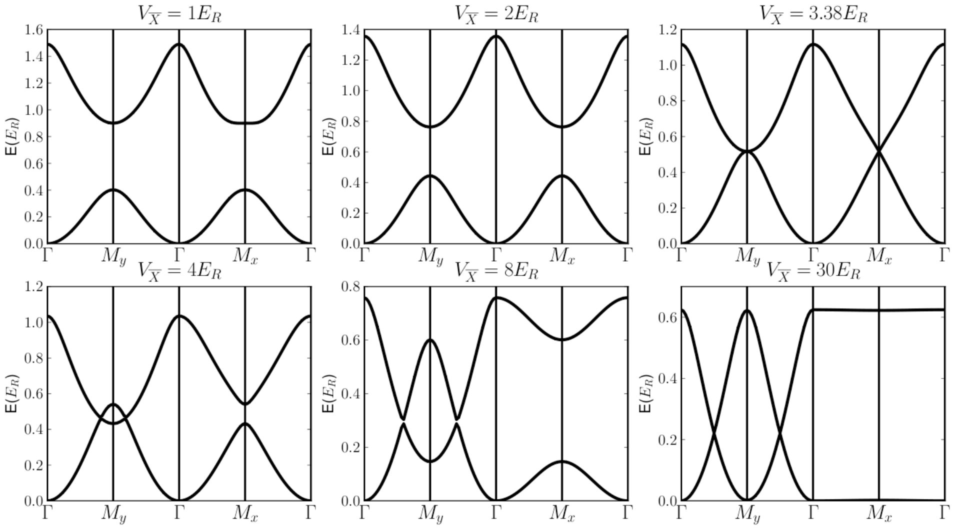

Figure 4.9: Band structure of the two lowest bands for various values of $V_{\overline{X}}$. The first two panels ($V_{\overline{X}} = 1$ and 2) correspond to the dimmer regime, the second two panels ($V_{\overline{X}} = 3.38$ and 4) to the stretched honeycomb regime and the last two panels ($V_{\overline{X}} = 8$ and 30) to the 1D-chain regime.

the potential of Eq. (4.18) covers three different regimes, as exemplified in Figs. 4.8a-c. These are the dimmer regime ($V_{\overline{X}} \sim 1$), the 1D-chain regime ($V_{\overline{X}} \sim 8$) and the stretched-honeycomb regime (intermediate values). As shown in Fig. 4.8a, the dimmer structure is characterized by a relatively low value of the potential in the region between A and B sites within the same unit cell. On the opposite, in the 1D-chain regime (Fig. 4.8c) the potential is small along the y direction connecting different minima, while it presents a high barrier between A and B sites of the same unit cell. The stretched-honeycomb regime (Fig. 4.8b) represents an intermediate configuration between these two limits.

Band structure

In order to gain insight on the properties of the different regimes, in Fig. 4.9 we analyze the band structure of the two lowest bands for selected values of $V_{\overline{X}}$. The path along which the energy dispersion is shown includes the points $\mathrm{M_x} = (1, 0)$ and $\mathrm{M_y} = (0, 1)$, where the most interesting features are expected [131]. We begin by considering the lowest value $V_{\overline{X}} = 1$, corresponding to the dimmer regime. At this value, the two lowest bands are separated by a gap all along the path. As $V_{\overline{X}}$ is increased, the gap decreases until $V_{\overline{X}} = 3.38$, where the two bands intersect at $\mathrm{M_x}$ and $\mathrm{M_y}$. It is noteworthy that while around $\mathrm{M_y}$ the band dispersion is parabolic, the bands intersect linearly at $\mathrm{M_x}$, a Dirac point. From now on, we will refer to this configuration as the *merging point.*

As the potential $V_{\overline{X}}$ is further increased, we observe different behaviors along $\Gamma - \mathrm{M_x}$ and $\Gamma - \mathrm{M_y}$. First, we will focus in the $\Gamma - \mathrm{M_x}$ direction. For $V_{\overline{X}} > 3.38$ we find that a gap opens all along the line, leading to the disappearance of the Dirac point. This gap continuously increases as $V_{\overline{X}}$ is further raised. Finally, at very high values of $V_{\overline{X}}$ ($V_{\overline{X}} >> V_X, V_Y$), we find no dispersion of the bands along this direction. This feature reflects that lattice sites hardly interact along the x direction, consistently with the shape of the calculated MLWFs in this regime, which resemble 1D-chains along the y direction (Fig. 4.8a).

The situation is significantly different along the $\Gamma - \mathrm{M_y}$ line. For $V_{\overline{X}} > 3.38$, we find a band-crossing that changes its location with $V_{\overline{X}}$. Noteworthy, the location of the band-crossing approaches $\mathrm{M_y}/2 \equiv \mathrm{M'_y} = (0, 1/2)$ as $V_{\overline{X}}$ increases. At very high values of $V_{\overline{X}}$ ($V_{\overline{X}} >> V_X, V_Y$), the two bands cross at $\mathrm{M'_y}$, and the dispersion is equal from $\Gamma - \mathrm{M'_y}$ to $\mathrm{M'_y} - \mathrm{M_y}$. Note also that the dispersion around Γ and $\mathrm{M_y}$ is completely parabolic.

The situation explained above can be interpreted again considering the 1D-chain-like structure of the potential. Indeed, considering the 1D-chain limit as an ideal 1D structure, the associated direct and reciprocal lattices would have the following vectors, respectively:

$$\mathbf{a}'_1 = 2\pi\hat{\mathbf{e}}_y, \tag{4.21}$$

$$\mathbf{b}'_1 = \hat{\mathbf{e}}_y, \tag{4.22}$$

with $\hat{\mathbf{e}}_y$ the unit vector along the y direction. In this effective 1D system, the 1D BZ is a line from $-0.5\hat{\mathbf{e}}_y$ to $+0.5\hat{\mathbf{e}}_y$. For positive k_y, the end of this line would be precisely $\mathrm{M'_y}$, which is halfway from Γ to $\mathrm{M_y}$, as depicted in Fig. 4.7b. With this in mind, the band-crossing at $\mathrm{M'_y}$ depicted in the last panel of Fig. 4.9 would be analogous to the band-crossing of a free-electron band at the zone boundary, and $\mathrm{M_y}$ would correspond to the high symmetry point Γ at the second BZ.

MLWFs

As we have done in the case of the honeycomb potential analyzed in Sec. 4.2, in the present case we can also calculate the MLWFs considering the two lowest Bloch bands. The resulting MLWFs for different values of $V_{\overline{X}}$ are illustrated in Figs. 4.8 (c-d) (results are shown for sublattice A). In all the cases, MLWFs are exponentially localized around the A site of the central unit cell, but present a non-negligible contribution around the neighboring potential minima too. As shown in the figure, the structure of the potential determines the shape of the MLWFs. For $V_{\overline{X}} = 1$, see Fig. 4.8d, we find a large contribution of the MLWF around the B site of the central unit cell, consistent with the dimmer structure of the potential. The situation is very

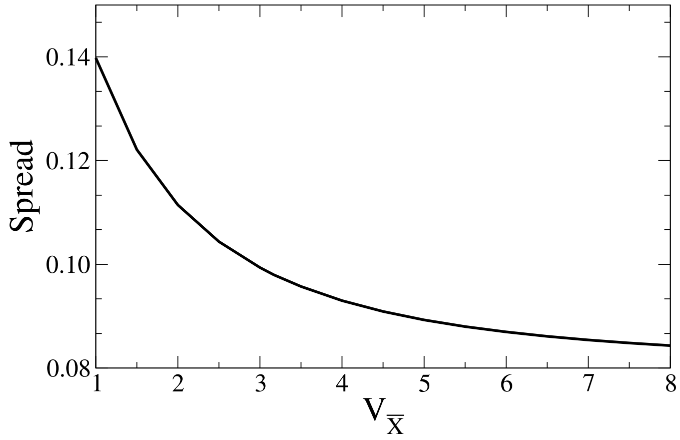

Figure 4.10: Spread (units of k_L^2) of the MLWFs as a function of $V_{\overline{X}}$, in the regime of the experiment [131] ($V_X = 0.28$, $V_Y = 1.8$, symmetric case).

different for $V_{\overline{X}} = 8$ (Fig. 4.8f), which shows a MLWF highly localized along the y axis, resembling the 1D-chain structure of the potential. The stretched-honeycomb regime represented by Fig. 4.8e constitutes an intermediate stage between the two limits.

In order to analyze the degree of localization of the MLWFs, in Fig. 4.10 we show the spread Ω of the MLWFs (Eq. (1.25)) as a function of $V_{\overline{X}}$. The figure shows that increasing $V_{\overline{X}}$, Ω rapidly decreases in the regime of low $V_{\overline{X}}$, while it almost saturates in the opposite limit. This indicates that the TB approach is expected to work better for the stretched-honeycomb and 1D-chain regimes than for the dimmer case.

4.3.2 Tunneling coefficients

We now focus on the tunneling coefficients associated to the MLWFs. For the present example, we have truncated the TB expansion of Eq. (4.5) including all possible tunneling coefficients between neighboring cells, as indicated in Fig. 4.7a. We distinguish between diagonal and off-diagonal terms in the band index.

(i) Diagonal terms connecting the minima located at points of the same type $n = A$ or $n = B$, red arrows in Fig. 4.7a. We use the following notation based on Eq. (4.5):

$$j_1^n \equiv T_{nn}^{(1,-1)} = T_{nn}^{(-1,1)}, \tag{4.23}$$

$$j_2^n \equiv T_{nn}^{(1,0)} = T_{nn}^{(0,1)} = T_{nn}^{(0,-1)} = T_{nn}^{(-1,0)}, \tag{4.24}$$

$$j_3^n \equiv T_{nn}^{(1,1)} = T_{nn}^{(-1,-1)}. \tag{4.25}$$

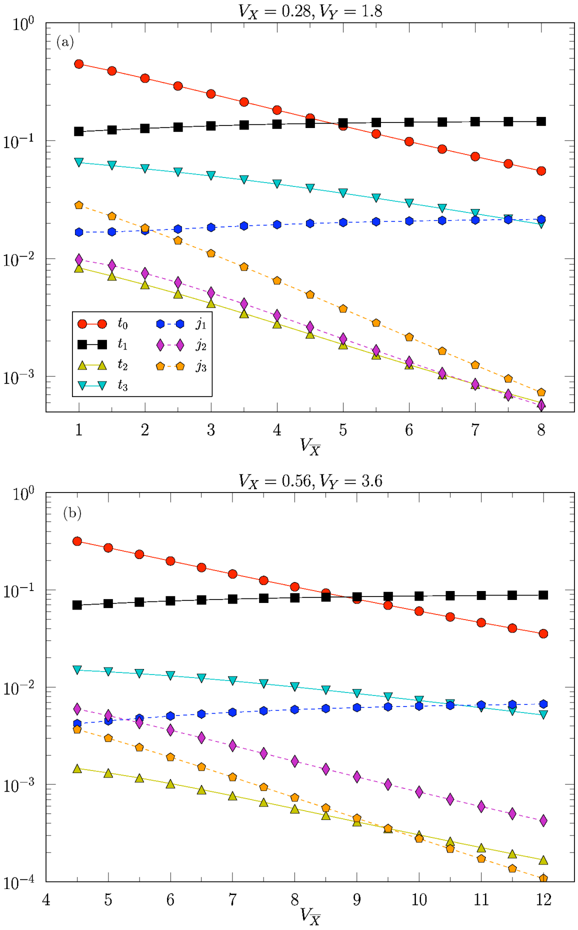

Figure 4.11: Evolution of various tunneling coefficients as a function of $V_{\overline{X}}$, covering the whole range from the dimmer to the 1D-chain structures. (a) Experimental regime, $V_X = 0.28$, $V_Y = 1.8$ [131]. (b) Proper TB regime, $V_X = 0.56$, $V_Y = 3.6$.

In the symmetric case $\theta = \pi$, $\varphi = 0$, we further have that

$$j_i^A = j_i^B \equiv j_i, \quad i = 1, 3. \tag{4.26}$$

(ii) Off-diagonal terms connecting the minima located at points of different type, blue arrows in Fig. 4.7a. We redefine the tunneling coefficients as

$$\begin{aligned}
t_0 &\equiv T_{nn'}^{(0,0)}, && (4.27)\\
t_1 &\equiv T_{nn'}^{(1,0)} = T_{nn'}^{(0,1)}, && (4.28)\\
t_2 &\equiv T_{nn'}^{(-1,-1)}, && (4.29)\\
t_3 &\equiv T_{nn'}^{(1,-1)} = T_{nn'}^{(-1,1)}, && (4.30)
\end{aligned}$$

with $n, n' = A, B$ and $n \neq n'$.

The behavior of the tunneling coefficients in the considered range for $V_{\overline{X}}$ is shown in Fig. 4.11a. We first focus on the value $V_{\overline{X}} \simeq 1$. We find that the ratio between the two dominant coefficients t_0/t_1 is $\backsimeq 10$. This reflects the dimmer structure of the potential, since t_0 connects sites A and B (see Fig. 4.7a). Noteworthy, t_2 is by far the next largest coefficient, comparable in magnitude to t_1. The importance of t_2 reveals that the tunneling between neighboring dimmers in the x direction is considerable (see t_2 in Fig. 4.7a). The rest of the coefficients have a significantly lower value compared to t_0, t_1 and t_2.

As $V_{\overline{X}}$ is increased, the various tunneling coefficients evolve in two different ways. Most of them decrease in magnitude, reflecting the stronger localization of the MLWFs as we approach a more TB regime. This could be considered a 'normal' behavior, as it was also observed for the tunneling coefficients of the perfect honeycomb lattice covered in the previous section (see Fig. 4.4). However, two of the coefficients, namely t_1 and j_1, increase in magnitude as $V_{\overline{X}}$ is increased. This apparently 'inverse' behavior reflects the evolution of the potential of Eq. (4.18) from the dimmer to the 1D-chain structure, as these coefficients connect potential minima inside the 1D-chains. Owing to this 'inverse' behavior, t_1 becomes the dominant coefficient for $V_{\overline{X}} \gtrsim 4.5$. Similarly, j_1 becomes larger than j_3 and even t_2 for $V_{\overline{X}} \gtrsim 7.5$. It is therefore clear that varying the potential amplitude can also modify the role of the different tunneling coefficients.

4.3.3 Accuracy of the tight binding model

We proceed now to test the validity of the TB model in terms of the calculated tunneling coefficients. With this aim, in Figs. 4.12a-f we compare the exact energy dispersion with the TB spectrum (cf. Appendix F) in the three regimes. We consider two different TB approximations, one including just t_0, t_1 and t_2 (corresponding to the universal Hamiltonian of Ref. [143]), and that including all the coefficients in Fig. 4.11a The figures show that the main features, including the band-crossing along the k_y direction in Figs. 4.12e-f, are well reproduced by both approximations, though the TB model with just t_0, t_1 and t_2 is not capable of approximating the exact bands with sufficient accuracy.

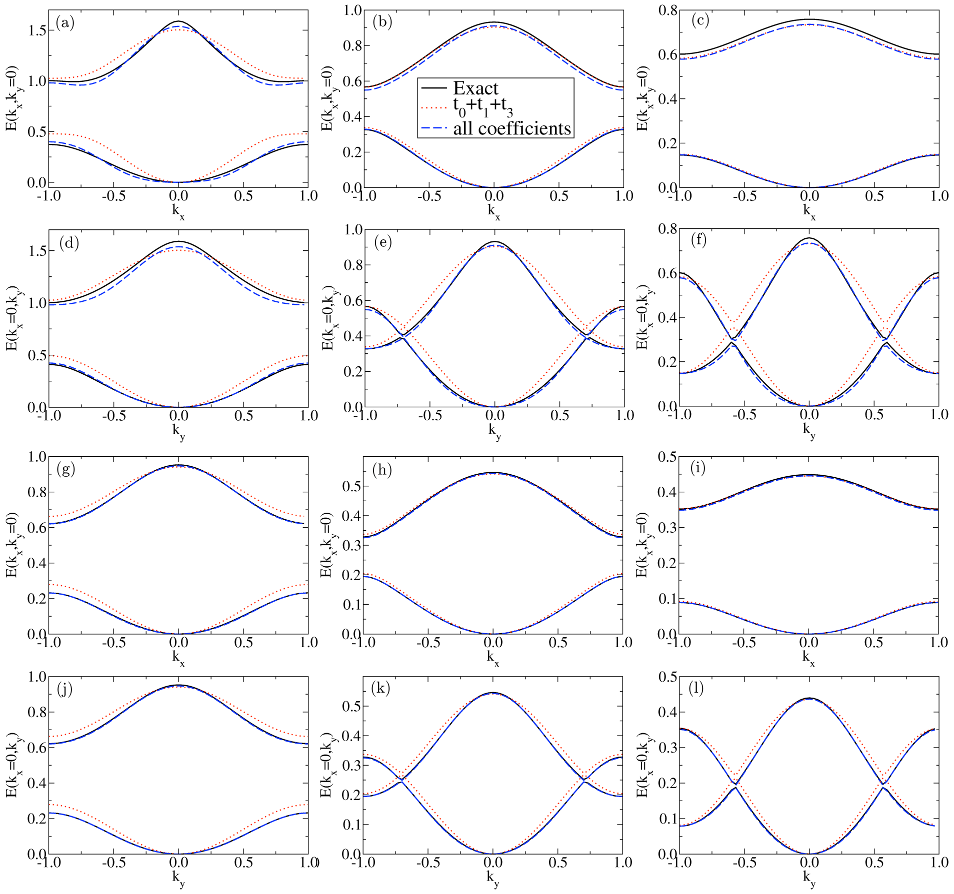

Figure 4.12: Cuts of the exact energy bands (black solid line) compared to two TB approximations: one with just t_0, t_1 and t_2 (red dotted line), and the other with all the coefficients in Fig. 4.7a (blue dashed line). Panels (a-f) show the results for the experimental parameter setup of Tarruel and co-workers: $V_X = 0.28$, $V_Y = 1.8$ [131], while panels (g-l) correspond to $V_X = 0.56$, $V_Y = 3.6$. Panels (a-c) show cuts along k_x ($k_y = 0$) for $V_{\overline{X}} = 1$ (dimmer regime), $V_{\overline{X}} = 4.5$ (stretched-honeycomb regime) and $V_{\overline{X}} = 8$ (1D-chain regime), respectively. Panels (d-f) show cuts along k_y ($k_x = 0$) for the same parameters as in (a-c). Panels (g-l) are organized as panels (a-f), but with $V_{\overline{X}} = 4.5$ (dimmer regime), $V_{\overline{X}} = 8$ (stretched-honeycomb regime) and $V_{\overline{X}} = 12$ (1D-chain regime).

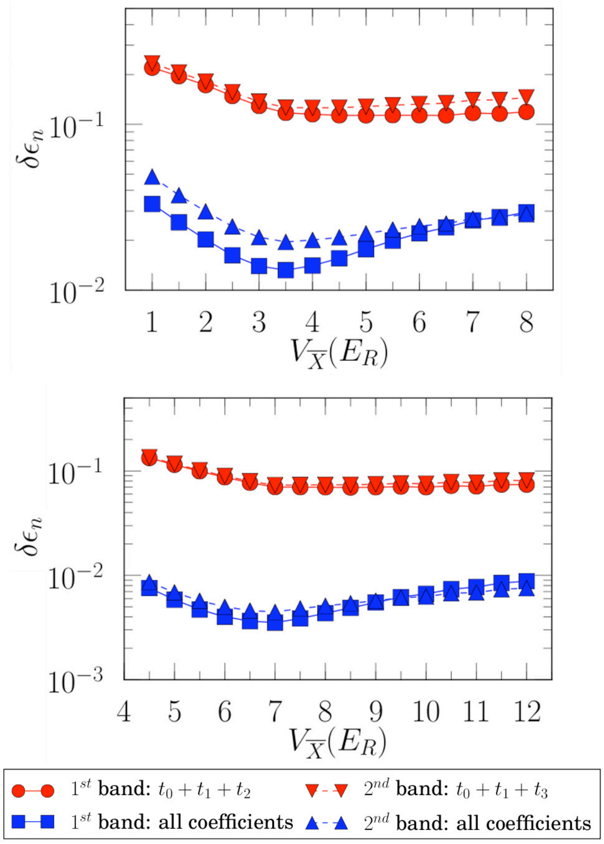

Figure 4.13: Calculated energy mismatch δE_n for the two bands including the two TB approximations discussed in the text. (a) and (b), respectively, show the results for the experimental and TB regimes.

In order to test further the accuracy of the TB model, in Fig. 4.13a we analyze the calculated mismatch between the exact and approximate energy spectra (Eq. 4.13) as a function of $V_{\overline{X}}$. We find that even the approximation including all the coefficients considered yields a mismatch above 1% in all the parameter regime. This is significantly greater than the mismatch of the TB model for the ideal honeycomb potential (Fig. 4.6), which produces an error below 1% in a broad parameter regime. The quality of the approximation could be improved by considering more coefficients in the TB model, but this would make the approach much less simple and practical.

At this point, we consider a different set of values for the potential parameters that correspond to a well defined TB regime, while keeping the same potential structure. In particular, we have considered the parameter values $V_X = 0.56$, $V_Y = 3.6$ and $V_{\overline{X}}$ ranging from 4 to 12, corresponding to twice the values of Tarruel and co-workers [131]. The aim is to obtain a better compromise between the accuracy and simplicity of the model than in the experimental parameter setup. The calculated tunneling coefficients are illustrated in Fig. 4.11b, showing the same general structure as the ones in Fig. 4.11a, except for minor differences regarding the smallest coefficients. The corresponding energy dispersion is shown in Figs. 4.12(g-l) in the dimmer, stretched-honeycomb and 1D-chain regimes. In this case, already the lowest order approximation with just the coefficients t_0, t_1 and t_2 provides a remarkable agreement with the exact data. The approximation including all the coefficients yields almost indistinguishable results compared to the exact dispersion. This is also reflected in the calculated mismatch for this parameter regime, shown in Fig. 4.13b. We find that the mismatch $\delta\epsilon_n$

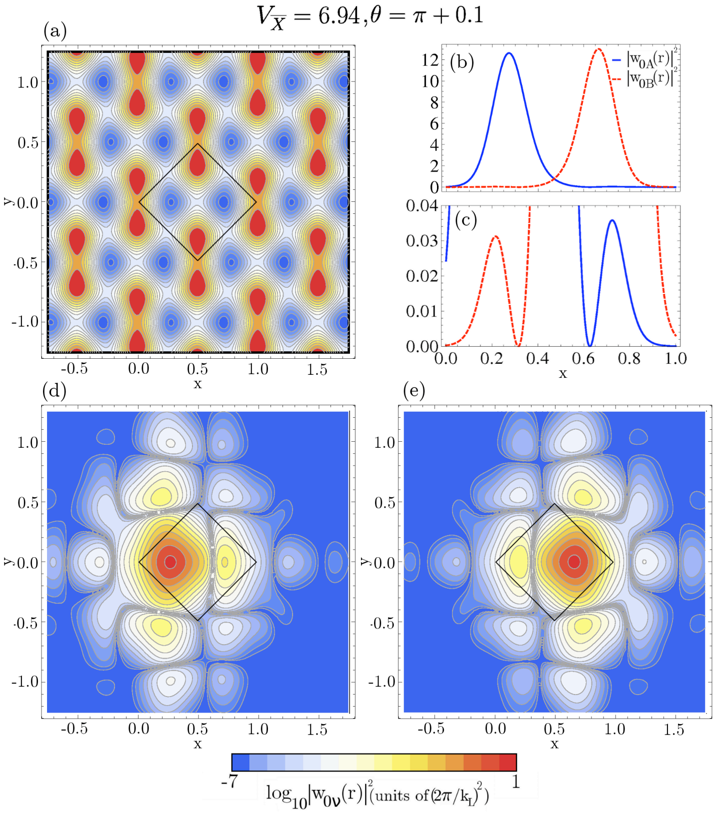

Figure 4.14: Asymmetric structure corresponding to $\theta = \pi + 0.1$, with potential parameters $V_X = 0.56$, $V_Y = 3.6$, $V_{\overline{X}} = 6.94$ (merging point). (a) illustrates the structure of the potential for this configuration, showing a deeper minimum at sublattice B than in A (color code as in Fig. 4.8). (b) and (c) show one dimensional profiles of $|w_{0A}(x, y = 0)|^2$ (solid, blue) and $|w_{0B}(x, y = 0)|^2$ (dashed, red) in the central unit cell. Note the different distributions of the two MLWFs, as a consequence of the parity breaking. This is evident also from the two dimensional plots of $|w_{0A}(\mathbf{r})|^2$ and $|w_{0B}(\mathbf{r})|^2$, in (d) and (e), respectively.

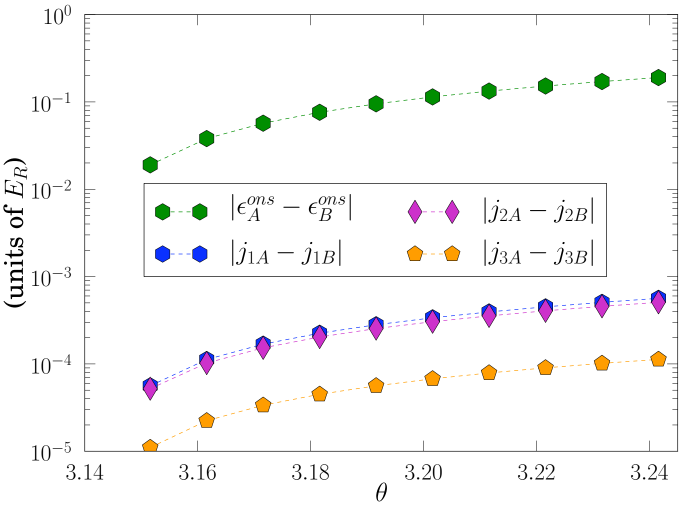

Figure 4.15: Splitting of the diagonal coefficients as a function of the angle θ (at the merging point: $V_X = 0.56$, $V_Y = 3.6$, $V_{\overline{X}} = 6.94$). Note that $|E_A - E_B| = 2|\epsilon|$, see Eq. (F.9).

is overall one order of magnitude smaller than in the experimental regime (Fig. 4.13a). It is noteworthy that the best approximation in Fig. 4.13b has an error below 1% in all the range of $V_{\overline{X}}$. Therefore, the setup $V_X = 0.56$, $V_Y = 3.6$ corresponds to a proper TB regime, accurately reproducible by TB models based on the MLWFs.

Before concluding this section, it is worth to mention the two different trends observed in the behavior of the mismatch. Focusing on Fig. 4.13a, we find that for $V_{\overline{X}} \lesssim 4.5$, $\delta\epsilon_n$ decreases as $V_{\overline{X}}$ is increased. This evolution could expected since in this parameter regime, the MLWFs become much more localized as the potential is raised (see Fig. 4.10). For $V_{\overline{X}} \gtrsim 4.5$, in contrast, the mismatch increases with increasing $V_{\overline{X}}$. We recall from Fig. 4.11 that some tunneling coefficients corresponding to sites inside the 1D-chains grow as $V_{\overline{X}}$ is increased (see t_1 and j_1 as an example). When approaching the 1D-chain limit, some of these coefficients that are not considered in our TB model become relevant, so that the quality of the approximation decreases.

4.3.4 Breaking parity

In this final section we analyze the effect of the asymmetry introduced in the potential of Eq. (4.18) by letting $\theta \neq \pi$. For simplicity, we will restrict the analysis to the proper TB parameter regime $V_X = 0.56$, $V_Y = 3.6$. For $\theta \neq \pi$, the two potential minima in the unit cell become non-degenerate [131]. In Fig. 4.14a we exemplify this situation by illustrating the structure of the potential for $\theta = \pi + 0.1$ at the merging point, which in this regime

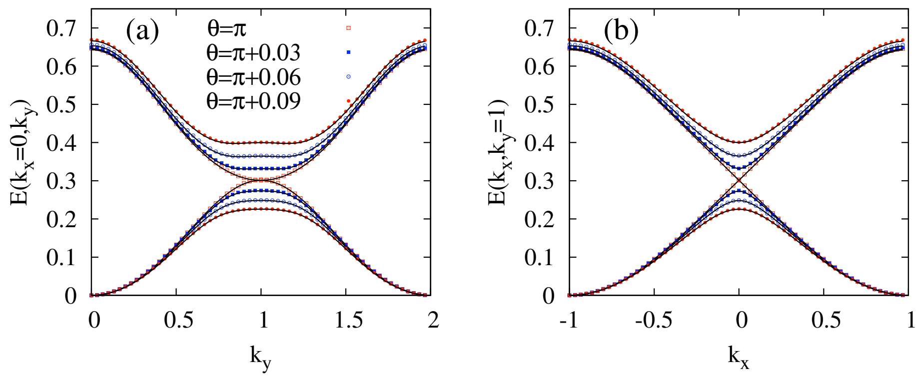

Figure 4.16: Cuts of the energy bands around the merging point $\mathrm{M_y} = (0, 1)$ for different values of the parity breaking angle θ. The exact Bloch bands (dots) are compared to the full TB model (solid line), as a function of k_y (at $k_x = 0$) (a), and of k_x (at $k_y = 1$) (b). The picture refers to the TB regime $V_X = 0.56$, $V_Y = 3.6$, $V_{\overline{X}} = 6.54$.

happens at $V_{\overline{X}} = 6.54$. The figure shows a deeper minimum at site B than in A. Correspondingly, the associated MLWFs exhibit a higher localization around B than around A, as illustrated in Figs. 4.14 b-e.

As a consequence of the parity breaking, the degeneracy of the diagonal coefficients is also broken, for both the onsite energies E_n (Eq. (4.6)) and the diagonal tunneling coefficients j_i^n, $n = A, B$ (Eq. (4.25)). In Fig. 4.15 we illustrate the splitting between the A and B terms for these coefficients for small deviations from $\theta = \pi$. [1] As shown in the figure, the deviations grow as θ deviates from π, reflecting the asymmetry of the potential, which strongly affects the energy dispersion. Indeed, as shown in the experiment by Tarruel and co-workers [131], a gap can be opened at the Dirac points by breaking the invariance under parity. Here we show that the variation of the tunneling coefficients shown in Fig. 4.15 is able to accurately reproduce the exact dispersion law and, in particular, the opening of the mass gap at the Dirac points. With this aim, in Fig. 4.16 we compare the exact and TB band dispersion for different values of $\theta \neq \pi$ at the merging point. As shown in the figure, even small deviations from $\theta = \pi$ give rise to a appreciable gap at the Dirac point, which is accurately reproduced by our model.

---

[1] The off-diagonal tunneling coefficients are weakly affected in these range of values of θ.

4.4 Conclusions

In this chapter we have considered MLWFs as a basis for TB models of optical lattices. We have described how to calculate the tunneling coefficients that connect the continuous and discrete systems in different lattice geometries.

As the first example, in Sec. 4.2 we have analyzed the perfect honeycomb optical lattice with close connections to the graphene physics. The TB model in terms of just three nearest neighbor coefficients calculated with the aid of the MLWFs has accurately reproduced the features of the continuous system. In particular, the characteristic Dirac point has been very well reproduced by our model, with an energy mismatch much below 1% in the regimes of practical interest. The results presented in this section have demonstrated the power of the MLWFs in determining the parameters of TB Hamiltonians describing ultracold atoms in optical lattices.

After analyzing the ideal honeycomb lattice, in Sec. 4.3 we have applied the method to a tunable honeycomb optical lattice [131]. This more complex example has allowed us to consider several lattice geometries, such as the dimmer, stretched-honeycomb and 1D-chain structures. We have derived the corresponding TB models, and calculated the MLWFs and tunneling coefficients for different lattice configurations. The results have shown that the energy spectrum, including the position of Dirac points, can be accurately reproduced also in these cases. Furthermore, the present example has allowed us to study the effect of the asymmetry introduced by breaking the degeneracy of the two potential minima contained in the unit cell. The massive Dirac points that accompany such parity breaking have been very well reproduced by our TB model, showing that MLWFs successfully adapt to complex and variable optical lattice geometries.

Chapter 5

Final conclusions

Throughout this work, we have applied an *ab-initio* approach based on DFT and MLWFs for calculating several properties of diverse systems, including spin-flip excitations in surfaces with strong spin-orbit interaction, plasmon dispersion under pressure in a simple metal, sodium, and tight binding models for 2D optical lattices. The analysis of this rather wide variety of topics has been possible thanks to the ability of the MLWFs for successfully adapting to diverse systems.

In the context of surfaces with spin-orbit interaction, we have analyzed the Tl/Si(111), Au(111) and Pb/Ge(111)$-\beta\sqrt{3}\times\sqrt{3}R30^\circ$ structures. The calculations based on the generalization of the DFT to the noncollinear spin case have accurately described their ground state properties, showing in all cases a very good agreement with state-of-the-art ARPES and SR-ARPES measurements. Additionally, we have analyzed the low-energy excitations induced by an external electromagnetic field between spin-split surface states. The use of MLWFs has allowed to consider very fine $\mathbf{k}$ meshes needed to study such excitations. With this technique, we have found that the spin-orbit interaction can play an important role in the light absorption spectrum of surfaces, which is one of the main results of this work.

The properties of sodium, a simple metal, have also been the focus of attention in this work. As it is the case of similar elements such as lithium and calcium, sodium exhibits interesting phenomena when pressure is applied to it. We have performed an exhaustive *ab-initio* analysis of the ground and excited state properties of sodium under pressure. MLWFs have been used as the basis for calculating the linear response function within TDDFT, a powerful approach that has allowed us to study the collective charge excitations, known as plasmons. Our analysis has predicted the existence of an anisotropic interband plasmon in the fcc phase that emerges and disappears at finite values of the momentum, indicating an unexpected departure of sodium from the free-electron-like behavior. Additionally, we have found very low-energy plasmons in the high pressure phases oP8 and tI19 (above

125 GPa), which explain recent measurements of a drastic drop of reflectivity in these phases. In conclusion, the calculations presented in this work have provided clear fingerprints of pressure-induced complexity in sodium.

In the last chapter of this work we have applied the MLWFs in a context in which they have not been fully exploited yet; the context of cold atoms trapped in 2D optical lattices. We have constructed tight binding models of several 2D optical lattices, allowing to map the continuous system into a discrete one in terms of a few tunneling coefficients. Noteworthy, our tight binding models have accurately reproduced the properties of the continuous system, such as the energy spectrum and the so-called Dirac points, with an energy mismatch much below 1%. Therefore, The results presented in this work have demonstrated the power of the MLWFs in determining the parameters of tight binding models describing cold atoms in optical lattices.

Publications

Part of the work presented here has been published in the following references:

1. *Relativistic effects and fully spin-polarized Fermi surface at the Tl/Si(111) surface*,
   Julen Ibañez-Azpiroz, Asier Eiguren and Aitor Bergara,
   Physical Review B 84, 125435 (2011)
2. *Spin-Flip Transitions Induced by Time-Dependent Electric Fields in Surfaces with Strong Spin-Orbit Interaction*,
   Julen Ibañez-Azpiroz, Asier Eiguren, Evgeny Ya. Sherman and Aitor Bergara,
   Physical Review Letters 109, 156401 (2012)
3. *Tight-binding models for ultracold atoms in honeycomb optical lattices*,
   Julen Ibañez-Azpiroz, Asier Eiguren, Aitor Bergara, Giulio Pettini and Michele Modugno,
   Physical Review A 87, 1011602(R) (2013)
4. *Self-consistent tight-binding description of Dirac points moving and merging in two dimensional optical lattices*,
   Julen Ibañez-Azpiroz, Asier Eiguren, Aitor Bergara, Giulio Pettini and Michele Modugno,
   Submitted to **Physical Review A**
5. *Spin-flip transitions and departure from the Rashba model in the Au(111) surface*,
   Julen Ibañez-Azpiroz, Evgeny Ya. Sherman, Aitor Bergara and Asier Eiguren
   Submitted to **Physical Review B**
6. *Ab-initio analysis of plasmon dispersion in sodium under pressure*,
   Julen Ibañez-Azpiroz, Bruno Rousseau, Asier Eiguren and Aitor Bergara
   To be submitted

Acknowledgements

I would like to acknowledge in first place the people of the research group in Leioa, who have been the working-mates during the years in which this thesis has been done. Aitor and Asier, I deeply acknowledge all your help and confidence, the doors you have opened for me, your patience, and all you have taught to me. For giving much more than receiving, thanks truly. I really hope you have enjoyed these years as much as I have. Ion and Miguel, the 'older brothers', have not stopped of helping me during my thesis, as well as the 'younger brothers/sisters' Ainhoa and Peio (eutsi gogor!). Together with Idoia and Aritz, thanks very much to all of you, time flies when one works with such nice people.

A big part of the work presented in this thesis has been done in collaboration with people outside the research group in Leioa. Eugene has been there from the beginning till the end of my thesis, constantly giving ideas and helping whenever needed, I owe a very big part of this work to him, eskerrikasko Eugene. We started the collaboration with Michele and Giulio only a year ago, it is incredible how fast and well we have understood each other, grazie mile Michele e Giulio. I would also like to thank Michel Côté, who took me in his group in Montreal, where I felt like at home during the four months of stay. Finally, I would like to make a special mention to Bruno, who has been at my side in two different stages of my thesis, in Leioa and in Montreal. For helping me in physics, computational aspects, during my stay in Michels group, discovering Montreal and Quebec... for all that and much more, thanks truly Bruno.

Outside research, there is plenty of people to acknowledge. People of the 'Bekadromos', older and younger, locals and foreigners. People from the 'Kuadrila', the milestone, and also the friends from Bilbao. Of course, aita eta ama, for everything, together with aunts-uncles-cousins-grandmothers. And also Nerea, for helping me so much this last year.

Following Miguels thesis, I feel the necessity to thank all the people who has helped developing the free software, as well as anyone who took the time to write an answer in some blog in the internet to some technical, surely boring question. Finally, I also feel the necessity to thank the pre-university teachers of the public school I have had from when I was a kid till high-school. Their high quality work is in my opinion rarely acknowledged.

I would like to make a special mention to Rafa, Txomin and Otxoto, who provided me with the necessary tools for physics.

Regarding the institutions, I would like to acknowledge financial support from the Basque Government through the PhD grant. I would like to also acknowledge the University of the Basque Country and the Donostia International Physics Center.

//

Lehen eskerrak Leioako ikerkuntza taldekoei eman nahi nizkieke, lan hau bertan egindakoa baita. Aitor eta Asier, zinez eskertzen dizuet urte guzti hauetan zehar etengabe eman didazuen laguntza eta konfidantza, ireki dizkidazuen aukerak, euki duzuen pazientzia, irakatsi didazuen guztia... milesker. Nere lehen urratsak izan direnez, lau urte hauetako elkarlanak askoz ere gehiago eman dit niri zuei baino. Horregatik, jasotakoa baina askoz ere gehiago emateagatik, eskerrikasko. Soilik espero dut denbora hontan zehar nik bezain ongi pasa izana. Etengabe lagundu eta irakatsi didatenen artean daude Ion eta Miguel ere, tropeleko 'anaia zaharrak', Ainhoa eta Peio (eutsi gogor!) 'anaia/arreba gazteak' diren bezela. Idoia eta Aritzekin batera, eskerrikasko denori, denbora abian doa horrelako talde batean lan egiten denean.

Tesi hontan aurkeztutako zati haundi bat taldetik kanpoko kolaboratzaileekin elkarlanean egin da. Eugene tesi hasieratik bukaerara egon da hor, etengabe ideiak emanez eta laguntza eskainiz, tesi honen zati oso haundi bat zor diot berari, eskerrikasko Eugene. Michele eta Giuliorekin harremanak duela urte bete eskas hasi genituen, harrigarria izan da ze ondo ulertu garen hasieratik, grazie mile Michele e Giulio. Michel Côté-ri ere eskerrak eman nahi nizkioke Montrealen bere taldean hartu izanagatik, etxean bezela sentitu nintzen han pasa nituen lau hilabeteetan zehar. Azkenik, bereziki eskertu nahiko nuke Bruno, tesiko bi etapatan egon baita nerekin batera, Leioan eta Montrealen. Fisikan, teknika konputazionaletan, Michel-en taldean egonaldia prestatzen, Montreal erakusten... guzti horretan eta askoz gehiagotan laguntzeagatik, eskerrikasko Bruno.

Lan arlotik kanpo, asko daude eskertzeko. Bekadromoetako jendea, orain daudenak eta egon zirenak, hemengoak eta kanpokoak. Kuadrilakoak, beti (beti!) hor egoteagatik, baita Bilboko lagunak eta izandako pixukide guztiak ere. Noski, aita eta ama, den-denagatik, izeba-osaba-lehengusuak eta amañi ahaztu gabe. Azken boladan hor egon den Nerea ere, besteak beste esgintzeak horren ondo sendatzeagatik.

Miguelen tesiko eskerretatik kopiatuz, software askea garatzen lagundu duen edonori eskerrak ematea derrigorrezkoa iruditzen zait, baita era desinteresatuan hainbat eta hainbat arazo tekniko ebazteko ezinbestekoak diren edozein motatako blog-ak idazten dituztenei ere. Azkenik, oinarrizko irakaskuntza publikoa eta kalitatezkoa eman didaten irakasleak eskertu nahiko nituzke, haien lana gutxitan aipatzen dela iruditzen baitzait. Hiru izen, Rafa, Txomin eta Otxoto, azpimarratu nahi nituzke, Fisikan ezinbestekoak

izan zaizkidan tresnak emateagatik.

Erakundeei dagokienez, Eusko Jaurlaritza eskertzen dut tesia egin ahal izateko beka emateagatik, baita Euskal Herriko Unibertsitate publikoa eta Donostia International Physics Center ere.

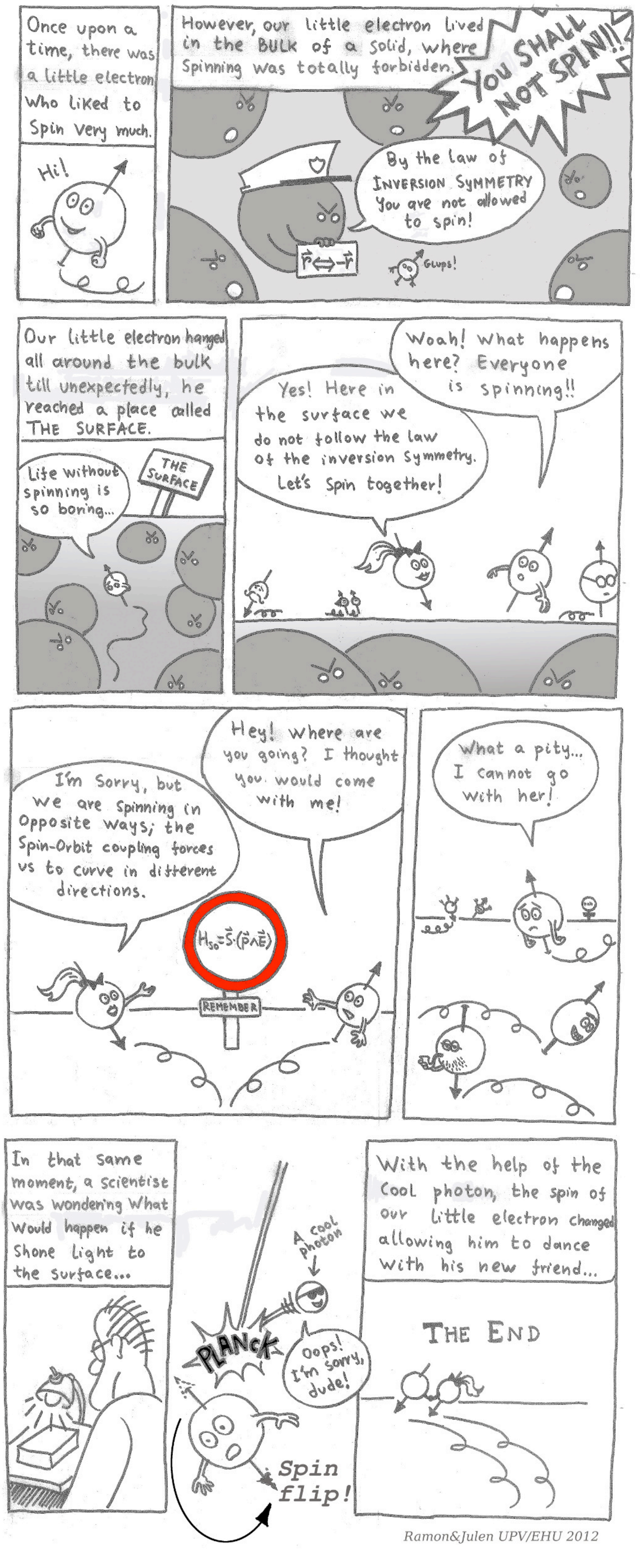

Ramon&Julen UPV/EHU 2012

Appendices

Appendix A

Slab representation of a surface

Computational algorithms that implement the DFT or SDFT based on plane waves are usually adapted to the periodicity of solids. In practice, one defines the crystal unit cell in real space, which is to be repeated in the directions corresponding to the three direct lattice vectors that define the unit cell. In the case of a surface, however, periodicity is lost along the direction perpendicular to the surface. In order to apply these algorithms, the surface must be represented by the so-called repeated slab technique. This consists on introducing a sufficiently large slab along the surface perpendicular direction that resembles an entire surface. This means that the slab must contain enough atoms in order to reproduce both, the properties of the bulk and the surface. Also, it needs to contain enough vacuum along the surface perpendicular direction so that when repeated, the two sides of the slab do not spuriously interact among themselves. Along the plane parallel to the surface, on the other hand, the usual unit cell is maintained.

An important point when building an slab is to determine the minimum number of atoms that it needs to contain in order to properly emulate the properties of the bulk and the surface. This optimization process is based on the following energy considerations. Let E_n represent the total energy of the surface slab with n atoms and ϵ_{bulk} the energy of a single bulk atom obtained from a standard bulk calculation. We note that due to the different environments, ϵ_{bulk} is different from the energy of an atom located near the surface. Taking ϵ_{thr} as the energy threshold determining the accuracy of the minimization, when $|E_{n+1} - E_n - \epsilon_{\text{bulk}}| < \epsilon_{\text{thr}}$, it is safe to conclude that n atoms are enough to model the surface since adding the $n + 1$th atom increments the total energy by ϵ_{bulk}, meaning that this atom plays the role of a bulk atom; therefore, the surface is already well approximated.

A schematic illustration of a surface slab is included in Fig. A.1. This slab is meant to represent the Tl/Si(111) surface, consisting of silicon bulk

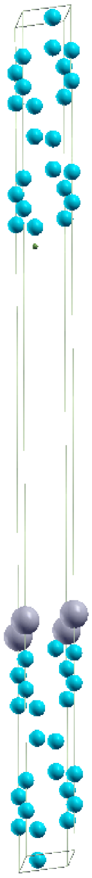

Figure A.1: Schematic representation of the Tl/Si(111) surface slab with a hydrogen overlayer covering the opposite side of the slab. Grey, blue and green balls denote Tl, Si and H atoms, respectively.

atoms, which crystallize in the diamond structure, and a thallium overlayer covering the (111) termination (cf. Sec. 2.1.2). At the opposite side of the slab, we have introduced a hydrogen overlayer in order to saturate the dangling bonds of the corresponding Si(111) termination. This is a common and safe procedure, since electron states associated to the hydrogen overlayer lie always well below the Fermi level and, therefore, have no effect in the chemical properties of the surface in which we are interested. In the present example, after the optimization process, we have found that 24 Si atoms are enough to approximate the surface.

Appendix B

Rashba model

In this appendix we review the basic aspects of the Rashba model [53] for a 2D free-electron-like gas, which is broadly considered as the standard model for analyzing the properties of surface states under strong spin-orbit interaction (SOI) [37]. Within this model, electrons are considered as free particles under the action of a simplified SOI term,

$$H_R = \alpha_R(\boldsymbol{\sigma} \times \mathbf{p})_z, \tag{B.1}$$

with α_R the so-called Rashba parameter that controls the strength of the SOI. The subscript z in Eq. (B.1) means that only this component of the vector product $\boldsymbol{\sigma} \times \mathbf{p}$ must be kept.

The so-called Rashba SOI term of Eq. (B.1) contains two major simplifications compared to the general SOI term (Eq. (2.4)). First, it assumes that the only finite component of the potential gradient is along the surface-perpendicular direction z, which is why we only keep the z component of the vector product. Physically, this gradient constrains the electrons to the 2D (x, y) plane. Second, it assumes that the potential gradient is constant, i.e. independent of $\mathbf{r}$, making the Rashba SOI term also independent of the position. Thanks to these simplifications, the Rashba model is analytically solvable.

With these considerations in mind, the full Hamiltonian in the Rashba model is given by

$$H_0 = \frac{\mathbf{p}^2}{2m^*} + \alpha_R(\boldsymbol{\sigma} \times \mathbf{p})_z, \tag{B.2}$$

with m^* the electron effective mass. For an in-plane Bloch vector $\mathbf{k} = (k_x, k_y) = k(\cos\varphi, \sin\varphi)$, the spinor eigenfunctions of the above Hamiltonian are

$$\phi_{\mathbf{k},\pm}(\mathbf{r}) = \frac{e^{i\mathbf{k}\cdot\mathbf{r}}}{2\pi}\frac{1}{\sqrt{2}}\begin{pmatrix} ie^{-i\varphi/2} \\ \pm e^{i\varphi/2} \end{pmatrix}. \tag{B.3}$$

Above, ± denotes the 'spin-up' and 'spin-down' states with respect to the

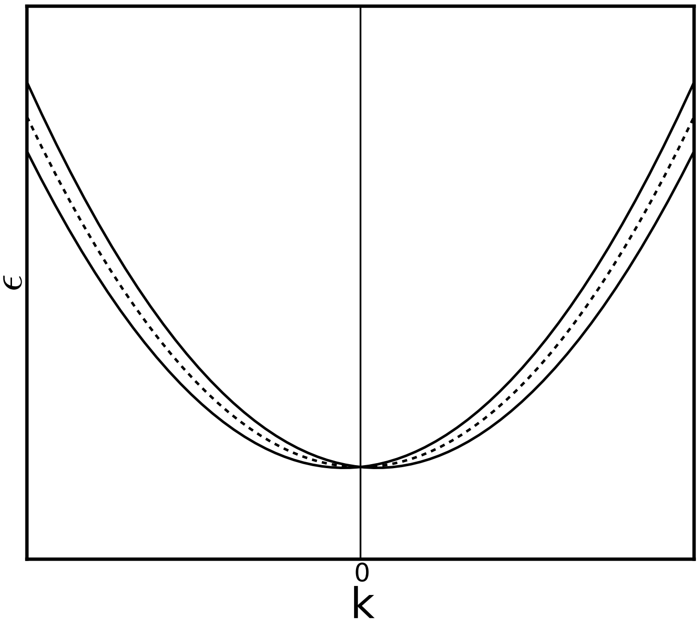

Figure B.1: Schematic illustration of the energy spin-splitting in the Rashba model: solid lines denote the energy dispersion of Eq. (2.19), while the dashed lines denote the original free-electron-like dispersion (without the linear Rashba term).

spin-polarization axis

$$\mathbf{m}_{\pm}(\mathbf{k}) = \langle \phi_{\mathbf{k},\pm} \,|\, \boldsymbol{\sigma} \,|\, \phi_{\mathbf{k},\pm} \rangle = \pm\frac{1}{2} \begin{pmatrix} \sin\varphi \\ -\cos\varphi \\ 0 \end{pmatrix} \perp \mathbf{k}. \tag{B.4}$$

The above equation predicts that the spin-polarization is independent of the momentum magnitude and perpendicular to both, the surface-perpendicular direction z and the electron momentum $\mathbf{k}$. Furthermore, it predicts opposite spin-polarization for the spin-split states.

Besides the kinetic contribution, the energy dispersion in the Rashba model contains a term linear in momentum,

$$\epsilon_{\pm}(\mathbf{k}) = \frac{\mathbf{k}^2}{2m^*} \pm \alpha_R |\mathbf{k}|. \tag{B.5}$$

Therefore, the effect of the Rashba SOI is to break the original two-fold spin-degeneracy through the term $\alpha_R|\mathbf{k}|$, with the exception of the high symmetry point $k = 0$. The results of this spin-splitting is schematically depicted in Fig. B.1.

The electron velocity operator is easily calculated using the relation $\mathbf{v} = \boldsymbol{\nabla}_{\mathbf{p}} H_0$ (Eq. (2.14)),

$$v_x = \frac{p_x}{m^*} - \alpha_R \sigma_y, \tag{B.6}$$

$$v_y = \frac{p_y}{m^*} + \alpha_R \sigma_x. \tag{B.7}$$

With the above expressions, the transition matrix elements between the $\phi_{\pm\mathbf{k}}(\mathbf{r})$ states (Eq. (2.17)),

$$C_{-+}^{(\alpha)}(\mathbf{k}) = -\frac{1}{c}\mathbf{A}_0^{(\alpha)} \cdot \langle \phi_{\mathbf{k},-} | \, \mathbf{v} \, | \phi_{\mathbf{k},+} \rangle \, , \tag{B.8}$$

are readily accessible.

We first note that the spin-diagonal part of the velocity operator (the canonical contribution $\mathbf{p}/m^*$) yields null contribution to $C_{-+}^{(\alpha)}(\mathbf{k})$ since the states $\phi_{\mathbf{k},\pm}(\mathbf{r})$ are orthogonal in spin-basis. With this in mind, we find the following expressions for different light polarizations:

$$C_{-+}^{(x)}(\varphi) = \frac{A_0}{c} \langle \phi_{\mathbf{k},-} | \, \alpha_R \sigma_y \, | \phi_{\mathbf{k},+} \rangle = i \frac{A_0}{c} \alpha_R \sin\varphi, \tag{B.9}$$

$$C_{-+}^{(y)}(\varphi) = -\frac{A_0}{c} \langle \phi_{\mathbf{k},-} | \, \alpha_R \sigma_x \, | \phi_{\mathbf{k},+} \rangle = -i \frac{A_0}{c} \alpha_R \cos\varphi, \tag{B.10}$$

$$C_{-+}^{(R,L)}(\varphi) = \frac{A_0}{\sqrt{2}c} \langle \phi_{\mathbf{k},-} | \, \alpha_R \sigma_y \mp i \alpha_R \sigma_x \, | \phi_{\mathbf{k},+} \rangle = \pm \frac{A_0}{\sqrt{2}c} \alpha_R e^{\mp i\varphi}. \tag{B.11}$$

Therefore, the transition matrix elements only depend on the direction of the momentum φ, but not on the magnitude $|\mathbf{k}|$.

The associated spin-flip transition probabilities, $P_{-+}^{(\alpha)}(\mathbf{k}) \equiv |C_{-+}^{(\alpha)}(\mathbf{k})|^2 / |\mathbf{A}_0^{(\alpha)}|^2$, are straightforwardly obtained from the above expressions,

$$P_{-+}^{(x)}(\varphi) = \frac{\alpha_R^2}{c^2} \sin^2\varphi, \tag{B.12}$$

$$P_{-+}^{(y)}(\varphi) = \frac{\alpha_R^2}{c^2} \cos^2\varphi, \tag{B.13}$$

$$P_{-+}^{(R,L)} = \frac{\alpha_R^2}{2c^2}. \tag{B.14}$$

The last equation shows that the transition probabilities for R and L polarized light are equal and independent of φ, i.e. constant for all momenta.

Finally, we are in position to compute the spin-flip absorption rate (Eq. (2.25)),

$$\begin{aligned} \Lambda^{(\alpha)}(\omega) &= \frac{\omega}{\mathcal{P}} 2\pi \int \frac{\mathrm{d}\mathbf{k}}{(2\pi)^2} (f_{k,-} - f_{k,+}) |C_{-+}^{(\alpha)}(\varphi)|^2 \delta(\epsilon_+(\mathbf{k}) - \epsilon_-(\mathbf{k}) - \omega) \\ &= \frac{1}{2c|A_0|^2\omega} \int_0^{2\pi} \mathrm{d}\varphi |C_{-+}^{(\alpha)}(\varphi)|^2 \int \mathrm{d}k (f_{k,-} - f_{k,+}) k \delta(2\alpha_R k - \omega), \end{aligned} \tag{B.15}$$

where in the last step we have used $\mathcal{P} = |A_0|^2\omega^2/\pi c$ and the fact that the occupation factors only depend on the momentum magnitude, but not on φ.

The integration of the angular part in the above equation yields the same result for all light polarizations, $\int_0^{2\pi} \mathrm{d}\varphi |C_{-+}^{(\alpha)}(\varphi)|^2 = |A_0|^2\pi\alpha_R^2/c^2$. Thus, we finally obtain,

$$\Lambda_{-+}^{(\alpha)}(\omega) = \frac{\pi}{4c}\big(f_{\omega,-} - f_{\omega,+}\big), \tag{B.16}$$

with $f_{\omega,\pm} = \left(\exp\left(\dfrac{\omega^2/2 \pm \alpha_R\omega - E_F}{k_B T}\right) + 1\right)^{-1}$ and E_F the Fermi level.

The spin-flip absorption rate in the Rashba model turns out to be independent of the external field polarization. Furthermore, it is almost independent of the Rashba parameter α_R, which enters only through the occupation factors. Indeed, for $T \to 0$ we have

$$\lim_{T\to 0} \Lambda_{-+}^{(\alpha)}(\omega) = \begin{cases} \dfrac{\pi}{4c} \sim 0.57\% & \text{if } \frac{\omega^2}{2} + \alpha_R\omega - E_F > 0 \\ & \text{and } \frac{\omega^2}{2} - \alpha_R\omega - E_F < 0, \\ 0 & \text{otherwise.} \end{cases} \tag{B.17}$$

Therefore, α_R does not affect the amount of light absorbed at a given frequency, but only the range of frequencies in which light is absorbed.

Appendix C

Gauge transformation

In this Appendix we briefly review the formalism introduced by Wang and co-workers [54] to express the matrix elements involving **k**-space derivatives of the Bloch functions in terms of matrix elements involving MLWFs.

We assume that we have M MLWFs per unit cell, denoted as $|\mathbf{R}n\rangle$. Then, we recast the expression of the periodic part of a Bloch-like function in terms of the MLWFs ,

$$|u_{n\mathbf{k}}^{(W)}\rangle = \sum_{\mathbf{R}} e^{-i\mathbf{k}\cdot(\mathbf{r}-\mathbf{R})}\,|\mathbf{R}n\rangle\,. \tag{C.1}$$

The above states are not in general eigenstates of the Hamiltonian, and we will refer to them as belonging to the Wannier gauge (W). The usual Bloch states that are eigenstates of the Hamiltonian are obtained by a unitary rotation,

$$|u_{n\mathbf{k}}^{(H)}\rangle = \sum_{m} |u_{m\mathbf{k}}^{(W)}\rangle\, U_{mn}(\mathbf{k}). \tag{C.2}$$

We refer to the above as the Hamiltonian gauge (H).

The connection between the two gauges is given by the rotation matrix $U(\mathbf{k})$, which is therefore referred as a gauge transformation. Let us analyze the properties of this matrix by considering the reduced Hamiltonian,

$$H^{(H)}(\mathbf{k}) = e^{-i\mathbf{k}\cdot\mathbf{r}}H(\mathbf{k})e^{i\mathbf{k}\cdot\mathbf{r}}, \tag{C.3}$$

where $H(\mathbf{k})$ is the full single particle Hamiltonian of the system. The above reduced Hamiltonian $H^{(H)}(\mathbf{k})$ is a $M \times M$ matrix in band indexes fulfilling

$$\langle u_{n\mathbf{k}}^{(H)}|H^{(H)}(\mathbf{k})|u_{n\mathbf{k}}^{(H)}\rangle = \delta_{nm}\epsilon_n(\mathbf{k}). \tag{C.4}$$

This is why we refer to the $|u_{n\mathbf{k}}^{(H)}\rangle$ as belonging to the Hamiltonian gauge (H), because precisely in this gauge the Hamiltonian is diagonal. Then, we can construct the following reduced $M \times M$ Hamiltonian matrix in the Wannier gauge,

$$H_{nm}^{(W)}(\mathbf{k}) = \left\langle u_{n\mathbf{k}}^{(W)} \,\middle|\, H(\mathbf{k}) \,\middle|\, u_{m\mathbf{k}}^{(W)} \right\rangle. \tag{C.5}$$

The above matrix is not in general diagonal, and one finds the unitary matrix $U(\mathbf{k})$ precisely by diagonalizing $H^{(W)}_{nm}(\mathbf{k})$,

$$H^{(H)}(\mathbf{k}) = U^{\dagger}(\mathbf{k})H^{(W)}(\mathbf{k})U(\mathbf{k}). \tag{C.6}$$

Derivatives in reciprocal space

Next, we analyze how a matrix $A^{(j)}(\mathbf{k})$ with the following elements

$$A^{(j)}_{nm,i}(\mathbf{k}) = \left\langle u^{(j)}_{n\mathbf{k}} \middle| \partial_i \middle| u^{(j)}_{m\mathbf{k}} \right\rangle \tag{C.7}$$

transforms between the $j = H$ and $j = W$ gauges, with $\partial_i \equiv \partial/\partial k_i$ a $\mathbf{k}$-space derivative along the direction i. Note that this object is precisely the Berry connection entering the transition matrix element of Eq. (2.18). This quantity is ill-defined in the Hamiltonian gauge due to the inherent phase indeterminacy of the Bloch states, whereas in the Wannier gauge it is well defined as the phase is fixed via the MLWFs.

In the case of an 'ordinary' operator, such as the Hamiltonian, one can transform between the Wannier and Hamiltonian gauges just by operating on the left and right by the rotation matrix (see Eq. (C.6)). However, quantities such as $A^{(j)}_{nm,i}(\mathbf{k})$ in Eq. (C.7) introduce an extra term in the transformation as a consequence of the explicit $\mathbf{k}$-space derivative:

$$A^{(H)}_i = U^{\dagger}A^{(W)}_i U + U^{\dagger}\partial_i U, \tag{C.8}$$

where we have omitted the $\mathbf{k}$-dependence for the sake of simplicity. Thus, the extra term $U^{\dagger}\partial_i U$ takes into account the $\mathbf{k}$-space variation of the rotation matrix. This term may be obtained from perturbation theory for variations in $\mathbf{k}$-space (so-called $\mathbf{k}{\cdot}\mathbf{p}$ method [22]),

$$(U^{\dagger}\partial_i U)_{nm} = \begin{cases} \dfrac{(U^{\dagger}H^{(W)}_i U)_{nm}}{\epsilon_m - \epsilon_n} & \text{if } n \neq m \\ 0 & \text{if } n = m, \end{cases} \tag{C.9}$$

with $H^{(W)}_i \equiv \partial_i H^{(W)}$ the $\mathbf{k}$-space derivative of the reduced Hamiltonian in the Wannier gauge. Since $H^{(W)}$ is smooth in reciprocal space, its $\mathbf{k}$-space derivative is well defined. We notice that the gauge choice implicit in Eq. (C.9) is $(U^{\dagger}H^{W}_i U)_{nn} = 0$, the so-called parallel transport gauge.

The final step is to express $A^{(H)}_{nm,i}$ in terms of MLWFs matrix elements. The needed quantities are

$$H^{(W)}_{nm}(\mathbf{k}) = \sum_{\mathbf{R}} e^{i\mathbf{k}\mathbf{r}} \left\langle \mathbf{0}n \,|\, H \,|\, \mathbf{R}m \right\rangle, \tag{C.10}$$

$$H^{(W)}_{nm,i}(\mathbf{k}) = \sum_{\mathbf{R}} i\mathbf{k}e^{i\mathbf{k}\mathbf{r}} \left\langle \mathbf{0}n \,|\, H \,|\, \mathbf{R}m \right\rangle, \tag{C.11}$$

$$A^{(W)}_{nm,i}(\mathbf{k}) = \sum_{\mathbf{R}} e^{i\mathbf{k}\mathbf{r}} \left\langle \mathbf{0}n \,|\, r_i \,|\, \mathbf{R}m \right\rangle. \tag{C.12}$$

which follow from combining Eqs. (C.1), (C.6) and (C.7).

Appendix D

Effect of a time-dependent EMF in surfaces with strong SOI

We consider the effect of an external time-dependent EMF with frequency ω and wavevector $\mathbf{q} = q\hat{\mathbf{e}}_z$ propagating along the surface-perpendicular direction z. It is always possible to find a gauge where the scalar potential associated to the EMF is null, i.e. $\Phi_{\text{ext}}(\mathbf{r}, t) = 0$; this corresponds to the so-called temporal or Weyl gauge [144]. Within this gauge, the external EMF is fully described by the vector potential [145]

$$\mathbf{A}^{(\alpha)}_{\text{ext}}(\mathbf{r}, t) = \mathbf{A}^{(\alpha)}_0 e^{i\mathbf{q}\cdot\mathbf{r}} e^{-i\omega t} + \mathbf{A}^{(\alpha)*}_0 e^{-i\mathbf{q}\cdot\mathbf{r}} e^{i\omega t}. \tag{D.1}$$

Above, α stands for the polarization of the external field, and $\mathbf{A}^{(\alpha)}_0$ is a vector constrained to the (x, y) plane.

The expression for the electric field associated to the EMF through Maxwell's equations is

$$\begin{aligned} \mathbf{E}^{(\alpha)}_{\text{ext}}(\mathbf{r}, t) &= -\frac{1}{c}\frac{\partial \mathbf{A}^{(\alpha)}_{\text{ext}}(\mathbf{r}, t)}{\partial t} \\ &= i\frac{\omega}{c}\mathbf{A}^{(\alpha)}_0 e^{i\mathbf{q}\cdot\mathbf{r}} e^{-i\omega t} - i\frac{\omega}{c}\mathbf{A}^{(\alpha)*}_0 e^{-i\mathbf{q}\cdot\mathbf{r}} e^{i\omega t}. \end{aligned} \tag{D.2}$$

In this gauge the electric field is parallel to the vector potential, in contrast to the magnetic field, $\mathbf{B}^{(\alpha)}_{\text{ext}}(\mathbf{r}, t) = \boldsymbol{\nabla} \times \mathbf{A}^{(\alpha)}_{\text{ext}}(\mathbf{r}, t)$, which is perpendicular.

The full Hamiltonian containing the interaction with the EMF is described up to order $(v/c)^2$ by [57]

$$\begin{aligned} H = & \frac{\left(\mathbf{p} - \frac{1}{c}\mathbf{A}^{(\alpha)}_{\text{ext}}(\mathbf{r}, t)\right)^2}{2} + V(\mathbf{r}) + V_{\text{sc}}(\mathbf{r}) - \frac{1}{2c}\boldsymbol{\sigma} \cdot \left(\boldsymbol{\nabla} \times \mathbf{A}^{(\alpha)}_{\text{ext}}(\mathbf{r}, t)\right) \\ & - \frac{1}{4c^2}\boldsymbol{\sigma} \cdot \left(\boldsymbol{\nabla} V(\mathbf{r}) \times \left(\mathbf{p} - \frac{1}{c}\mathbf{A}^{(\alpha)}_{\text{ext}}(\mathbf{r}, t)\right)\right), \end{aligned} \tag{D.3}$$

Above, it is assumed that the potential $V_{\mathrm{sc}}(\mathbf{r})$ contains the scalar relativistic mass-velocity and Darwin contributions, which are unimportant for our purposes here. Safely omitting the term quadratic in $\mathbf{A}^{(\alpha)}_{\mathrm{ext}}(\mathbf{r},t)$ too, the general Hamiltonian of Eq. (D.3) can be decomposed into smaller pieces of different orders of magnitude,

$$H_0 = \frac{\mathbf{p}^2}{2} + V(\mathbf{r}) - \frac{1}{4c^2}\boldsymbol{\sigma}\cdot(\boldsymbol{\nabla}V(\mathbf{r})\times\mathbf{p}) \tag{D.4}$$

$$H_1(t) = -\frac{1}{c}\left(\mathbf{p}\cdot\mathbf{A}^{(\alpha)}_{\mathrm{ext}}(\mathbf{r},t) - \frac{1}{4c^2}\boldsymbol{\sigma}\cdot\left(\boldsymbol{\nabla}V(\mathbf{r})\times\mathbf{A}^{(\alpha)}_{\mathrm{ext}}(\mathbf{r},t)\right)\right) \tag{D.5}$$

$$H_2(t) = -\frac{1}{2c}\boldsymbol{\sigma}\cdot\left(\boldsymbol{\nabla}\times\mathbf{A}^{(\alpha)}_{\mathrm{ext}}(\mathbf{r},t)\right) \tag{D.6}$$

The dominant term, H_0, is the ground-state Hamiltonian containing, among other contributions, the relativistic SOI. $H_1(t)$ includes the coupling of the external vector potential to the momentum as well as to $\boldsymbol{\sigma}\times\boldsymbol{\nabla}V(\mathbf{r})$. Finally, $H_2(t)$ is the Zeeman term, coupling the spin to the external magnetic field.

Simple analysis of the order of magnitude of $H_1(t)$ and $H_2(t)$ perturbation terms

Usually, the first order relativistic Zeeman term dominates over the $H_1(t)$ term, which includes a first order and a third order relativistic correction. In surfaces with strong relativistic effects, however, the magnitude of $\boldsymbol{\nabla}V(\mathbf{r})$ can be so large that the $H_1(t)$ term can dominate over the $H_2(t)$ term. Considering only the spin-dependent part of $H_1(t)$, we compare the magnitude of the two terms,

$$\left|\frac{H_1(t)}{H_2(t)}\right| \sim \left|\frac{\boldsymbol{\nabla}V(\mathbf{r})}{2c^2\mathbf{q}}\right|, \tag{D.7}$$

where we have used $\boldsymbol{\nabla}\times\mathbf{A}^{(\alpha)}_{\mathrm{ext}}(\mathbf{r},t)\sim\mathbf{q}\cdot\mathbf{A}^{(\alpha)}_{\mathrm{ext}}(\mathbf{r},t)$ (see Eq. (D.1)). Next, we estimate the magnitude of potential gradient considering the spin-splitting ΔE induced by the SOC,

$$\left|\frac{1}{4c^2}\boldsymbol{\sigma}\cdot(\boldsymbol{\nabla}V(\mathbf{r})\times\mathbf{p})\right| = \Delta E. \tag{D.8}$$

Solving the above equation for $\boldsymbol{\nabla}V(\mathbf{r})$ and inserting it in Eq. (D.7), we obtain that

$$\left|\frac{H_1(t)}{H_2(t)}\right| \sim 2\left|\frac{\Delta E}{\mathbf{p}\cdot\mathbf{q}}\right|. \tag{D.9}$$

In surfaces analyzed in this work, ΔE is of the order of 0.1 eV$\sim 10^{-3}$ a.u., and $|\mathbf{p}|\sim 1-10^{-1}$ a.u.. Finally, considering the typical magnitude of the wave vector of an external optical field, $|\mathbf{q}|\sim 10^{-3}-10^{-4}$ a.u., we obtain the following comparative order of magnitude,

$$\left|\frac{H_1(t)}{H_2(t)}\right| \sim 10^0 - 10^2. \tag{D.10}$$

This is the reason why throughout the text we have assumed that $H_1(t)$ is the main perturbation term and have omitted the $H_2(t)$ term from our considerations.

Velocity operator

The general expression of the velocity operator from the Erhenfest theorem is given by

$$\mathbf{v} = \frac{\partial \mathbf{r}}{\partial t} = -i\left[\mathbf{r}, H_0\right] = \boldsymbol{\nabla}_{\mathbf{p}} H_0. \tag{D.11}$$

Using H_0 as defined in Eq. (D.4), the associated velocity operator is given by

$$\mathbf{v} = \mathbf{p} - \frac{1}{4c^2}\boldsymbol{\sigma} \times \boldsymbol{\nabla} V(\mathbf{r}). \tag{D.12}$$

With the aid of the above equation, the expression for the main perturbation $H_1(t)$ (Eq. (D.5)) can be written as the coupling between the velocity operator and the vector potential of the EMF,

$$H_1(t) = -\frac{1}{c}\mathbf{v} \cdot \mathbf{A}^{(\alpha)}_{\text{ext}}(\mathbf{r}, t). \tag{D.13}$$

In our approach, this is the main interaction Hamiltonian appearing in Eq. (2.13) with $H_1(t) \equiv H_{\text{int}}(t)$. As the vector potential is parallel to the electric field (Eq. (D.2)), the above term is sometimes identified as the electric coupling, to distinguish from the more common magnetic Zeeman coupling $H_2(t)$.

Appendix E

2D optical lattices using plane waves

The QUANTUM-ESPRESSO package [23] used throughout the work is a code for electronic-structure calculations that implements the DFT using plane waves as the basis set, as presented in Chapter 1. The central equation solved by the program is the one body KS equation (1.3), which we repeat here,

$$\left(-\frac{1}{2}\nabla^2 + V_{\text{eff}}(\mathbf{r})\right)\phi_{n\mathbf{k}}(\mathbf{r}) = \epsilon_{n\mathbf{k}}\phi_{n\mathbf{k}}(\mathbf{r}), \tag{E.1}$$

the main outcome being the KS eigenfunctions and eigenvalues. As a post-processing step, these quantities play the role of input quantities for the WANNIER90 code [30], which calculates the associated MLWFs. We have taken advantage of the link existing between these two packages in order to calculate the MLWFs corresponding to a 2D optical lattice. For this, we have adapted the QUANTUM-ESPRESSO package in order to include the single particle optical potential into the effective potential $V_{\text{eff}}(\mathbf{r})$. In accordance, the Hartree, the PP and the exchange-correlation contributions have been left out from $V_{\text{eff}}(\mathbf{r})$ (see Eq. (1.4)), as we are only interested in the 2D optical (external) potential.

The QUANTUM-ESPRESSO package is implemented in 3D, whereas the optical lattices are regarded as 2D systems. We overcome this problem by inserting a confining harmonic potential along the direction perpendicular to the 2D plane, which we take as the z axis. The total potential inserted in 3D is therefore

$$V_{\text{eff}}(\mathbf{r}) = V_{\text{opt}}(x, y) + \frac{1}{2}\omega^2 z^2, \tag{E.2}$$

with $V(z) = \omega^2 z^2/2$ the harmonic oscillator and $V_{\text{opt}}(x, y)$ the actual 2D optical potential (see Eqs. (4.7) and (4.18) for the two specific examples analyzed in the work). The eigenfunctions $\Psi_{nm\mathbf{k}}(\mathbf{r})$ of the Schrödinger equation associated to the potential of Eq. E.2 are of the separable form

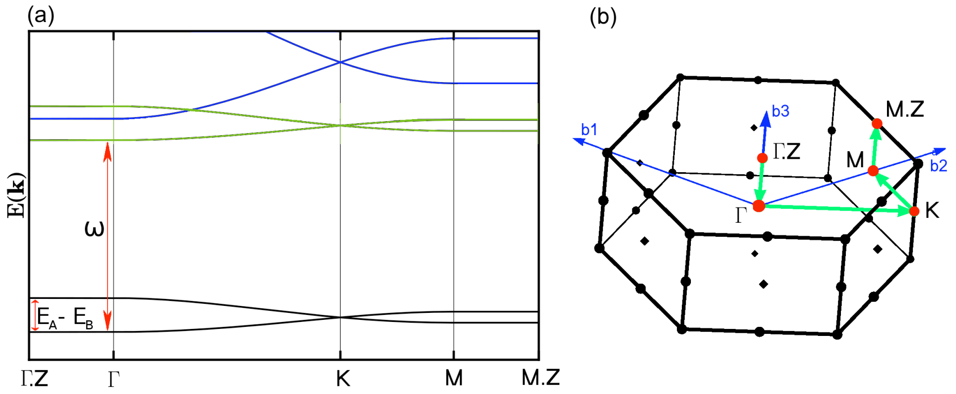

Figure E.1: (a) Band structure corresponding to the ideal honeycomb potential (analyzed in Sec. 4.2) along a 3D path. The black and green lines show the energy dispersion of the two lowest states of the 2D potential with harmonic quantum number $m = 0$ and $m = 1$, respectively. The blue lines denote the first excited state of the 2D potential with $m = 0$. (b) BZ associated to the 3D unit cell, with $\mathbf{b}_3$ the reciprocal lattice vector perpendicular to the 2D plane in which $\mathbf{b}_1$ and $\mathbf{b}_2$ are defined (Eq. (4.8)).

$\Psi_{nm\mathbf{k}}(\mathbf{r}) = \phi_{n\mathbf{k}}(x,y)\varphi_m(z)$, with $\varphi_m(z)$ the eigenfunctions of the 1D harmonic potential, $V(z)$, whose spectrum is

$$\varepsilon_m = (\frac{1}{2} + m)\omega, \quad m \in \mathbb{N}. \tag{E.3}$$

In practice, the value of the frequency ω is chosen so that the energy difference between the two lowest harmonic levels, $\varepsilon_1 - \varepsilon_0 = \omega$, is much bigger than the maximum energy separation between the two lowest Bloch bands, $E_A(\mathbf{k}) - E_B(\mathbf{k})$, associated to the eigenstates $\phi_{A\mathbf{k}}(x,y)$ and $\phi_{B\mathbf{k}}(x,y)$ of the 2D potential.

A helpful illustration is included in Fig. E.1, where we show the dispersion of the bands corresponding to the ideal honeycomb potential analyzed in Sec. 4.2 along a 3D path in reciprocal space. The black lines denote the two lowest Bloch bands of the honeycomb potential with the harmonic quantum number $m = 0$, whereas the green lines also correspond to the two lowest Bloch bands but with harmonic quantum number $m = 1$. This is why the dispersion of the black and green lines is identical, the only difference being an overall energy shift. The value of this energy shift is precisely ω, which has been chosen much bigger than the maximum energy separation of the two lowest bands, $E_A(\mathbf{k}) - E_B(\mathbf{k})$ (see the figure). With this procedure, it is possible to isolate the two bands of interest (the blcak ones) from the rest, reproducing the energy dispersion of the 2D lattice. We also notice the null dispersion along the z direction (see band structure along Γ.Z-Γ and M-M.Z), meaning that the Bloch states do not overlap along this direction.

Finally, we mention that the blue lines of the band structure correspond to the first excited states of the 2D honeycomb potential, which lie much above than the lowest two.

Appendix F

Tight binding spectrum

In this Appendix we derive the general tight binding spectrum valid for any configuration with two minima per unit cell following [133] (the minima are not necessarily assumed to be degenerate). We employ the notation used in Sec. 4.3 for the tunneling coefficients, since it is more general than the one used in Sec. 4.2, which in fact is a particular case of the previous.

We begin by defining the operator

$$b_{n\mathbf{k}} = \frac{\sqrt{V}}{2\pi} \sum_{\mathbf{R}} e^{-i\mathbf{k}\cdot\mathbf{R}} a_{n\mathbf{R}}. \tag{F.1}$$

Then, the tight binding Hamiltonian $\mathcal{H}_0^{tb}$ (Eq. (4.4)) can be written as

$$\mathcal{H}_0^{tb} = \sum_{nn'=A,B} \sum_{\mathbf{k}} h_{nn'}(\mathbf{k}) b^{\dagger}_{n\mathbf{k}} b_{n'\mathbf{k}} \tag{F.2}$$

with

$$h_{nn'}(\mathbf{k}) = \sum_{\mathbf{R}} e^{i\mathbf{k}\cdot\mathbf{R}} T^{\mathbf{R}}_{nn'}. \tag{F.3}$$

The above equation can be expressed in a matrix form separating the diagonal and off-diagonal terms in the band index,

$$h_{nn'}(\mathbf{k}) = \begin{pmatrix} \epsilon_A(\mathbf{k}) & z(\mathbf{k}) \\ z^*(\mathbf{k}) & \epsilon_B(\mathbf{k}) \end{pmatrix}. \tag{F.4}$$

The two lowest energy bands are then given by the eigenvalues of (F.4),

$$\varepsilon_{\pm}(\boldsymbol{k}) = \epsilon_+(\mathbf{k}) \pm \sqrt{\epsilon_-^2(\mathbf{k}) + |z(\mathbf{k})|^2}, \tag{F.5}$$

with

$$\epsilon_{\pm}(\mathbf{k}) = \frac{\epsilon_A(\mathbf{k}) \pm \epsilon_B(\mathbf{k})}{2}. \tag{F.6}$$

Let us start by considering the diagonal terms. By fixing an arbitrary energy offset, we can write

$$\begin{aligned} \epsilon_A(\mathbf{k}) &= \epsilon + F^A(\mathbf{k}) \qquad (F.7) \\ \epsilon_B(\mathbf{k}) &= -\epsilon + F^B(\mathbf{k}) \qquad (F.8) \end{aligned}$$

with

$$\epsilon = \frac{E_A - E_B}{2} \qquad (F.9)$$

and

$$\begin{aligned} F^n(\mathbf{k}) &= 2j_1^n \cos\left(\mathbf{k}\cdot(\mathbf{a}_2 - \mathbf{a}_1)\right) \\ &\quad +4j_2^n \cos\left(\mathbf{k}\cdot\frac{(\mathbf{a}_2 - \mathbf{a}_1)}{2}\right)\cos\left(\mathbf{k}\cdot\frac{(\mathbf{a}_1 + \mathbf{a}_2)}{2}\right) \\ &\quad +2j_3^n \cos\left(\mathbf{k}\cdot(\mathbf{a}_1 + \mathbf{a}_2)\right). \qquad (F.10) \end{aligned}$$

This expression is valid for a generic structure with two potential minima per unit cell. When the two minima are degenerate, as it is the case of the examples analyzed in Sec. 4.2 and in Sec. 4.3 when $\theta = \pi$, we have that

$$F^A(\mathbf{k}) = F^B(\mathbf{k}) \equiv F(\mathbf{k}), \qquad (F.11)$$

and the eigenvalues in Eq. (F.5) take the following simple form

$$\varepsilon_\pm(\mathbf{k}) = F(\mathbf{k}) \pm |z(\mathbf{k})|. \qquad (F.12)$$

We focus now on the off-diagonal matrix element $z(\mathbf{k})$. Its analytical form is given by

$$\begin{aligned} z(\mathbf{k}) \equiv &-\Big[t_0 + t_1(e^{-i\mathbf{k}\cdot\mathbf{a}_1} + e^{-i\mathbf{k}\cdot\mathbf{a}_2}) \\ &+t_2 e^{-i\mathbf{k}\cdot(\mathbf{a}_1+\mathbf{a}_2)} + 2t_3\cos(\mathbf{k}\cdot(\mathbf{a}_2 - \mathbf{a}_1)\Big]. \qquad (F.13) \end{aligned}$$

The above is valid both for degenerate and non-degenerate cases since the definition of the off-diagonal terms is not affected by parity breaking.

Ideal honeycomb lattice

The particular (more symmetric) case of the ideal honeycomb lattice considered in Sec. 4.2 with only the closest nearest neighbors would be recovered with the following substitutions,

$$t_0 = t_1 \to t_0,\ j_1 = j_2 \to t_1,\ t_2 = t_3 \to t_2,\ j_3 = 0. \qquad (F.14)$$

Then, the expression for the diagonal term simplifies to

$$F(\mathbf{k}) = 2t_1\left[\cos\left(\mathbf{k}\cdot(\mathbf{a}_1 - \mathbf{a}_2)\right) + \sum_{i=1,2}\cos\left(\mathbf{k}\cdot\mathbf{a}_i\right)\right]. \qquad (F.15)$$

Similarly, the off-diagonal term takes the following form,

$$z(\mathbf{k}) = t_0 Z_0(\mathbf{k}) + t_2 Z_2(\mathbf{k}), \tag{F.16}$$

with

$$\begin{aligned} Z_0(\mathbf{k}) &= 1 + e^{-i\mathbf{k}\cdot\mathbf{a}_1} + e^{-i\mathbf{k}\cdot\mathbf{a}_2}, \\ Z_2(\mathbf{k}) &= e^{-i\mathbf{k}\cdot(\mathbf{a}_1+\mathbf{a}_2)} + e^{-i\mathbf{k}\cdot(\mathbf{a}_1-\mathbf{a}_2)} + e^{-i\mathbf{k}\cdot(\mathbf{a}_2-\mathbf{a}_1)}. \end{aligned} \tag{F.17}$$

Finally, the expression for the spectrum takes the following compact form

$$\bar{\varepsilon}_{\pm}(\mathbf{k}) = t_1 F(\mathbf{k}) \pm |t_0 Z_0(\mathbf{k}) + t_2 Z_2(\mathbf{k})| + 3t_1, \tag{F.18}$$

where the last term has been added in order to make the energy vanishing at the Dirac points.

It is worth mentioning that the parameter values of $t_0 + t_2$ and t_1 can be extracted from a fit of the Bloch spectrum at $\mathbf{k} = \mathbf{0}$ by using the expression of Eq. (F.18). In fact, we obtain that

$$t_0 + t_2 = \frac{\bar{\varepsilon}_+(\mathbf{0}) - \bar{\varepsilon}_-(\mathbf{0})}{6}, \tag{F.19}$$

$$t_1 = \frac{\bar{\varepsilon}_+(\mathbf{0}) + \bar{\varepsilon}_-(\mathbf{0})}{18}. \tag{F.20}$$

Also, since t_2 is negligible in comparison to t_0 (see Fig. 4.4), Eq. (F.19) can be used as an accurate estimate of t_0. Notably, these estimates coincide with the calculated tunneling coefficients, representing an independent check for the approach in terms of the MLWFs.

Bibliography

[1] G. H. Wannier, Phys. Rev. **52**, 191 (1937).

[2] N. Marzari and D. Vanderbilt, Phys. Rev. B **56**, 12847 (1997).

[3] R. D. King-Smith and D. Vanderbilt, Phys. Rev. B **47**, 1651 (1993).

[4] D. Vanderbilt and R. D. King-Smith, Phys. Rev. B **48**, 4442 (1993).

[5] R. Resta, Rev. Mod. Phys. **66**, 899 (1994).

[6] T. Thonhauser, D. Ceresoli, D. Vanderbilt, and R. Resta, Phys. Rev. Lett. **95**, 137205 (2005).

[7] D. Xiao, J. Shi, and Q. Niu, Phys. Rev. Lett. **95**, 137204 (2005).

[8] D. Ceresoli, T. Thonhauser, D. Vanderbilt, and R. Resta, Phys. Rev. B **74**, 024408 (2006).

[9] J. Shi, G. Vignale, D. Xiao, and Q. Niu, Phys. Rev. Lett. **99**, 197202 (2007).

[10] I. Souza and D. Vanderbilt, Phys. Rev. B **77**, 054438 (2008).

[11] F. Giustino, M. L. Cohen, and S. G. Louie, Phys. Rev. B **76**, 165108 (2007).

[12] A. Eiguren and C. Ambrosch-Draxl, Phys. Rev. B **78**, 045124 (2008).

[13] M. Calandra, G. Profeta, and F. Mauri, Phys. Rev. B **82**, 165111 (2010).

[14] P. L. Silvestrelli, Phys. Rev. B **59**, 9703 (1999).

[15] L. Bernasconi and P. Madden, Journal of Molecular Structure **544**, 49 (2001), ISSN 0166-1280.

[16] A. Lazicki, A. F. Goncharov, V. V. Struzhkin, R. E. Cohen, Z. Liu, E. Gregoryanz, C. Guillaume, H. Mao, and R. J. Hemley, Proceedings of the National Academy of Sciences **106**, 6525 (2009).

[17] N. W. Ashcroft and N. D. Mermin, *Solid State Physics* (Thomson Learning Inc., 1976).

[18] P. Hohenberg and W. Kohn, Phys. Rev. **136**, B864 (1964).

[19] C. Bowen, G. Sugiyama, and B. J. Alder, Phys. Rev. B **50**, 14838 (1994).

[20] J. P. Perdew, K. Burke, and M. Ernzerhof, Phys. Rev. Lett. **77**, 3865 (1996).

[21] D. M. Ceperley and B. J. Alder, Phys. Rev. Lett. **45**, 566 (1980).

[22] R. M. Martin, *Electronic structure: basic theory and practical methods* (Cambridge University Press, 2004).

[23] P. Giannozzi et al., Journal of Physics: Condensed Matter **21**, 395502 (2009).

[24] E. Anderson, Z. Bai, C. Bischof, S. Blackford, J. Demmel, J. Dongarra, J. Du Croz, A. Greenbaum, S. Hammarling, A. McKenney, et al., *LAPACK Users' Guide* (Society for Industrial and Applied Mathematics, Philadelphia, PA, 1999), 3rd ed., ISBN 0-89871-447-8 (paperback).

[25] D. R. Hamann, M. Schlüter, and C. Chiang, Phys. Rev. Lett. **43**, 1494 (1979).

[26] L. Kleinman and D. M. Bylander, Phys. Rev. Lett. **48**, 1425 (1982).

[27] D. Vanderbilt, Phys. Rev. B **41**, 7892 (1990).

[28] I. Souza, N. Marzari, and D. Vanderbilt, Phys. Rev. B **65**, 035109 (2001).

[29] E. I. Blount, Solid State Physics **13**, 305 (1962).

[30] A. Mostofi, J. Yates, Y. Lee, I. Souza, D. Vanderbilt, and I. Marzari, Comput. Phys. Commun. **178**, 685 (2008).

[31] G. Panati and A. Pisante, ArXiv e-prints (2011), `1112.6197`.

[32] A. A. Soluyanov and D. Vanderbilt, Phys. Rev. B **83**, 235401 (2011).

[33] X. Wang, D. Vanderbilt, J. R. Yates, and I. Souza, Phys. Rev. B **76**, 195109 (2007).

[34] Y.-S. Lee, M. B. Nardelli, and N. Marzari, Phys. Rev. Lett. **95**, 076804 (2005).

[35] M. Shelley, N. Poilvert, A. A. Mostofi, and N. Marzari, Computer Physics Communications **182**, 2174 (2011), ISSN 0010-4655.

[36] N. Marzari, A. A. Mostofi, J. R. Yates, I. Souza, and D. Vanderbilt, Rev. Mod. Phys. **84**, 1419 (2012).

[37] M. Heide, G. Bihlmayer, P. Mavropoulos, A. Bringer, and S. Blügel, Psi-k Newsletter **78**, 1109 (2006).

[38] J. I. Pascual, G. Bihlmayer, Y. M. Koroteev, H.-P. Rust, G. Ceballos, M. Hansmann, K. Horn, E. V. Chulkov, S. Blügel, P. M. Echenique, et al., Phys. Rev. Lett. **93**, 196802 (2004).

[39] A. Strozecka, A. Eiguren, and J. I. Pascual, Phys. Rev. Lett. **107**, 186805 (2011).

[40] S. LaShell, B. A. McDougall, and E. Jensen, Phys. Rev. Lett. **77**, 3419 (1996).

[41] S. Datta and B. Das, Appl. Phys. Lett. **56** (1990).

[42] P. Tamarat, N. B. Manson, J. P. Harrison, R. L. McMurtrie, A. Nizovtsev, C. Santori, R. G. Beausoleil, P. Neumann, T. Gaebel, F. Jelezko, et al., New Journal of Physics **10**, 045004 (2008).

[43] O. Z. Karimov, G. H. John, R. T. Harley, W. H. Lau, M. E. Flatté, M. Henini, and R. Airey, Phys. Rev. Lett. **91**, 246601 (2003).

[44] J. Nitta, T. Akazaki, H. Takayanagi, and T. Enoki, Phys. Rev. Lett. **78**, 1335 (1997).

[45] S. V. Eremeev, I. A. Nechaev, Y. M. Koroteev, P. M. Echenique, and E. V. Chulkov, Phys. Rev. Lett. **108**, 246802 (2012).

[46] C. R. Ast, J. Henk, A. Ernst, L. Moreschini, M. C. Falub, D. Pacilé, P. Bruno, K. Kern, and M. Grioni, Phys. Rev. Lett. **98**, 186807 (2007).

[47] K. Sakamoto, T. Oda, A. Kimura, K. Miyamoto, M. Tsujikawa, A. Imai, N. Ueno, H. Namatame, M. Taniguchi, P. E. J. Eriksson, et al., Phys. Rev. Lett. **102**, 096805 (2009).

[48] M.-H. Liu and C.-R. Chang, Phys. Rev. B **80**, 241304 (2009).

[49] Y. Ohtsubo, S. Hatta, H. Okuyama, and T. Aruga, Journal of Physics: Condensed Matter **24**, 092001 (2012).

[50] K. Yaji, Y. Ohtsubo, S. Hatta, H. Okuyama, K. Miyamoto, T. Okuda, A. Kimura, H. Namatame, M. Taniguchi, and T. Aruga, Nat. Commun. **1**, 1 (2010).

[51] M. Hochstrasser, J. G. Tobin, E. Rotenberg, and S. D. Kevan, Phys. Rev. Lett. **89**, 216802 (2002).

[52] A. Eiguren and C. Ambrosch-Draxl, New Journal of Physics **11**, 013056 (2009).

[53] E. I. Rashba, Sov. Phys. Solid State **1109** (1960).

[54] X. Wang, J. R. Yates, I. Souza, and D. Vanderbilt, Physical Review B **74**, 195118 (2006).

[55] I. E. Tamm, Z. Phys. **76**, 849 (1932).

[56] W. Shockley, Phys. Rev. **56**, 317 (1939).

[57] A. M. Messiah, *Quantum Mechanics* (Whiley & Sons, North Holland., 1966).

[58] U. von Barth and L. Hedin, Journal of Physics C: Solid State Physics **5**, 1629 (1972).

[59] J. Kubler, K. H. Hock, J. Sticht, and A. R. Williams, Journal of Physics F: Metal Physics **18**, 469 (1988).

[60] P. Kurz, F. Förster, L. Nordström, G. Bihlmayer, and S. Blügel, Phys. Rev. B **69**, 024415 (2004).

[61] J. E. Peralta, G. E. Scuseria, and M. J. Frisch, Phys. Rev. B **75**, 125119 (2007).

[62] L. Kleinman, Phys. Rev. B **21**, 2630 (1980).

[63] G. Theurich and N. A. Hill, Phys. Rev. B **64**, 073106 (2001).

[64] A. D. Corso and A. M. Conte, Phys. Rev. B **71**, 115106 (2005).

[65] T. Noda, S. Mizuno, J. Chung, and H. Tochihara, Japanese Journal of Applied Physics **42**, L319 (2003).

[66] G. Lee, C. G. Hwang, N. D. Kim, J. Chung, J. S. Kim, and S. Lee, Phys. Rev. B **76**, 245409 (2007).

[67] G. Binnig, H. Rohrer, C. Gerber, and E. Weibel, Phys. Rev. Lett. **50**, 120 (1983).

[68] M. Z. Hasan and C. L. Kane, Rev. Mod. Phys. **82**, 3045 (2010).

[69] D. Sanchez-Portal, E. Artacho, and J. M. Soler, Solid State Communications **95**, 685 (1995), ISSN 0038-1098.

[70] O. Gunawan, Y. P. Shkolnikov, K. Vakili, T. Gokmen, E. P. De Poortere, and M. Shayegan, Phys. Rev. Lett. **97**, 186404 (2006).

[71] W. Yao, D. Xiao, and Q. Niu, Phys. Rev. B **77**, 235406 (2008).

[72] E. Sherman, Physical Review B **67**, 161303 (2003).

[73] E. I. Rashba, Phys. Rev. B **68**, 241315 (2003).

[74] Z. Fang, N. Nagaosa, K. S. Takahashi, A. Asamitsu, R. Mathieu, T. Ogasawara, H. Yamada, M. Kawasaki, Y. Tokura, and K. Terakura, Science **302**, 92 (2003).

[75] Y. Yao, L. Kleinman, A. H. MacDonald, J. Sinova, T. Jungwirth, D.-s. Wang, E. Wang, and Q. Niu, Phys. Rev. Lett. **92**, 037204 (2004).

[76] M. G. Lopez, D. Vanderbilt, T. Thonhauser, and I. Souza, Phys. Rev. B **85**, 014435 (2012).

[77] M. V. Berry, Proceedings of the Royal Society of London. A. Mathematical and Physical Sciences **392**, 45 (1984).

[78] J. Henk, M. Hoesch, J. Osterwalder, A. Ernst, and P. Bruno, Journal of Physics: Condensed Matter **16**, 7581 (2004).

[79] M.-H. Liu, S.-H. Chen, and C.-R. Chang, Phys. Rev. B **78**, 195413 (2008).

[80] Anton and Kokalj, Computational Materials Science **28**, 155 (2003).

[81] J. Henk, A. Ernst, and P. Bruno, Phys. Rev. B **68**, 165416 (2003), URL `http://link.aps.org/doi/10.1103/PhysRevB.68.165416`.

[82] V. P. Gusynin, S. G. Sharapov, and J. P. Carbotte, Phys. Rev. Lett. **96**, 256802 (2006).

[83] A. B. Kuzmenko, E. van Heumen, F. Carbone, and D. van der Marel, Phys. Rev. Lett. **100**, 117401 (2008).

[84] V. V. Struzhkin, M. I. Eremets, W. Gan, H.-k. Mao, and R. J. Hemley, Science **298**, 1213 (2002).

[85] T. Yabuuchi, T. Matsuoka, Y. Nakamoto, and K. Shimizu, Journal of the Physical Society of Japan **75**, 083703 (2006).

[86] H. Olijnyk and W. Holzapfel, Physics Letters A **100**, 191 (1984), ISSN 0375-9601.

[87] H. Fujihisa, Y. Nakamoto, K. Shimizu, T. Yabuuchi, and Y. Gotoh, Phys. Rev. Lett. **101**, 095503 (2008).

[88] Y. Ma, M. Eremets, A. R. Oganov, Y. Xie, I. Trojan, S. Medvedev, A. O. Lyakhov, M. Valle, and V. Prakapenka, Nature **458**, 182 (2009).

[89] T. Matsuoka and K. Shimizu, Nature **458**, 186 (2009).

[90] E. Gregoryanz, O. Degtyareva, M. Somayazulu, R. J. Hemley, and H.-k. Mao, Phys. Rev. Lett. **94**, 185502 (2005).

[91] I. Errea, B. Rousseau, and A. Bergara, Phys. Rev. Lett. **106**, 165501 (2011).

[92] V. M. Silkin, A. Rodriguez-Prieto, A. Bergara, E. V. Chulkov, and P. M. Echenique, Physical Review B **75**, 172102 (2007).

[93] J. B. Neaton and N. W. Ashcroft, Phys. Rev. Lett. **86**, 2830 (2001).

[94] E. Gregoryanz, L. F. Lundegaard, M. I. McMahon, C. Guillaume, R. J. Nelmes, and M. Mezouar, Science **320**, 1054 (2008).

[95] L. F. Lundegaard, E. Gregoryanz, M. I. McMahon, C. Guillaume, I. Loa, and R. J. Nelmes, Phys. Rev. B **79**, 064105 (2009).

[96] M. Hanfland, K. Syassen, L. Loa, N. E. Christensen, and D. L. Novikov, Poster at 2002 High Pressure Gordon Conference (2002).

[97] Rousseau, B., Xie, Y., Ma, Y., and Bergara, A., Eur. Phys. J. B **81**, 1 (2011).

[98] J. B. Neaton and N. W. Ashcroft, Nature **400**, 141 (1999).

[99] I. Errea, B. Rousseau, A. Eiguren, and A. Bergara, Phys. Rev. B **86**, 085106 (2012).

[100] E. Runge and E. K. U. Gross, Phys. Rev. Lett. **52**, 997 (1984).

[101] M. Petersilka, U. J. Gossmann, and E. K. U. Gross, Phys. Rev. Lett. **76**, 1212 (1996).

[102] S. L. Adler, Phys. Rev. **126**, 413 (1962).

[103] D. Pines and P. Nozieres, *The Theory of Quantum Liquids*, vol. vol. 1 (Benjamin, New York, 1966).

[104] K. Sturm, Advances in Physics **31**, 1 (1982).

[105] S. Botti, F. Sottile, N. Vast, V. Olevano, L. Reining, H.-C. Weissker, A. Rubio, G. Onida, R. Del Sole, and R. W. Godby, Phys. Rev. B **69**, 155112 (2004).

[106] J. P. Perdew and A. Zunger, Phys. Rev. B **23**, 5048 (1981).

[107] W. M. Saslow and G. F. Reiter, Phys. Rev. B **7**, 2995 (1973).

[108] H. kwang Mao, C. Kao, and R. J. Hemley, Journal of Physics: Condensed Matter **13**, 7847 (2001).

[109] B. Rousseau, A. Eiguren, and A. Bergara, Phys. Rev. B **85**, 054305 (2012).

[110] I. Errea, A. Rodriguez-Prieto, B. Rousseau, V. M. Silkin, and A. Bergara, Phys. Rev. B **81**, 205105 (2010).

[111] H. J. Monkhorst and J. D. Pack, Phys. Rev. B **13**, 5188 (1976).

[112] *http://opium.sourceforge.net/*.

[113] *http://elk.sourceforge.net/*.

[114] M. Hanfland, I. Loa, and K. Syassen, Physical Review B **65**, 184109 (2002).

[115] A. vom Felde, J. Sprösser-Prou, and J. Fink, Phys. Rev. B **40**, 10181 (1989).

[116] A. vom Felde, J. Sprösser-Prou, and J. Fink, Phys. Rev. B **40**, 10181 (1989).

[117] I. Loa, K. Syassen, G. Monaco, G. Vanko, M. Krisch, and M. Hanfland, Physical Review Letters **107**, 086402 (2011).

[118] Y. Xie, Y. M. Ma, T. Cui, Y. Li, J. Qiu, and G. T. Zou, New Journal of Physics p. 063022 (2008).

[119] H.-K. Mao, Y. Ding, Y. Xiao, P. Chow, J. Shu, S. Lebegue, A. Lazicki, and R. Ahuja, Proceedings of the National Academy of Sciences (2011).

[120] M. H. Anderson, J. R. Ensher, M. R. Matthews, C. E. Wieman, and E. A. Cornell, Science **269**, 198 (1995).

[121] C. C. Bradley, C. A. Sackett, J. J. Tollett, and R. G. Hulet, Phys. Rev. Lett. **75**, 1687 (1995).

[122] K. B. Davis, M. O. Mewes, M. R. Andrews, N. J. van Druten, D. S. Durfee, D. M. Kurn, and W. Ketterle, Phys. Rev. Lett. **75**, 3969 (1995).

[123] I. Bloch, J. B. Dalibard, and W. Zwerger, Rev. Mod. Phys. **80**, 885 (2008).

[124] M. Greiner, O. Mandel, T. Esslinger, and I. Bloch, Nature **415**, 5 (2002).

[125] U. Schneider, L. Hackermüller, S. Will, T. Best, I. Bloch, T. A. Costi, R. W. Helmes, D. Rasch, and A. Rosch, Science **322**, 1520 (2008).

[126] B. Wunsch, F. Guinea, and F. Sols, New Journal of Physics **10**, 103027 (2008).

[127] K. L. Lee, B. Grémaud, R. Han, B.-G. Englert, and C. Miniatura, Phys. Rev. A **80**, 043411 (2009).

[128] P. Soltan-Panahi, J. Struck, P. Hauke, A. Bick, W. Plenkers, G. Meineke, C. Becker, P. Windpassinger, M. Lewenstein, and K. Sengstock, Nature Physics **7**, 434 (2011).

[129] P. Soltan-Panahi, D.-S. Lühmann, J. Struck, P. Windpassinger, and K. Sengstock, Nature Physics **8**, 71 (2011).

[130] R. d. Gail, J. N. Fuchs, M. O. Goerbig, F. Piéchon, and G. Montambaux, Physica B: Physics of Condensed Matter pp. 1–5 (2012).

[131] L. Tarruell, D. Greif, T. Uehlinger, G. Jotzu, and T. Esslinger, Nature **483**, 302 (2012).

[132] L.-K. Lim, J.-N. Fuchs, and G. Montambaux, Phys. Rev. Lett. **108**, 175303 (2012).

[133] M. Modugno and G. Pettini, New J. Phys. **14**, 055004 (2012).

[134] W. Kohn, Phys. Rev. **115**, 809 (1959).

[135] L. He and D. Vanderbilt, Phys. Rev. Lett. **86**, 5341 (2001).

[136] F. Gerbier, A. Widera, S. Fölling, O. Mandel, T. Gericke, and I. Bloch, Phys. Rev. A **72**, 053606 (2005).

[137] J. D. des Cloizeaux, Phys. Rev. **129**, 554 (1963).

[138] J. D. des Cloizeaux, Phys. Rev. **135**, A698 (1964).

[139] J. Ibañez Azpiroz, A. Eiguren, A. Bergara, G. Pettini, and M. Modugno, Phys. Rev. A **87**, 011602 (2013).

[140] J. Jung and A. H. MacDonald, Phys. Rev. B **87**, 195450 (2013).

[141] R. Walters, G. Cotugno, T. H. Johnson, S. R. Clark, and D. Jaksch, Phys. Rev. A **87**, 043613 (2013).

[142] K. L. Lee, *Ultracold fermions in a honeycomb optical lattice* (2010).

[143] G. Montambaux, F. Piéchon, J.-N. Fuchs, and M. O. Goerbig, Phys. Rev. B **80**, 153412 (2009).

[144] H. Weyl, Zeitschrift für Physik **56**, 330 (1929), ISSN 0044-3328.

[145] C. Cohen-Tannoudji, B. Diu, F. Laloe, and B. Dui, *Quantum Mechanics (2 vol. set)* (Wiley-Interscience, 2006), ISBN 0471569526.